A search for intermediate-mass black holes in compact stellar systems through optical emissions from tidal disruption events

by

Richard T. Pomeroy

A thesis submitted in partial fulfilment for the requirements
for the degree of MSc (by Research) in Astrophysics
at the University of Central Lancashire

Jeremiah Horrocks Institute
Supervised by Dr. Mark Norris

Sept 2022

Research Student Declaration

Type of Award   MSc (by Research) Astrophysics

School   School of Natural Sciences

Concurrent registration for two or more academic awards
I declare that while registered as a candidate for the research degree, I have not been a registered candidate or enrolled student for another award of the University or other academic or professional institution.

Material submitted for another award
I declare that no material contained in the thesis has been used in any other submission for an academic award and is solely my own work.

Use of a Proof-reader
No proof-reading service was used in the compilation of this thesis.

Signature of Candidate

Print name: R.T.Pomeroy

Student ID: G20616878

Abstract

In this project, we have taken two separate data sets, and applied them to a search for tidal disruption events (TDEs), to provide evidence for the existence of intermediate-mass black holes (IMBH). The search was performed primarily on the optical archives of the Zwicky Transient facility (ZTF), using light curves and alerts produced by the facility. Follow-up and contextual imaging were also carried out using PanSTARRS and HST archives. The data sets were based on compact stellar system (CSS) positions, covering the mass / radius space from globular clusters through to dwarf elliptical galaxies, with one data set consolidated from literature CSS positions, and the other from notional GC/CSS populations hosted around massive galaxies at distance $2 \leqslant D \leqslant 120$ Mpc.

We discussed the nature of CSS environments, especially considering the low-mass clusters, or ultra-compact dwarf (UCD), end of what is considered a composite population, with the expectation that any TDEs observed in aged cluster populations would involve IMBH and white dwarfs. The larger mass systems, nominally referred to as compact ellipticals (cEs), derived from tidally threshed larger galaxies, are more likely to host IMBH of higher mass, or even super-massive black holes (SMBH), but no strong evidence was found to preclude TDEs also being observed in these systems.

Despite analysis of the archives covering a period of approximately 42 months, no evidence of optical TDE transient signatures was found through either inspection of light curves and transient alerts at known CSS positions, or alerts in the periphery of host galaxies. A statistical analysis was carried out on the second data set, quantifying the sample size and visibility using the globular cluster luminosity function (GCLF). From this result we conclude that the upper limit for the rate of TDEs in CSS is $n_{\mathrm{TDE,Vis}} \lessapprox 10^{-6}\mathrm{yr}^{-1}\mathrm{gal}^{-1}$ which is two orders of magnitude below the theoretical TDE rate involving SMBH interacting with solar mass main sequence stars in the nucleus of massive galaxies.

Contents

Acknowledgements

I would like to acknowledge the support and guidance of my supervisor, Dr. Mark Norris, without whom this work would not have been possible. I thank him for his guidance, patience, perseverance and stimulating discussions throughout the period of this project. His advice and suggestions have at all times been useful and carried me in the right direction. I would also like to thank my second supervisor, Dr. Megan Argo, for her guidance support and advice throughout my project. I would like to thank my viva examiners, Dr. Joanne Pledger and Dr. John Stott, for the time they spend reviewing my thesis, for their thoughtful comments and for the exhilarating discussion we had, which I very much enjoyed.

I would like to thank my wife and family for their unending support throughout the long journey of my research. They have sacrificed so much to allow me to pursue my passion, and I will never be able to thank them enough. Finally, I would like to thank my parents for, so many years ago, nurturing a sense of wonder for the universe and the sky above me - I hope I have made you both proud.

List of Figures

List of Tables

Chapter 1

Introduction

It has been established over that last few decades, that most large galaxies contain super-massive black holes (SMBH) at their centres. The broad characteristics of these galaxies have been found to relate to the mass of their nuclear black holes (M_{BH}) as expressed through a number of 'scaling' relationships. These include bulge velocity dispersion, $M_{\mathrm{BH}} - \sigma_{bulge}$ (Ferrarese & Merritt, 2000), bulge luminosity and mass, $M_{\mathrm{BH}} - L_{bulge}$, $M_{\mathrm{BH}} - M_{bulge}$ (Kormendy & Richstone, 1995) and bulge radial light profile or Sérsic index, $M_{\mathrm{BH}} - n_{bulge}$ (Graham & Driver, 2007). These relationships hint at a fundamental link or feedback mechanism suggesting central black holes play a role in governing the evolution of the galaxy (e.g. Kormendy & Ho, 2013; Ruszkowski et al., 2019) as well as galaxy-wide processes potentially influencing the growth (feeding / merging) of the black hole itself, i.e. co-evolution. As Kormendy & Ho (2013) note, the extent of co-evolution varies in different galaxy types, thus, providing an accurate census of nuclear black holes in different environments and at different mass scales is essential to understanding these relationships in detail and to provide background to galaxy formation hypotheses.

On a more fundamental level, the formation processes of SMBHs are unclear. The naïve assumption that SMBH could grow purely from accretion is confounded by the existence of quasars, i.e. active galactic nuclei (AGN) containing SMBH, at high redshifts. For example, Wang et al. (2021) recently found the most distant quasar discovered to date, estimated at a redshift of $z = 7.642$ or a mere $\sim$670 million years after the big bang, with a mass of 1.6×10^9 M$_\odot$. Several other quasars of high masses, have been found to exist at redshifts $z > 7$, including 8×10^8 M$_\odot$ at $z = 7.54$ (Bañados et al., 2018), 1.5×10^9 M$_\odot$ at $z = 7.515$ (Yang et al., 2020), 2×10^9 M$_\odot$ at $z = 7.085$ (Mortlock et al., 2011). As Wang et al. (2021) points out, continuous accretion at the Eddington limit for 0.65 Gyr would be required for a seed 1000 M$_\odot$ intermediate mass black hole (IMBH - see §1.2) to form a 10^9 M$_\odot$ SMBH. As illustrated in Fig. 1.1, current thinking (e.g. Greene et al., 2020; Mezcua, 2017; Wang et al., 2021) is that the existence of seed IMBH is essential to explain the observed masses of SMBH early in the life of the universe. While there are many candidates, the only IMBHs confirmed so far (of which there have been eight, to March 2022) have been made through the detection of gravitational waves from the merger of two stellar mass (< 100 M$_\odot$) black holes (e.g. Abbott et al., 2020) - see §1.2.

This project aims to add to this area of research by searching for these lower (intermediate) mass black holes which could potentially exist within the low-mass compact stellar systems described below (§1.1). Discovery of candidate nuclear black holes, and correlation with host environment characteristics where they exist would provide evidence to
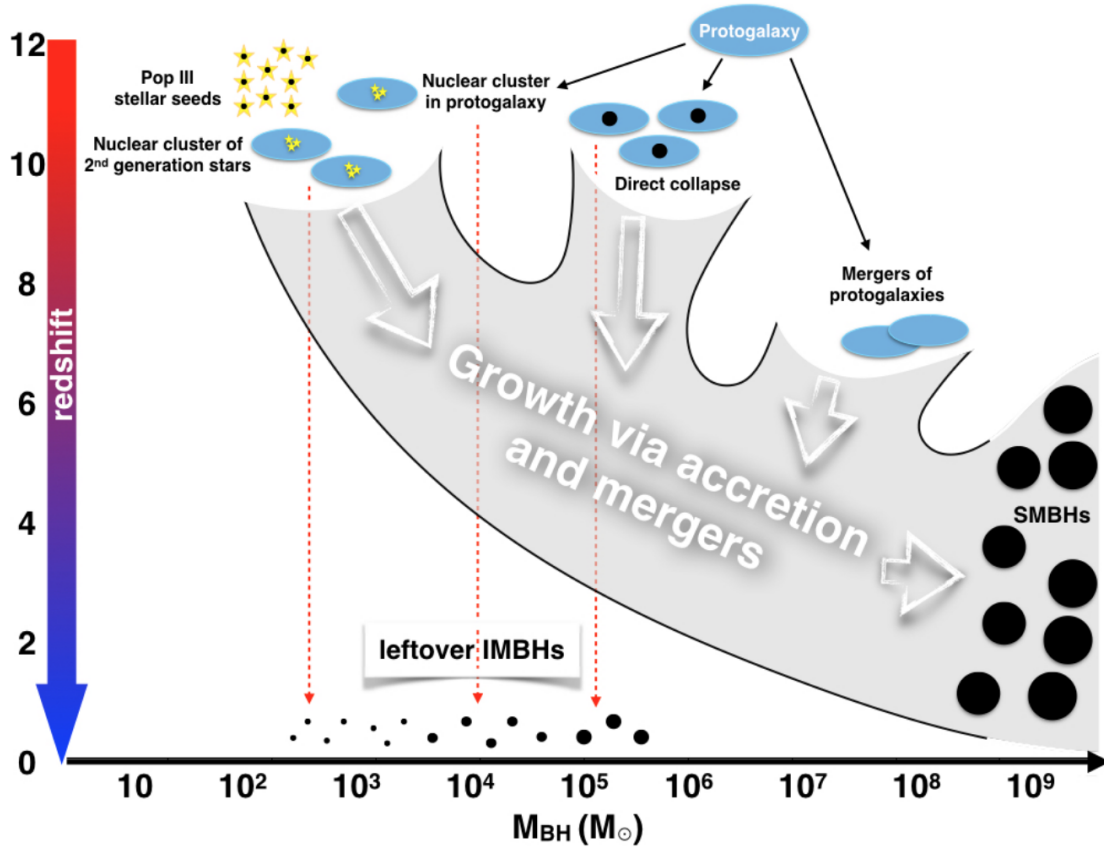
Figure 1.1: SMBH growth model, showing IMBH formation channels as seed black holes through merger and accretion in the early Universe. SMBH are purported to have formed through multiple mergers of IMBHs after host protogalaxies mergers (credit: Mezcua, 2017)

constrain compact stellar system formation processes.

In order to achieve this, analysis was based around searching for the transient signals generated from an event referred to as a Tidal Disruption Event (TDE), where a black hole disrupts a star and radiation is emitted from the accretion disc which forms from matter which remains gravitationally bound to the black hole after the event. With the ever increasing sensitivity of instrumentation, especially when applied through wide-field surveys (e.g. Djorgovski et al., 2013), the opportunity has been afforded to observe lower mass galaxies and thus examine the continuity of black hole / host galaxy scaling relationships through to lower masses. This is significant not only from the depth to which a static sky is now being observed, but also because the speed of processing has allowed multi-epoch observations, initially limited to small areas for targeted projects, but more recently, of the entire sky on a regular basis. Over the last decade, the dynamic nature of astronomical objects has been studied in more detail than ever before - see §2.2 for a summary.

Document Structure

We will initially give some background on Compact Stellar Systems (§1.1) and black holes (§1.2), summarising formation and detection methods for these elusive objects, focusing specifically on intermediate mass black holes (§1.2). After this, details of accretion discs (§1.3) and the specifics of tidal disruption events (§1.4) will be expounded, explaining

further what potential signals could be observed in the data samples outlined in §2.1. As this project is searching for transient signals, the growth of time-domain astronomy, and facility shortlisting and selection is summarised in §2.2, with more detail on the facility selected being described and assessed in §2.3. Details of the analysis carried out and results found are covered in Chapter 3, Chapter 4 and Chapter 5, with this being followed by brief discussion (Chapter 6) and conclusion (Chapter 7) sections.

1.1 Compact Stellar Systems
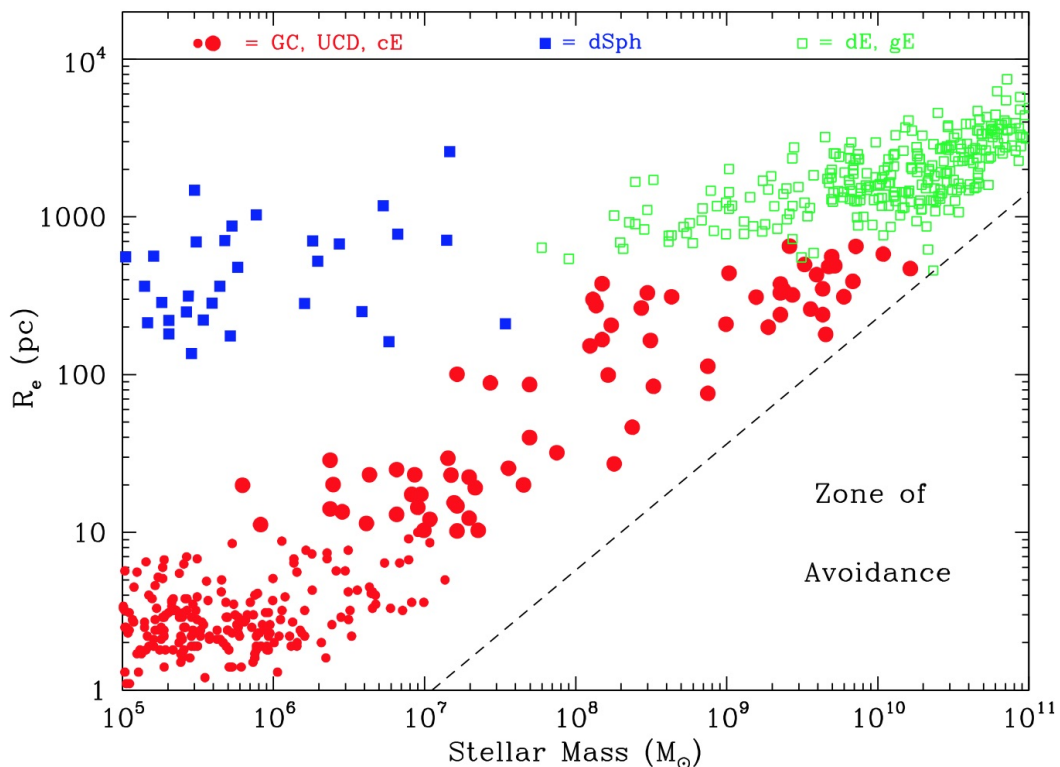
Figure 1.2: Illustration of CSS location in the mass / size parameter space relative to GCs, dwarf spheroidals (dSph), dwarf ellipticals (dE) and classical ellipticals (gE), showing samples from the Archive of Intermediate Mass Stellar Systems (AIMSS) project (Norris et al., 2014) and additional literature data as detailed in Forbes et al. (2014). Large red circles denote UCDs and cEs (> 10pc), with GCs shown with small red circles. The similar mass, but more diffuse and extended dSph are shown by blue squares, and the green squares denote dE and gE. The dashed diagonal line indicates an area of high density in which no objects have currently been found, known as the 'Zone of Avoidance'. (credit: Forbes et al., 2014)

Within this body of work, we consider three types of compact stellar systems (CSS): The well known globular clusters (GCs) which dominate our samples by number, and the related, but more massive ultracompact dwarfs (UCDs) and compact ellipticals (cEs).

Globular Clusters

GCs are dense clusters of stars, which form early in the life of a host galaxy and exist almost exclusively in the halos of these galaxies. Due to their isolated halo locations,

interaction and triggering of star formation is rare or non-existent, and as a result they tend to consist of old, single-stellar populations (i.e. of one age) with little gas or dust for new star forming episodes. All stars in GCs will have similar levels of metallicity, and due to the age and low-mass of the remaining main-sequence stars will be observable as redder objects than systems with multi-age populations. GCs tend to have masses of $\lesssim 10^6$ M$_\odot$ and sizes $R_e \lesssim 10$pc (see Fig. 1.2).

The characteristics of UCDs and CEs place them nominally between GCs and dwarf galaxies in the mass / size parameter space, as illustrated in Fig. 1.2. As noted by Phillipps et al. (2001), in past analysis, many of these objects have been overlooked, being rejected either as background galaxies due to their high surface brightness, or as foreground stars as a result of their compact nature. Initial colour analysis with multi-band photometry, then detailed spectroscopic follow-up on high resolution instrumentation, has been essential to reveal their true nature.

Compact Ellipticals

Compact ellipticals (cEs), especially the local group prototype M32, have been studied extensively since the start of the modern era (e.g. Burbidge et al., 1961; King, 1961; Wirth & Gallagher, 1984; Nieto & Prugniel, 1987; Graham, 2002). Over the last few years, however, the small list of known cEs has been extensively augmented, with discoveries of both isolated and cluster hosted cEs from authors such as Norris et al. (2014), Paudel et al. (2014), Chilingarian & Zolotukhin (2015), Lee & Jang (2016), and Zhang & Bell (2017). Additionally, multiple objects have arisen from survey data analysis, for example in the Virgo cluster (Guérou et al., 2015), the Antila cluster (Smith Castelli et al., 2008) and the Centaurus cluster (Misgeld et al., 2009).

cEs are considered high surface brightness, low-mass elliptical objects which have high stellar density, containing $\sim 10^8 - 10^{10}$ M$_\odot$ (Chilingarian et al., 2009; Norris et al., 2014; Chilingarian & Zolotukhin, 2015) within an effective radius (i.e. half-mass radius) from $100 \lesssim R_e \lesssim 1000$ pc, as shown in Fig. 1.2. Three formation scenarios have been suggested (e.g. Ferré-Mateu et al., 2018) to explain the characteristics of cEs; either an intrinsic growth process (Wirth & Gallagher, 1984; Kormendy et al., 2009), where they would represent the low-mass, low luminosity end of early type galaxies (ETGs); or alternatively, the product of tidal stripping after either a bulged galaxy (Bekki et al., 2001) or a dwarf elliptical galaxy containing a dense core (Faber, 1973) encounters a larger protagonist. In the latter cases, a cE results from the remnant after stripping of the more diffuse outer layers of the progenitor. Following the discovery of cEs both with and without host galaxies, many authors (e.g. Norris et al., 2014; Rey et al., 2020) have argued that both formation processes are viable, with metallicity being a differentiating characteristic. It is expected that knowledge of the mass of a putative black hole would also be a formation differentiator. More recently, Urrutia Zapata et al. (2019) demonstrated that merging star clusters may also account for the existence of cEs.

Ultracompact Dwarfs

First discovered ~ 20 years ago in the Fornax cluster (Hilker et al., 1999; Drinkwater et al., 2000), many more Ultracompact Dwarfs (UCDs) have subsequently been discovered, especially in clusters. For example, in Virgo (Jones et al., 2006), Centaurus (Mieske et al., 2007), Hydra I (Misgeld et al., 2011), Coma (Chiboucas et al., 2011) and Perseus (Penny

et al., 2014). Additionally, UCDs have been found in galaxy groups such as NGC3923 (Norris & Kannappan, 2011) and around isolated galaxies, such as the Sombrero galaxy (M104) (Hau et al., 2009) and NGC4546 (Norris & Kannappan, 2011). UCDs are also high density and high surface brightness, but 'smaller' than cEs with masses between $\sim 10^6 - 10^8$ M$_\odot$ and size between $10 \lesssim R_e \lesssim 100$pc, as in Fig. 1.2. As with cEs, the consensus of current research (e.g. Thomas et al., 2008; Da Rocha et al., 2011; Pfeffer & Baumgardt, 2013; Norris et al., 2015; Pfeffer et al., 2016) suggests multiple formation paths. UCDs could either represent a continuation of the high mass end of globular clusters in a cluster formation scenario, or be the product of tidal stripping after a nucleated dwarf galaxy encounters a larger galaxy, which removes the majority of the dwarf's extended outer structure, but leaves the core relatively intact (Bekki et al., 2001). Most commentators (e.g. Norris et al., 2014; Pfeffer et al., 2016) suggest the UCD population is a composite of the two formation methods, with overlap below a star cluster formation limit of $M_\star \lesssim 7 \times 10^7$ M$_\odot$ (Norris et al., 2014).

1.2 Black Holes

A black hole is a compact object, so massive that the escape velocity from its gravitational field exceeds that of light. Predicted as a consequence of Einstein's (1916) theory of general relativity, a catastrophic gravitational collapse to a singularity, is the ultimate fate of insufficiently supported matter. It was not until the mid-1960's that observations were made of the luminous radio source, 3C 273 (Schmidt, 1963), closely followed by detections of extra-solar X-ray emissions from Cygnus X-1/HDE 226868 (Bowyer et al., 1965). The era of black hole 'observation' was initiated after the former was identified as the first 'quasar' powered by a supermassive black hole and the latter the first stellar-mass black hole.

Black holes come in three main types, classified by range of mass; stellar, intermediate and supermassive.

Stellar mass black holes are the collapsed remnants of 'dead' stars which have depleted their reserves of hydrogen. Their initial mass must be $\geqslant 20$ M$_\odot$ (e.g. Smartt, 2009) so that after mass reduction by stellar winds during the post-main sequence phase and supernova mass expulsion, the remnant will be $\gtrsim 3$ M$_\odot$ and collapse to a stellar mass black hole.

As stated above, super-massive black holes (SMBH) with mass range $M_{\rm BH} > 10^6$ M$_\odot$ have been shown to exist at the centres of most massive galaxies. These leviathans have predominantly been detected within quasars at moderate redshifts through surveys such as the Sloan Digital Sky Survey (SDSS); for example Ata et al. (2018) observed 147,000 quasars between $0.8 < z < 2.2$.

Intermediate-mass Black Holes

Intermediate-mass black holes (IMBHs) are compact objects, intermediate in mass between stellar mass black holes and super-massive black holes, i.e. 100 M$_\odot < M_{\rm BH} < 10^6$ M$_\odot$.

IMBH are theorised to form in a number of ways, but their mass range is highly suggestive that they formed in zero metallicity environments of pristine primordial gas, either directly collapsing (Bromm & Loeb, 2003) or as the remnants of the first, 'Population III' stars (Larson, 2003). Another possibility is formation through either 'fast'

or 'slow' mergers. The fast process ($t \lesssim 1\text{Myr}$) involves formation from runaway merging of massive (Pop III) stars in dense stellar cluster environments after a core collapse (Portegies Zwart & McMillan, 2002). The slower process ($0.1 \lesssim t \lesssim 1\text{Gyr}$) involves the repeated merging of mass segregated black holes in the centre of dense globular clusters (Miller & Hamilton, 2002), and although a core collapse is not necessary, an initial $M_{\text{BH}} \gtrsim 50$ M$_\odot$ is required to progress, as smaller remnants are likely to be dynamically ejected in three-body interactions (Heger & Woosley, 2002).

Detection of black holes in general has always been problematic as conclusive validation relies primarily upon stellar dynamics, i.e. measuring the influence the compact object has on its surroundings. First explored by Frank & Rees (1976) the gravitational 'sphere-of-influence' (SOI) of a black hole is defined as

$$R_{SOI} \approx \frac{GM_{\text{BH}}}{\sigma^2} \tag{1.1}$$

where σ is the velocity dispersion of the stars within that radius. As noted by Kormendy & Ho (2013), even for a supermassive black hole in the mass range 10^6 M$_\odot < M_{\text{BH}} < 10^9$ M$_\odot$ in a galaxy where the nuclear BH is $\sim 0.1\%$ $M_\star$, this radius would amount to only ≈ 1 to 100 pc. At distances encompassing the nearest clusters (e.g. Virgo $\sim$18 Mpc and Fornax $\sim$19 Mpc), from 1 to 20 Mpc, this would correspond to an angular separation of $\sim 0.1" - 1"$, suggesting resolution of system dynamics would be distance limited for all but the closest targets in a sample using this method of detection. Indeed, until HST and the advent of adaptive-optics, detecting the influence of a black hole on proximate stars was impossible. However, recent HST (Taylor et al., 2021b) and future JWST (Taylor et al., 2021a) imaging proposals, have been designed to observe nearby (Virgo cluster) CSS to allow stellar dynamical modelling which may provide evidence of the existence of IMBH in these systems.

Other means of detection include:

- Gas dynamics - Following the same principles outlined above but for gas emission lines, with the advantage that gases are more likely to reach closer to the innermost stable circular orbit (ISCO) around the BH. However, the uncertainties here are increased because orbiting gas has a lower momentum and hence higher probability of following a non-Keplerian orbit (Kormendy & Richstone, 1995).

- Millisecond Pulsar timing - The pulse rate of fast spinning neutron stars which emit radio or microwave radiation from their jets can be measured very accurately. As the 'run-down' is influenced by the strong gravitational field of a BH, changes in timing of pulsars in the vicinity of a BH can thus be used to 'map' the local gravitational fields and intimate the presence of a BH (e.g. Devecchi et al., 2007).

- Reverberation Mapping - If a BH is 'accreting' matter, as illustrated in Fig. 1.3, the accretion disc will emit continuum radiation which is effectively centrally produced. The area surrounding the accretion disc, which is still influenced by the BH's gravity, will emit through emission lines of gases excited by the continuum radiation. The width of the spectral features in this 'broad-line region' (BLR), as indicated in Fig. 1.3, give the velocity of the gases. Variations in accretion onto the BH will be reflected in corresponding changes in intensity of both the continuum and BLR emissions, but with a time delay corresponding to the radius of the BLR (Peterson

& Horne, 2004). The BH mass is then given by

$$M_{\text{BH}} \approx \frac{f R_{BLR} \sigma^2}{G} \tag{1.2}$$

where f is a virial factor, associated with the geometry and orientation of the BLR.
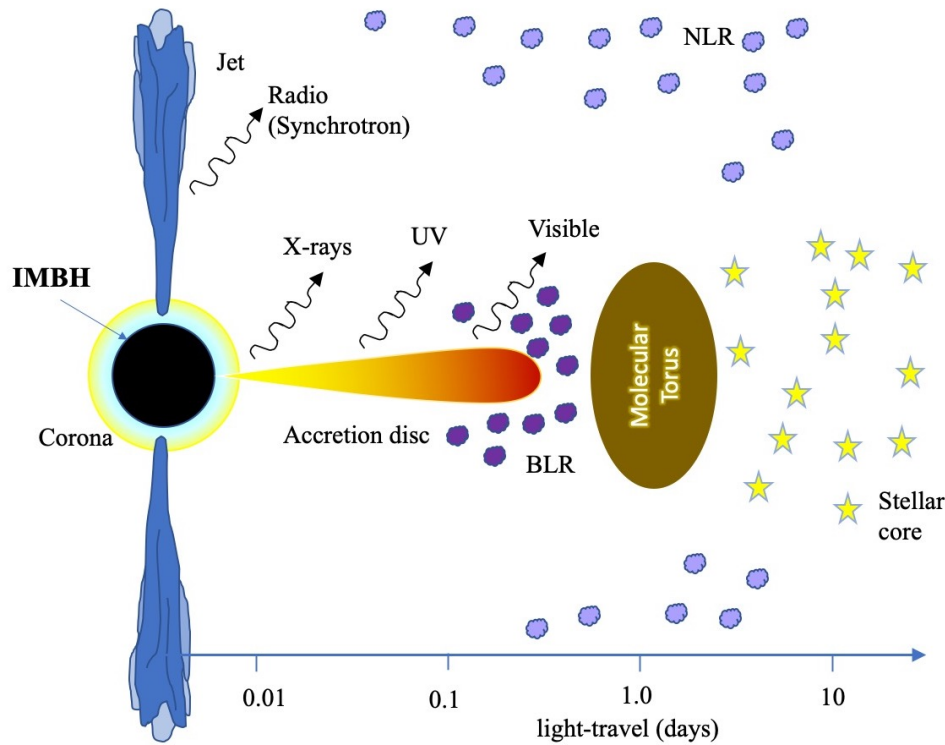
Figure 1.3: Simple illustration of the structure of an accretion disc around an intermediate mass black hole, showing possible emission sources, in addition to the broad-line region which is within the SOI of the black hole's gravity. (credit: Author)

- The Fundamental Plane of Black Hole Activity - if a BH is in an accreting state, it may emit a broad spectrum of radiation. Merloni et al. (2003) defined the fundamental plane of black hole activity, noting the relationship between X-ray luminosity, radio luminosity and BH mass, given by

$$L_{\text{R}} = (0.60^{+0.11}_{-0.11}) \log L_{\text{X}} + (0.78^{+0.11}_{-0.09}) \log M + 7.33^{+4.05}_{-4.07} \tag{1.3}$$

- Gravitational waves - In the last few years, it has become possible to detect ripples in the fabric of spacetime which arise from the merger of massive compact objects, as predicted by General Relativity (Einstein, 1916). The first such detection was made by the LIGO and Virgo Collaboration in 2015 (Abbott et al., 2016). More recently, the same team (Abbott et al., 2020) announced the detection of a binary merger of BHs with masses 85^{+21}_{-14} M$_\odot$ and 66^{+17}_{-18} M$_\odot$ resulting in a final remnant mass of 142^{+28}_{-16} M$_\odot$ - the first conclusive detection of an IMBH. Many more have been found in data over the last few years with a total of 8 events resulting in total masses over 100 M$_\odot$ having been detected to March 2022. Nevertheless, the nature of LIGO is such that it is optimised to detect relatively high frequency

strain sources, according to LIGO Scientific Collaboration et al. (2015) from 10-7000 Hz, typical of stellar mass BH binary mergers at low redshift. Detection of the gravitational wave energy from more massive IMBH mergers at higher redshifts, and so called extreme mass-ratio inspirals (EMRI), for example, between neutron stars and IMBH, will have to wait at least a decade for the Laser Interferometer Space Antenna (LISA) (Baker et al., 2019).

In summary, there are a variety of ingenious methods, but also substantial challenges to detecting black holes. This is especially true under circumstances where they are distant or lower-mass objects where it may be impossible to resolve spectra from stars or gas within the SOI, or when they are not accreting (quiescent) and hence low-luminosity. The latter is particularly true of CSS and particularly GCs due to the gas-free nature of these system (e.g. Miller & Hamilton, 2002). Nevertheless, as this project will attempt to detect the presence of IMBH in CSS, we will next review the structure of accretion discs and the potential of detecting the emissions from transient and tidal disruption events (TDEs).

1.3   Accretion Discs

The potentially radiant structure around a 'feeding' black hole, is known as an accretion disc. In general, a disc structure of material will tend to form in any gravitationally contracting system as angular momentum is conserved, and the plane of the rotationally supported disc that forms to arrest the collapse, holds the memory of the average angular momentum from the initial system. A simplistic view of an accretion disc is shown in Fig. 1.3, where as matter spirals into the potential well of the compact object, turbulence enhanced viscous stresses cause angular momentum transferal out (Shakura & Sunyaev, 1973) and increasingly energetic radiation emissions towards the centre. Close to the black hole, magnetic fields, threading through the ionised matter, are thought to add further energy to the particles, some of which accelerate away from the poles of the black hole as jets.

Much has been written about accretion discs, since Shakura & Sunyaev (1973) defined a thin-disk model for accreting matter and there now exist four main disk models: 'thin' (Shakura & Sunyaev, 1973),

Figure 1.4: Luminosity vs. mass accretion rate for differing disc types. Assumes $\dot{M}_{\rm Edd} \equiv L_{\rm Edd}/0.1c^2$ - i.e. 10% matter conversion efficiency. The thick discs have the highest mass accretion rates and are brightest, but are Eddington limited due to pressure gradients (credit: Ulmer, 1999).

'slim' (Abramowicz et al., 1988), 'thick' (Paczyński & Wiita, 1980) and advection-dominated accretion flow (ADAF) (Narayan & Yi, 1994). As noted by Abramowicz & Fragile (2013) in their review, these correspond to different parameter spaces as shown

Table 1.1: Accretion disc models, based around different parameter spaces; disc rotation / pressure or accretion rate / opacity. Reproduced from Abramowicz & Fragile (2013).

	Fast rotation (disc)	Slow rotation (Bondi)
Large pressure	**slim, thick**	**ADAF**
Small pressure	**thin**	**free-fall**
	High accretion rate	Low accretion rate
Large opacity	**slim, thick**	**thin**
Small opacity	**-**	**ADAF**

in Table 1.1.

The type of disc which forms will also affect the luminosity, due to the availability of matter for accretion as illustrated in Fig. 1.4. As summarised in Ulmer (1999), the discs with the highest luminosity are those with the greatest mass accretion rates. These types of disc are both geometrically and optically thick. As originally explored by Paczyńsky & Wiita (1980), despite the highest accretion rates, thick disc luminosity is likely to be only marginally super-Eddington due to increased pressure gradients forcing the inner radius of the disc closer to the Innermost Stable Circular Orbit (ISCO)[1]. After this point matter spirals rapidly into the black hole without releasing binding energy through accretion, i.e. accretion efficiency $\eta \ll 0.1$.
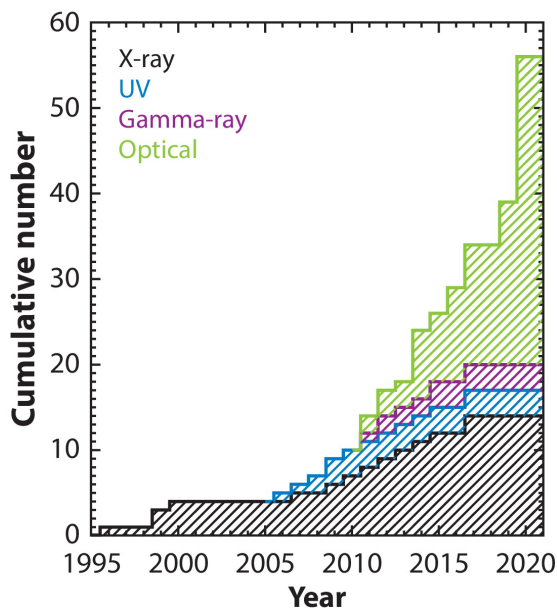
Figure 1.6: The cumulative discovery history of TDEs, showing the wavelength in which they were discovered. (credit: Gezari, 2021).

As originally explored by Shakura & Sunyaev (1973), thin discs do not radiate as brightly, with their luminosity increasing linearly with mass accretion rate, but have the highest accretion efficiencies ($\eta \sim 0.1$). Slim discs can be thought of as bridging the gap between the thin and thick discs ($\eta < 0.1$). Advection-dominated (ADAF) discs are optically thin and radiate inefficiently. Due to the lower density of material, thermal energy generated through friction and viscosity is 'advected' inwards with the matter flow without being radiated away, meaning only 1% or less of the matter is converted to energy ($\eta \lesssim 0.01$) before falling into the event horizon (Narayan & McClintock, 2008).

These accretion disc models represent a 'steady-state' of accretion, but the situation for TDEs is potentially more complicated due to the initial formation process of an accretion disc from gas distended into what may be a highly eccentric orbit as the star is disrupted. TDE observations support a mechanism where X-ray and optical emissions are mutually exclusive (e.g Saxton et al., 2019) and there are two main schools of thought regarding the physical processes which give rise to this effect. It is possible

---

[1]For a non-spinning (Schwarzschild) BH, the $R_{ISCO} \simeq 4R_S$ - see Eq. (1.5)

X-ray and UV emissions are reprocessed to optical and IR through adiabatic cooling and photo-ionisation (e.g. Strubbe & Murray, 2015; Dai et al., 2018) and as illustrated in Fig. 1.5, have a high dependency on the angle of inclination of the disc to the observer. Alternatively, Piran et al. (2015) have argued that UV and optical emissions occur due to shocks between streams of matter when the accretion disc is initially forming from gravitationally bound material, and the X-ray emissions result from the later accretion of the same material onto the black hole.

Irrespective of the correct model, the probability of detecting these, and many other transient events is increasing with the advent of robotic telescopes, global networks and greater computing power allowing automated data analysis (e.g. Brown et al., 2013) as detailed in §2.2. This is illustrated in Fig. 1.6 which shows that TDE discoveries are increasing across all wavelengths. Interestingly, since real-time optical surveys have been viably implemented over the last decade, the total of optical TDEs detected has surpassed the total detected in all other wavelengths. For example, during the first 18 months of operation of the Zwicky Transient Facility (ZTF - see §2.3), from the beginning of 2018, 17 TDEs were detected, substantially increasing the sample of TDEs available for analysis (van Velzen et al., 2021). Up to March 2022, there were 98 TDEs and candidates reported on James Guillochon's Open TDE Catalog[2].

---

[2]https://tde.space
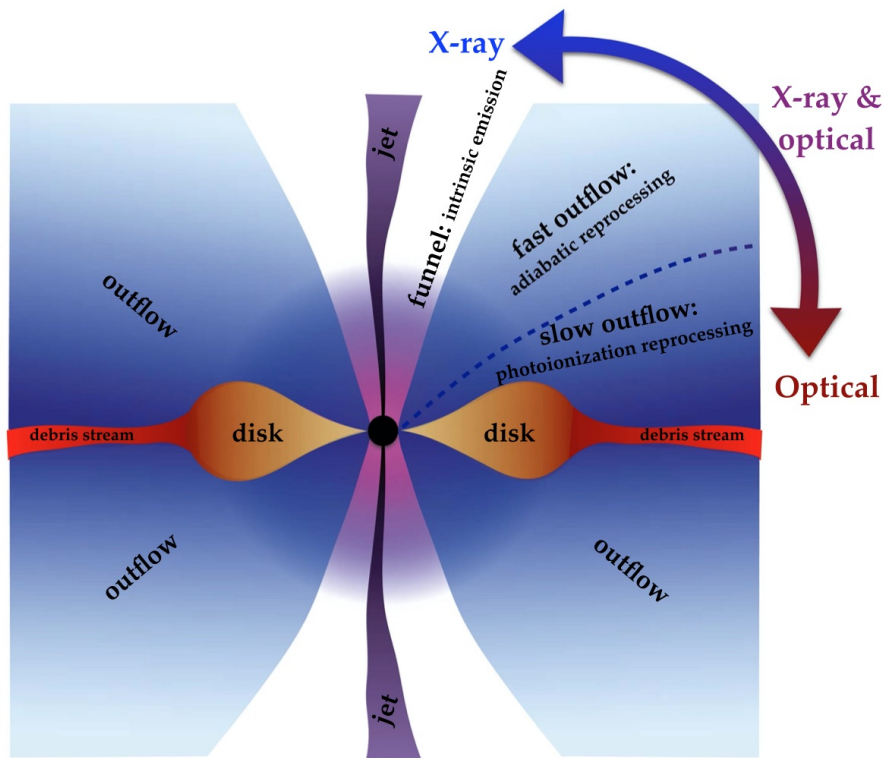
Figure 1.5: Schematic of a black hole accretion disc, showing winds and outflows and their influence on spectral features close in to the compact object. Also shown is the dependence of the observed output on inclination to observer, specifically as expected for a tidal-disruption event (TDE). Only when viewed along the optically thin funnel, are the intrinsic X-ray/EUV emissions of the disc observed. Note although a jet is shown, it is thought these are rarely seen in TDEs. (Credit: Dai et al., 2018)

1.4 Tidal Disruption Events

As discussed in §1.2 above, in dense stellar systems such as GCs or CSSs being considered, it is possible that a nuclear black hole exists. Over time, denser stars will migrate to the centre of the cluster due to mass segregation (Portegies Zwart & McMillan, 2002). When a star ventures too close to a massive compact object, i.e. within a tidal radius defined by Rees (1988) as

$$R_{\mathrm{T}} \simeq \left(\frac{M_{\mathrm{BH}}}{M_{\star}} \right)^{\frac{1}{3}} R_{\star} \tag{1.4}$$

the gravity of the black hole will overcome the self-gravity of the star and disrupt it, extending the gaseous envelope of the star (e.g. Frank & Rees, 1976; Evans & Kochanek, 1989) and see Fig. 1.7. It is thought that this process, known as a tidal disruption event (TDE) (Hills, 1975) might initially produce a brief high energy accretion flare from bound gas, while the unbound material is ejected from the system. Approximately 50% is thought to settle into an accretion disc and is consumed over time (Rees, 1988). Interestingly, given the Schwarzchild radius of a black hole is defined as

$$R_{\mathrm{S}} = \frac{2GM}{c^2} \tag{1.5}$$

the tidal radius of a black hole $M_{\mathrm{BH}} \gtrsim 3 \times 10^8$ M$_{\odot}$ will be inside the event horizon, meaning the larger the black hole, the more likely (a solar mass) star will be devoured 'whole' without any TDE emissions (Hills, 1975).

This is advantageous in the search for IMBH as although the gravity field is weaker for the lower-mass compact objects, any disruption events which are detected have to be a consequence of this mass-range of objects.

The probability of a star being involved in a TDE increases in a high-density environment such as those found in CSS. As detailed by Frank & Rees (1976) one of the factors determining the rate of TDEs is the frequency with which stars wander into the loss cone of a central BH. The probability of stars entering the loss cone increases in proportion to the sphere of influence of the BH, which is $\propto M_{\mathrm{BH}}$, as well as the central stellar density and distribution. Similarly, since the tidal radius is a function of both the mass of the black hole, and the type (density) of the star involved in the encounter, we should note that white dwarf compact remnants, which may be prevalent in the core of a GC or CSS due to mass segregation, would not be disrupted by a BH $M_{\mathrm{BH}} \gtrsim 10^5$ M$_{\odot}$ (MacLeod et al., 2014). This is because they would be swallowed whole by BHs over this mass as the tidal disruption radius R_{T} for objects of this type is within the Schwarzchild radius. The above constraints and others are illustrated in Fig. 1.8 which shows the limit of TDE parameter space based on star mass, evolutionary state and the mass of the disrupting BH. As shown, the strength of the tidal encounter is defined by the parameter $\beta = R_{\mathrm{T}}/R_{\mathrm{P}}$, where R_{T} is the tidal radius (Eq. (1.4)) and R_{P} is the radius of periapsis, or closest approach of the star to the BH. As shown in Fig. 1.9, variation in these impact parameters will result in variation in the peak luminosity and duration of the flare in addition to the profile. The next section will go into more detail on modelling the energy output for TDEs involving IMBH.
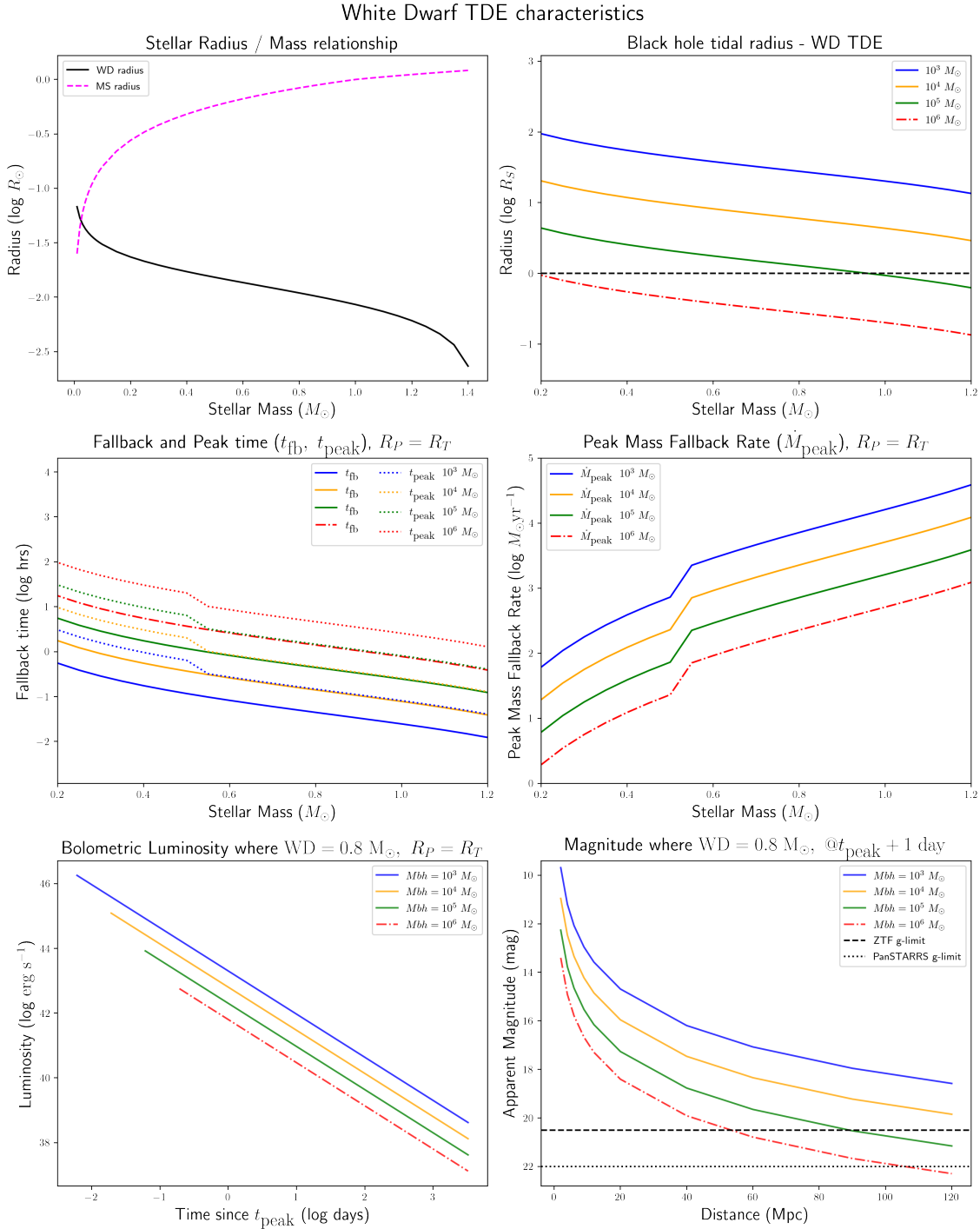
Figure 1.7: Characteristics of TDEs involving WDs and IMBHs. (Top left) Comparison of WD and main sequence (MS) star radius / mass. (Top right) Tidal radius for WD TDE encounters with IMBH - dotted line shows Schwarzchild radius within which a star would be consumed without disruption. (Centre left) Fallback and peak time for the disruption, where periapsis radius equals the tidal radius ($R_P = R_T$) i.e. the strength of the encounter, $\beta = 1$. (Centre right) Peak mass fallback rate, from which the accretion rate is derived. (Lower left) Bolometric luminosity estimates for 0.8 $M_\odot$ WD. (Lower right) Apparent (visual) magnitude for 0.8 $M_\odot$ WD encounter, showing magnitude 1 day after peak. ZTF and PanSTARRS limiting magnitude (g-mag) shown for reference.
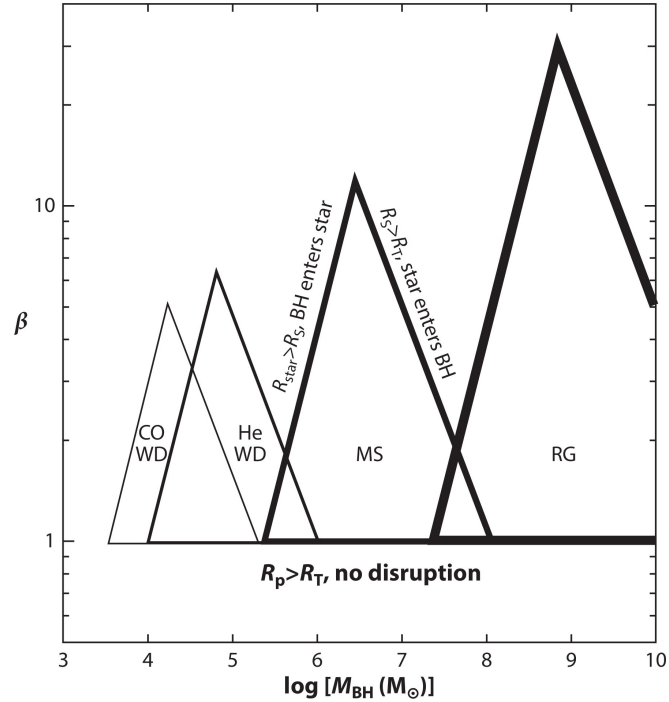
Figure 1.8: Constraints on TDEs as a function of star mass/evolution and BH mass. R_T is the tidal radius, R_P is the periapsis of the encounter and R_S is the Schwarzschild radius. $\beta = R_T/R_P$ which defines the strength of the tidal encounter. Evolutionary states shown are 0.6 $M_\odot$ carbon/oxygen white dwarf (CO WD), 0.17 $M_\odot$ helium white dwarf (He WD), main sequence (MS) and red giant (RG). (credit: Gezari, 2021).
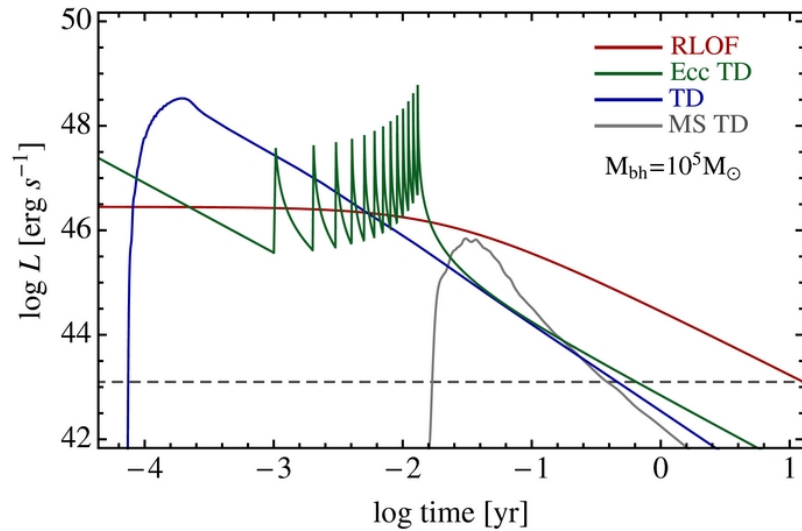
Figure 1.9: Effect of variation in orbital parameters on accretion flare luminosity. Simulated light curve for TDE of a 0.5 $M_\odot$ WD by a 10^5 $M_\odot$ BH, showing luminosity assuming $0.1\dot{M}c^2$ conversion efficiency. The blue line shows the disruption when $R_p = R_t$, the green line shows repeated flaring in the event the WD is on an eccentric orbit. The red line shows a gradual Roche lobe overflow (RLOF). The gray line shows the luminosity from the disruption of a 1 $M_\odot$ main-sequence (MS) star. The dashed line gives the Eddington luminosity for a 10^5 $M_\odot$ BH. As expounded in the text, the scenario where $R_p = R_t$ (blue line) has been analysed, but the RLOF and eccentric orbit TDEs may also present with sufficient luminosity and period to be detectable. As CSS are unlikely to contain any 1 $M_\odot$ MS stars, and lower-mass MS disruptions would be lower luminosity (credit: MacLeod et al., 2014; Guillochon & Ramirez-Ruiz, 2015)

13

Modelling a TDE

Historically, much analysis carried out, and in fact the classical definition of a TDE from authors such as Rees (1988), consider the characteristics of an event where an SMBH of $10^6 \, \mathrm{M_\odot} \lesssim M_{\mathrm{BH}} \lesssim 10^8 \, \mathrm{M_\odot}$ interacts with a main sequence solar mass star. As this mass of black hole is greater that the mass we expect to find in a CSS or GC (on the basis of the M_{BH} scaling relationships) we shall therefore consider how a TDE might scale to an IMBH. Additionally, unless formed from tidally stripped dwarf cores, CSS and GCs are 'redder' than normal galaxies due to their age, and are less likely to contain many, if any, stars of solar mass, as these would long ago have left the main sequence. We will, therefore, conjecture the characteristics of a TDE involving an IMBH and a white dwarf (WD). The following modelling is illustrated throughout in Fig. 1.7. Several authors have considered this scenario, both observationally (e.g. Krolik & Piran, 2011) and numerically (e.g. Haas et al., 2012; MacLeod et al., 2014).

When determining the emissions observable from a TDE there are a number of factors to consider. Firstly, as outlined by several authors in their simulations and analysis, (e.g. Ulmer, 1999; Guillochon & Ramirez-Ruiz, 2013; Malyali et al., 2019), a key factor of the emission is determined by the mass fallback rate, $\dot{M}_{\mathrm{fb}}$, which in turn is a function of the fallback time t_{fb}, the time $\sim 50\%$ of matter which remains gravitationally bound to the BH after the initial disruption takes to return to the radius of pericentre, r_{p}. Taking a simplistic view, i.e. assuming Keplerian orbits and ignoring relativistic effects, such as that described by Malyali et al. (2019) we find that

$$t_{\mathrm{fb}} \simeq \frac{r_{\mathrm{p}}^3}{\sqrt{GM_{\mathrm{BH}}}R_\star^{3/2}} \tag{1.6}$$

and from this the mass fallback rate, $\dot{M}_{\mathrm{fb}}$, which is determined by the type (density) of the disrupted star, and thus the energy distribution of the disrupted matter stream, is given by

$$\dot{M}_{\mathrm{fb}} = \frac{1}{3}\frac{M_\star}{t_{\mathrm{fb}}}\left(\frac{t_{\mathrm{fb}}}{t}\right)^{5/3} \tag{1.7}$$

with a peak fallback rate, $\dot{M}_{\mathrm{peak}}$, being approximately

$$\dot{M}_{\mathrm{peak}} \approx \frac{1}{3\delta^{5/3}}\frac{M_\star}{t_{\mathrm{fb}}} \tag{1.8}$$

where δ is a factor determined by the structure (i.e. density and mass) of star, and for a WD is taken as $\delta \approx 3.3$ for $M_{\mathrm{wd}} > 0.5 \, \mathrm{M_\odot}$ (Evans & Kochanek, 1989) or $\delta \approx 5.5$ for $M_{\mathrm{wd}} \leqslant 0.5 \, \mathrm{M_\odot}$ (Lodato et al., 2009).

Initial analyses of TDEs assumed that the mass accretion rate, $\dot{M}_{\mathrm{acc}}$, would closely track the mass fallback rate, however, more recent studies have questioned this assumption (e.g. Bonnerot et al., 2016). Accretion onto the black hole occurs when the gravitational energy is converted into radiation as the matter stream loses angular momentum, but for this to happen efficiently, the initially eccentric orbits of matter have to circularise (e.g. Rees, 1988; Ulmer, 1999; Lodato & Rossi, 2011; Guillochon & Ramirez-Ruiz, 2013). If the stream of disrupted matter has low viscosity, then the energy dissipation per orbit is low. Additionally, as noted by Guillochon & Ramirez-Ruiz (2015), for a rotating (Kerr) black hole, relativistic precession causes the debris stream to wind through multiple orbits without intersecting, therefore extending the time before accretion begins and a flare is

observable. For low mass black holes $M_{\text{BH}} \lesssim 10^6$ M$_\odot$, they also suggest this reduces the flare luminosity by an order of magnitude.

As discussed by, MacLeod et al. (2014) for a thick disc where the viscous time[3] is greater than the fallback time, this means the mass accretion rate is determined largely by the rate at which the material viscously expands and is given by

$$\dot{M}_{\text{acc}} = 0.1\dot{M}_{\text{peak}} \left(\frac{t}{t_0}\right)^{-4/3} \tag{1.9}$$

where the 0.1 factor relates to the order of magnitude luminosity reduction of the flare suggested by Guillochon & Ramirez-Ruiz (2015) noted above, and t_0 is roughly the viscous time at the pericentre for a thick disk. The above does not take any wind-induced mass loss into account and, as noted by MacLeod et al. (2014), the evolution of the decay would become steeper as a result of any mass loss which occurred, perhaps becoming closer to the -5/3 traditionally quoted for TDE decay rates.

Taking this as the accretion rate from an encounter, and assuming a matter conversion efficiency of 10% we arrive at a luminosity for the encounter of

$$L_{\text{bol}} = 0.1\dot{M}_{\text{acc}}c^2 \tag{1.10}$$

As this is the bolometric luminosity from the matter converted, we need to correct this to optical magnitude. Estimates of bolometric correction κ_ν for accretion disc emissions have been detailed by several authors, For example, Kaspi et al. (2000) estimated a rough optical (510 nm) to bolometric luminosity correction of $\kappa_{510} \sim 9$, and similarly Cheng et al. (2019) estimated $\kappa_{510} \sim 12$, where $\nu L_{510} = L_{\text{bol}}/\kappa_{510}$. It was noted that both these were based on an analysis of AGNs with masses upwards of 10^6 M$_\odot$, so the validity of this correction at lower masses is uncertain. Nevertheless, taking the more recent estimate from Cheng et al. (2019), and the maximum luminosity from our examples of a 0.8 M$_\odot$ WD encountering a 1000 M$_\odot$ BH, 1 day after peak we can estimate a $L_{\text{bol}} \approx 10^{43}$ erg s^{-1}, gives a visual luminosity of

$$L_v = L_{\text{bol}}/12 \approx 10^{42} \text{ erg s}^{-1} \tag{1.11}$$

We can convert this to a rough absolute magnitude for comparative purposes from

$$M_v = -2.5\log_{10}L_v + L_0 = -16.8\text{mag} \tag{1.12}$$

where $L_0 = 71.197$ is the zero point luminosity, i.e. 3.0128×10^{28}watts (Mamajek et al., 2015). At a distance of 120 Mpc this would equate to an apparent magnitude of $\sim$18.4 which is within the limiting magnitudes of the optical facilities proposed, and discussed in §2.2. It should be noted that for this particular scenario ($M_{\text{BH}} = 1000$ M$_\odot$, $M_{\text{WD}} = 0.8$ M$_\odot$, $R_P = R_T$, $t = t_{\text{peak}} + 1$ day) the decay is fast and after 10 days the magnitude would be marginal in the optical facilities considered (i.e. decrease to $\sim$21.9 mag). This appears to be a feature of WD TDEs (i.e. fast and bright) in comparison to TDEs involving MS stars of the same mass, which tend to be lower luminosity ($\sim$1 dex) at peak, but remain at that peak for longer. A more robust comparison between WD and MS encounters with IMBH would be a useful follow-up.

In summary, there are many parameters which determine the spectrum, profile and visibility of a TDE, not the least of which is the environment being considered, which will

---

[3]The viscous time-scale is a characteristic time in which angular momentum distribution changes.

clearly impact the probability of the event occurring in the first instance. CSS and GCs are dense stellar environments which are conducive to dynamical encounters, with TDEs involving a putative nuclear BH included in this potential. The above analysis indicates that TDEs involving WD and IMBH should be detectable in optical bands, although these encounters do not remain visible for more than a few weeks at best. Also, a lack of larger MS stars ($M_\star \geqslant 1~\mathrm{M}_\odot$) in these older clusters may limit the possibility of detecting these events in optical at distances greater than a few tens of Mpc. Detection at shorter wavelengths (e.g. X-ray, γ-ray), where luminosities are higher, and all-sky monitoring of fast bursts is carried out, would increase the probability of detection.

Chapter 2

Background

2.1 Approach and Data Samples

The search for transient signals in CSS was split into three different approaches which relied upon two data products available from the ZTF, in combination with data marshalled from two different sources. The data sources chosen gave the possibility to search for transients in both literature defined CSS source positions, as well as indefinite source positions within potential CSS hosting environments, thus spanning a greater volume. It was believed this would give the best opportunity to locate a transient signal following a robust and methodical process which was extensible as new ZTF data releases came online. The data sources were a CSS catalogue compiled from literature sources providing the known positions, and a 'local' (<120Mpc) galaxy catalogue which could be used to perform a proximity search. The approaches taken were inspection of light curves and a search for transient alerts. This gave the three approaches as follows: -

- CSS Catalogue - light curves

- CSS Catalogue - alerts

- Local galaxy proximity - alerts

For reference, the other option i.e. the combination of local galaxy proximity objects and light curves, was not considered feasible due to light curves being correlated with existing reference objects, and thus the volume of data was considered too great to handle, although the author notes this would make a good future project. The ZTF data products, i.e. the multi-epoch light curves and the transient alerts, are discussed in more detail in §2.3.1, but it should be noted that (at this stage) the ZTF only complete systematic light curves for known reference objects.

2.1.1 Data Samples

The dual approach to source position searching provided a wide range of opportunities for detection of transient signals. It should, however, be noted that both selections employed have varying benefits. For instance, the literature CSS selection provides positional information for objects which other authors have determined to be CSS through a number of robust methods, but which are limited to a few focused surveys, predominantly around large galaxy clusters. On the other hand, the search for sources in proximity to local galaxies should extend the search to a defined local volume, but the nature of the

sources would be less well understood, so additional validation of any candidates would be required.

CSS Catalogue

To search through archival data for evidence of potential TDEs, the positions of known CSS from the literature were required. An initial catalogue of positions had been collated by my supervisor, Dr. Mark Norris (UCLan), over a number of years from the Archive of Intermediate Mass Stellar Systems project (AIMSS, Norris et al., 2014) and publications contained therein. Additional literature data up to ~2016 was added by David Glass (UCLan), but my initial task was to bring this as up to date as possible, i.e. to include data up to 2020, and ensure the data entries were fully referenced.

Data associated with existing entries were found, and this was used to augment existing entries. As far as possible, duplicate entries were consolidated, based on positional ($< 1''$) and nomenclature comparisons from different surveys. Parameters associated with the lowest uncertainty measurements were used where duplicate readings were located, for example, where multiple photometry existed in certain filter bands from separate surveys.
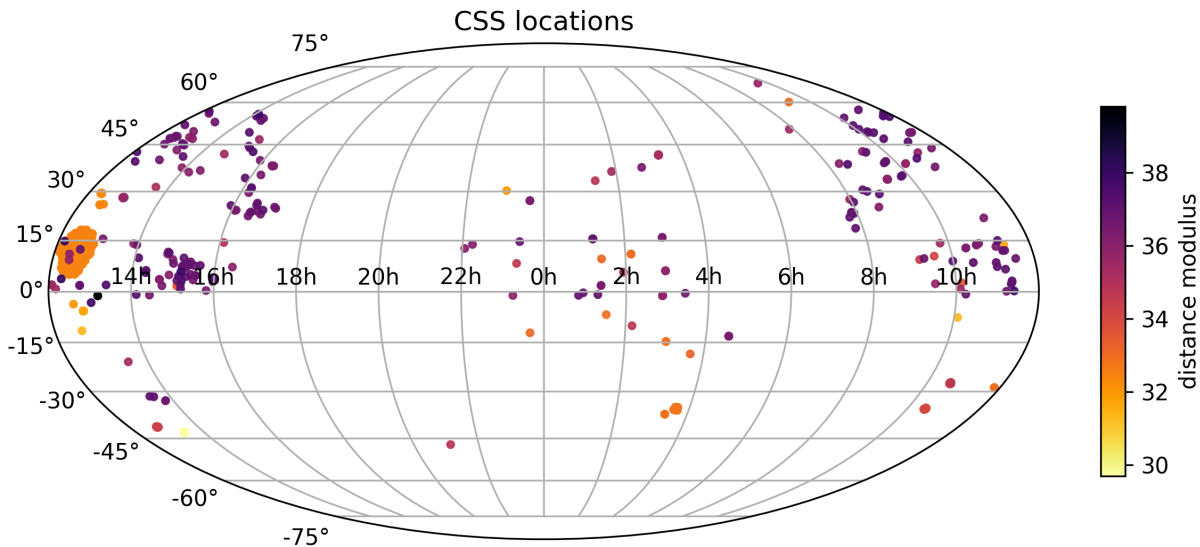
Figure 2.1: CSS catalogue sky location (Mollweide projection). The large clump at 12h07m<RA<12h54m, 4°53′<Dec<18°10′ consist of entries in the Virgo cluster from authors over many years, and augmented by the NGVS, accounting for almost 50% of the data. It was also noted that several entries shown, with Dec<−30° would not have ZTF imaging available due to its northern latitude location, including those in the Fornax, Antlia and Centaurus clusters.

The GC and CSS objects amounted to 1484 data entries and the sky position of these objects is as shown in Fig. 2.1. The large number of surveyed objects (clump at RA:12h07m, Dec:11°30′) shows the extent of CSS within the Virgo cluster. Additionally, the author noted that objects below ~Dec−30° would not be visible to the ZTF due to its northern latitude location (~33°N - see Table 2.7).

Local Galaxy Proximity

The local galaxy data consisted of an extract of positions of galaxies from the Hyperleda database [1] (Makarov et al., 2014). To obtain a sample which could be used for a practical search for alerts, a number of criteria were set using available parameters in the online query.

- *objtype* = 'G' - ensure the nature of the object is defined as a galaxy

- *modbest* between 26.5 and 35.4 - the best estimate of distance modulus, from either distance measurements or cosmological radial velocity with ΛCDM, to give a distance range $2 \leqslant D \leqslant 120$ Mpc. The lower limit takes the sample just outside of Andromeda (M31) to reduce clutter and filtering of oversize objects. The upper limit for the host galaxies was set to allow reasonable coverage of CSS objects down to an absolute magnitude of $\sim$-15 mag, thereby ensuring visibility of targets around the selected hosts to a limiting magnitude of $\sim$ 20.5 mag.

- *de*2000 > -30 - This limit on declination δ was imposed by the use of the ZTF facility and its northerly latitude.

- $-(modbest-bt) < -20$ - Using the apparent *b* magnitude (*bt*) and distance modulus to convert to an absolute *B*mag. Using this lower magnitude limit ensured rejection of smaller galaxies without significant GC populations.

Table 2.1: Description of columns downloaded from HyperLEDA database

Field	unit	Description	minimum	maximum	count
objname		Principal name	N/A	N/A	4812
al2000	hrs	RA (J2000)	0.0005	23.9987	4812
de2000	deg	Dec (J2000)	-29.9601	86.7385	4812
t		Morphological type code	N/A	N/A	4722
type		Morphological type	N/A	N/A	4722
v	km/s	Mean Heliocentric radial velocity (cz)	-291.8	8819.6	4812
e_v	km/s	Error on v	0.4	2426.6	4810
d_hf	Mpc	Hubble flow distance (v/70)	3.4	126	4812
bt	mag	Apparent B-magnitude	7.817	15.371	4812
e_bt		Error on bt	0.02	2.333	4812
babs	mag	Absolute B-magnitude	-20.0	-22.62	4812
it	mag	Apparent I-magnitude	7.030	15.765	3394
e_it	mag	Error on it	0.027	2.521	3394
ut	mag	Apparent U-magnitude	7.847	23.119	2410
vt	mag	Apparent V-magnitude	7.214	16.076	1226
modbest		Best distance modulus, combining mod0 and modz	28.450	35.393	4812
e_modbest		Error on modbest	0.010	1.127	4812
d_l	Mpc	Luminosity distance	4.9	119.9	4812
logd25	log(0.1')	log of apparent diameter (d25 in 0.1')	0.238	2.380	4719
hl_names(pgc)		Comma separated list of all the designations for the object "pgc"	N/A	N/A	4812

The data requested from the Hyperleda database was returned in the format shown in Table 2.1. To calculate the total number of globular clusters N_{GC} within the surveyed

---

[1]http://leda.univ-lyon1.fr/

region, this data was also augmented with an estimated specific frequency S_{N}. This was determined following the same process Peng et al. (2008) outlined for their Virgo cluster (ACSVCS) sample, using the relation detailed in Harris & van den Bergh (1981) between the number of globular clusters and galaxy V-band luminosity as shown in Eq. (2.1).

$$S_{\text{N}} = N_{\text{GC}} \times 10^{0.4(M_{\text{V}}+15)} \tag{2.1}$$
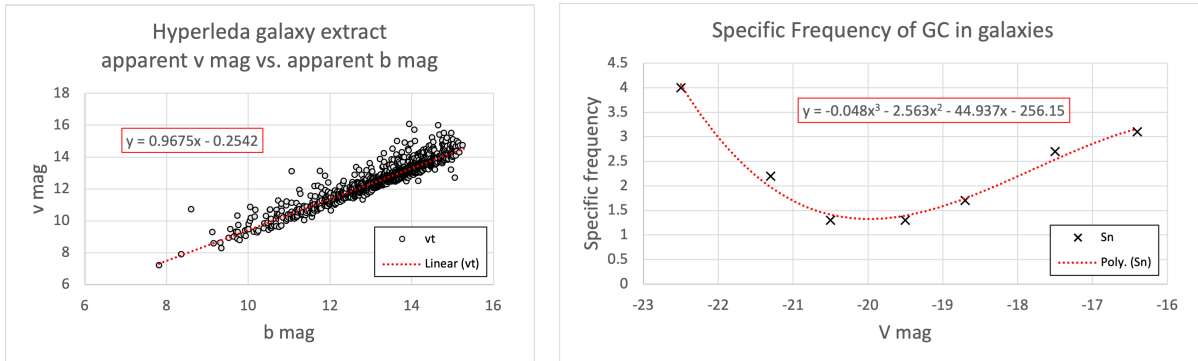
(a) Hyperleda galaxy extract, apparent V mag vs B mag. $\sim$25% of entries had existing measured values, so a simple linear interpolation from these was used to estimate absent V mag values.

(b) Specific frequency, S_{N}, defined by Harris & van den Bergh (1981), of globular clusters from bins measured by Peng et al. (2008). S_{N} is numbers of clusters per unit galaxy luminosity. A fit to a arbitrary polynomial was made for intermediate values.

Figure 2.2: Data used in estimation of numbers of GCs per galaxy from the Hyperleda sample.

As not all galaxies had measured m_{V} mag data available, a linear relationship between m_{B} and the existing m_{V} data was estimated to determine absent values, as shown in Fig. 2.2a. Using these measured or estimated values and the distance modulus, the absolute M_{V} was used to determine the specific frequency S_{N} using a trend as determined by Peng et al. (Table 3, 2008) from sample bins for their ACSVCS galaxies (see Fig. 2.2b). Rearranging Eq. (2.1) to estimate the total number of GCs hosted by a galaxy gave

$$N_{\text{GC,Total}} = \sum \frac{S_{\text{N}}}{10^{0.4(M_{\text{V}}+15)}} \approx 3.8 \times 10^6 \tag{2.2}$$

While the total number of GCs is interesting, a more relevant parameter for our purposes was an estimate of the count of visible systems. As the GCLF is close to a Gaussian[2], there will be a large number of systems at lower luminosity which are below a threshold limiting magnitude of the observation. For the purposes of this process the PanSTARRS g-filter limiting magnitude of 22 mag was used. As discussed in Chapter 5 PanSTARRS imaging was used as it had greater depth than the ZTF science images, and more consistent coverage compared to HST imaging.

Based on fig.9 and fig.11 from Jordán et al. (2007), we can obtain the mean (μ_G) magnitude and dispersion (σ_G) of a Gaussian for the GC distribution in relation to the absolute B magnitude of the galaxy, i.e.

$$\mu_G = 7.2 \text{ mag} \tag{2.3}$$

---

[2]Not an unreasonable assumption, although Jordán et al. (2007) argue an evolved Schechter function is a better fit, especially at the lower mass end.

$$\sigma_G = 1.14 - (0.1 \times M_{\text{B,gal}})^3 \tag{2.4}$$

noting that for our purposes a constant mean and linear dispersion relationship was considered adequate.
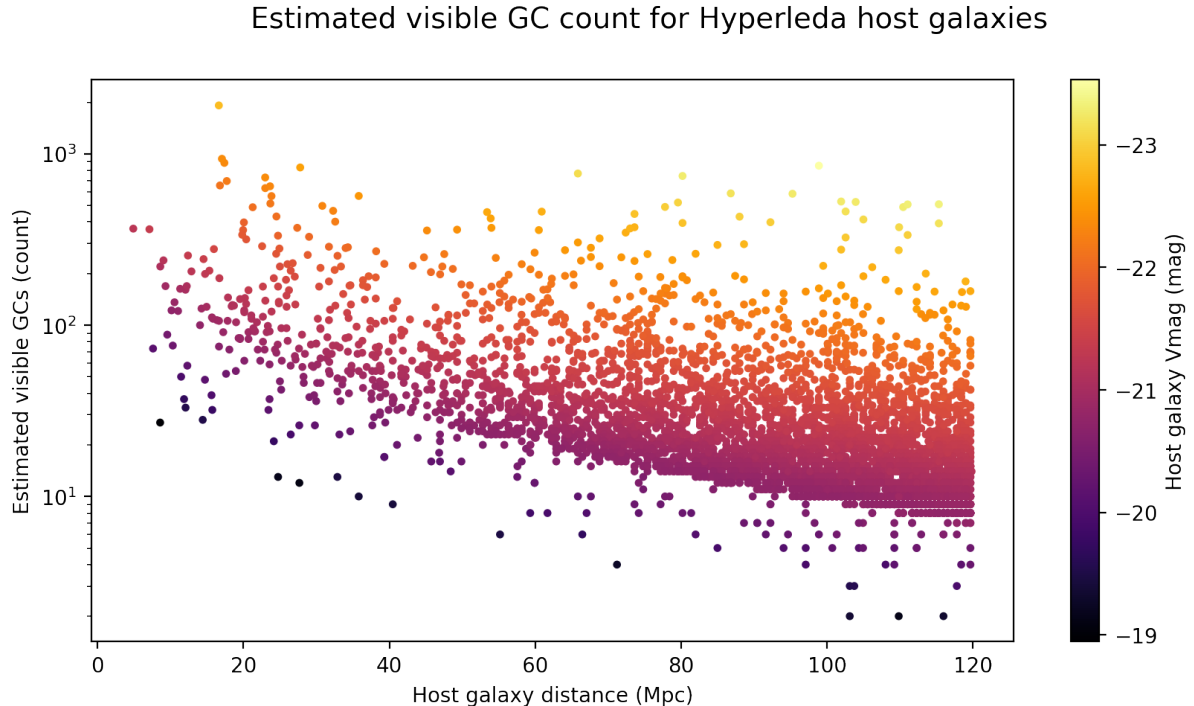
Figure 2.3: Estimated GCs hosted by galaxies in Hyperleda extract, visible in PanSTARRS *g*-filter, with a limiting magnitude of 22 mag. Estimated using Monte Carlo simulation for each host as described in the text. The count of GCs visible (log scale) is shown against host galaxy distance (from distance modulus) and shaded by luminosity (V mag).

As we were interested in the visibility of GCs in PanSTARRS, with a *g* mag limit of 22 mag, we converted the mean absolute magnitude (see Eq. (2.3)) to an apparent magnitude, μ_g, using the distance modulus, which had been used to determine the distance for the galaxy in the first place. So, a mean absolute magnitude of $\mu_G = -7.2$ mag, at the distance of the galaxy was

$$\mu_g = DM + \mu_G \tag{2.5}$$

With these amended normal distribution parameters, we performed a Monte Carlo simulation to determine the average number of GCs of the total, which would be above an apparent magnitude of 22 mag and therefore visible in the PanSTARRS imaging. The Monte Carlo simulation involved repetitively drawing a random sample from a Gaussian, with the parameters specified for each galaxy to determine GCs brighter than the required threshold, and thus potentially visible in our observational data.

For each host galaxy, the sample size was set to the total number of GCs, as calculated from rearranging Eq. (2.1), then 1000 simulations were performed and the average count of GCs visible at the required threshold was taken. The estimated count of GCs visible is illustrated in Fig. 2.3. The count of GCs is drawn on a log scale against the host galaxy

---

[3]Jordán et al. (2007, eq.18.)

distance and amounts to

$$N_{\text{GC,vis}} = N_{\text{GC,Total}} \int_{-\infty}^{+22} f(\mu_g, \sigma_g) \approx 1.9 \times 10^5 \qquad (2.6)$$

where $f(\mu_g, \sigma_g)$ is the Gaussian probability density function (PDF) of GCs within the host galaxy, as expressed previously. Overall, from the sample of host galaxies extracted within the selection criteria discussed, $\sim 5\%$ of the total GCs were within the 22 mag PanSTARRS threshold.

2.2 Time Domain Facilities

Time domain astronomy is the study of variations in the night sky over time. Variability in astronomical objects has been documented for many centuries. For example, soon after the invention of the telescope variability on the face of the Sun was noted through observations of sunspots by Thomas Harriot, David and Johann Fabricius', Christoph Scheiner and famously Galileo (Hoskin, 1999) from late 1610. Transient objects in the night sky have, however, been noted throughout history including comets traversing the heavens and even the occasional supernova such as the 1054 progenitor of the Crab Nebula (M1) documented throughout East Asia (Clark & Stephenson, 2013) and Tycho Brahe's *Nova Stella* in 1572, which the Danish astronomer studied for many months until it faded (Gingerich, 2005). It was a similar situation for Kepler's 1604 observations of a supernova (Clark & Stephenson, 2013). Significantly, both Tycho and Kepler's observations contributed further proof of the mutability of the extra-lunar sphere and thus sounded the death knell for Aristotelian cosmology and the Ptolemaic geocentric model, illustrating the importance of including the extra dimension in observational astronomy.

Despite this, it was not until the twentieth century that wide field of view (FOV) telescopes and improved photographic techniques afforded the opportunity to survey large portions of the night sky. Even so, these surveys were largely based on cataloging a static sky as the time period between repeat visits was still impractical for comparative observations. For instance, the first Palomar Observatory Sky Survey (POSS I) took nine years from 1949-1958 to complete (Minkowski & Abell, 1963) and a second survey (POSS II) was not carried out until the 1980's (Reid et al., 1991). Interestingly though, many historical photographic surveys have been, and continue to be, digitized to provide a comparative baseline (e.g. Pennington et al., 1993; Grindlay et al., 2009).

Table 2.2: PanSTARRS 3π Steradian Survey magnitude depths (adapted from Chambers et al., 2016, Table 11).

Filter	Nominal exposure (secs)	5σ single epoch (mag)	5σ stack limit (mag)
g_{P1}	43	22.0	23.3
r_{P1}	40	21.8	23.2
i_{P1}	45	21.5	23.1
z_{P1}	30	20.9	22.3
y_{P1}	30	19.7	21.4

Since the advent of large CCD chips in the mid-1990's, the possibility of repeated observation for transient and variability analysis has become more practical. One of the first such multi-epoch projects was the Optical Gravitational Lensing Experiment (OGLE) run by University of Warsaw and which commenced its first phase in 1992 (Udalski et al., 1992) with the 1.0m Swope Telescope at the Las Campanas Observatory in Chile. The success of the project allowed a move to a dedicated 1.3m telescope at

the same site in 1996 and it has been in its fourth phase since 2009, after technology upgrades implemented a mosaic of 32, 2048 × 4102 CCDs (Udalski et al., 2015). This project had (at the time) one of the largest Megapixel cameras in the world, with a 1.5° FOV but due to the nature of the microlensing experiment, observations were limited to the Galactic bulge, disc and latterly the LMC, SMC and Magellanic Bridge (Udalski et al., 2015). Nevertheless, the project has demonstrated the effectiveness of high cadence time domain astronomy through its discovery of many thousands of variable stars, as well as transiting exoplanets, supernova and Kuiper belt objects (KBOs).

Over the last decade, many facilities dedicated to observing portions of the night sky on a regular basis, have come online. The cadence which these facilities attempt to attain is largely dependent upon the nature (and funding) of the project being carried out, for which the technology and optical hardware will have been matched.

For example, clusters of small aperture telescopes with commercial lenses, deployed successfully in search of transiting exoplanets include projects such as the 7, 11cm telescopes of the Hungarian Automated Telescope Network (HATnet) with a pixel scale of $9''$ and its 6 southern hemisphere counterparts HATsouth using 4×18cm co-mounted lenses giving a pixel scale of $3.7''$ (Bakos, 2018). Similarly, the SuperWASP (Wide Angle Search for Planets) consists of an arrangement of 8×11cm co-mounted lens/cameras with a plate scale of ~$18''$ pixel^{-1} located in La Palma, Canaries and Sutherland, South Africa (Smith & WASP Consortium, 2014). Designed to search for supernova, the All-Sky Automated Survey for Supernovae (ASAS-SN), is a global network of 24 4×14cm telescopes surveying the whole sky every night (Shappee et al., 2014; Kochanek et al., 2017) searching for bright supernova down to g,V~18 mag with ~$8''$ pixel^{-1}. Pointing strategies result in varying coverage, for the above observatories - for example, HATnet allocate a primary field which is continuously observed throughout a night with 3 minutes cadence and to the end of 2018 (after 13 years of operation) the median pointing for a $10.6° \times 10.6°$ field was 6000 epochs.

While cost-effective, rapidly deployable and geographically scalable, these small telescopes provide wide-field images but are nonetheless limited in their photometric and astrometric capabilities having been designed largely to monitor variability in brighter stars. Although more expensive, larger conventional telescopes offer the ability to improve on photometric performance and search to greater depths of magnitude. A good example is the Panoramic Survey Telescope And Rapid Response System (PanSTARRS) based on a dedicated 1.8m telescope at the Haleakala Observatory in Maui, Hawaii. These optics, with a nominal 3.0° diameter FOV, are fitted with a 1.37 GigaPixel camera (Magnier et al., 2020) giving a pixel scale of ~$0.26''$ pixel^{-1}.

In the initial phase of this observatory, from 2010-2014, the majority of the time (56%) was allocated to repeat observation of the sky visible from Hawaii in the 3π Steradian Survey - i.e. 30,000 deg^2 north of Dec $-30°$. By the end of this phase each portion of the sky had been visited between 10-20 times in 5 filters ($g_{P1}, r_{P1}, i_{P1}, z_{P1}, y_{P1}$). The larger optics and higher resolution camera give the 5σ single epoch and stacked image magnitude limits in each of the $grizy_{P1}$ filters as shown in Table 2.2 (Chambers et al., 2016). While the PanSTARRS project provides access to good quality repeat imaging over a four year period, the cadence of 2-3 months per target visit, is marginal for the extraction of the expected transient signals detailed in §1.4.

Improving the cadence of wide-field observations, to facilitate detection of a range of both short-term transients and long-term variability, was one of the prime objectives of the Palomar Transient Factory (PTF) (Kulkarni, 2012). The PTF was active from

2009 to 2012 (Law et al., 2009), with its successor the intermediate-PTF (iPTF) (Masci et al., 2017) running until its replacement by the Zwicky Transient Facility (ZTF) in 2018 (Bellm et al., 2019a; Graham et al., 2019).

As outlined by Kulkarni (2013), the primary difference between the PTF and iPTF was the introduction of an automated photometric pipeline, producing calibrated images and other standard photometric products in association with the Infrared Processing and Analysis Centre (IPAC). In addition to this, the PTF collaborators used the IPAC created products (e.g. co-added reference images) in a real-time transient pipeline, able to process and deliver transient candidates within 30 minutes of observation. All three of these systems were based on the Palomar 48 inch (1.2m) Samuel Oschin Schmidt (which had been used for the POSS I / II survey's mentioned

Figure 2.4: Timelapse of the Samuel Oschin telescope dome at Mt. Palomar, CA., housing the 48″ Schmidt telescope which served as the optical platform for POSS I/II, PTF, iPTF and ZTF (Credit: Palomar/Caltech).

above - see Fig. 2.4). The PTF and iPTF were successful in their objectives to aid in the discovery and classification of transients (see Bellm (2019) for a summary), but were limited in their ability to cover the full sky due to a sensor FOV of 7.26 deg^2. A major upgrade to the ZTF was installation of an array of 16, 6k×6k CCDs, to cover a full 47 deg^2 FOV of the telescope (Dekany et al., 2020). A higher speed of CCD readout (46 seconds for PTF to 10 seconds for ZTF) with faster telescope and dome drives further increased the survey speed potential, while maintaining the image quality (2.2″ FWHM). Weather permitting the ZTF achieves a ∼3-day cadence on coverage of the entire northern hemisphere in ZTF-g and ZTF-r filters. The ZTF is also being used to develop tools and techniques for the Vera C. Rubin Observatory (previously the Large Synoptic Survey Telescope, or LSST).

While the above introduction covers a selection of optical based systems, there are all-sky surveys, both terrestrial and satellite-based, which have been carried out in other wavelengths, with some providing time-domain photometry in addition to stacked 'static-sky' reference imaging. For example,

- Gamma ray observatories include the Swift Gamma Ray burst (GRB) mission and Fermi Telescope. The Swift mission (Gehrels et al., 2004), launched in 2004 and still operating, contains a γ-ray Burst Alert Telescope (BAT) sensitive from 15-150 keV with a source position determination resolution of 1′-4′ (Nousek et al., 2011; Gehrels & Cannizzo, 2015). The BAT is used to alert ground-based networks and redirect the satellite to align the on-board X-ray (XRT) and UV/Optical (UVOT) telescopes for fast ($\sim$ 90) multi-wavelength temporal evolution follow up of the GRB afterglow. The Fermi Large Area Telescope (Fermi-LAT, Atwood et al., 2009), an imaging γ-ray telescope, covering a 20 MeV to >300 GeV energy range, and designed to detect transients and allow monitoring of variable sources,

- X-rays telescopes include Röentgensatellit or ROSAT, which operated throughout

the 1990s and carried out the first complete X-ray survey of the sky, the ROSAT All-Sky Survey (RASS), with its high-resolution X-ray imager, sensitive in the 0.1-2 keV band (Voges et al., 1999). The more recent extended Röentgen Survey with an Imaging Telescope Array or eROSITA (Predehl, 2017), is 30 times more sensitive than ROSAT in the soft X-ray band (0.5-2 keV) and has performed the first true imaging survey of the sky in the hard band (2-8 keV). eRosita plans to repeat its all-sky survey every six months throughout its initial 4 year mission profile, and its probability of detecting emissions from IMBH TDEs, has been analysed by Malyali et al. (2019). As mentioned above, the Swift mission also contains an XRT designed to perform a hard (0.2-10 keV) X-ray all-sky survey (Gehrels et al., 2004), but which has also been used to monitor the X-ray time evolution of GRB sources.

- UV observations have been carried out by a number of missions, including the Galaxy Evolution Explorer (GALEX) launched in 2003, and which carried out the first space based UV all-sky survey (Martin et al., 2005) at 135–275 nm. As mentioned above, the Swift mission also contains a UVOT with a 17 " × 17 " FOV, sensitive in 6 colours from 170–600 nm (Gehrels et al., 2004).

- The infrared band has been sadly neglected from a time-domain perspective, although there have been many surveys in multiple IR photometric wavelengths, to provide a picture of the infrared sky. Space based missions include the Japanese Akari satellite which surveyed the sky in six passbands from the mid to far infrared, 2–180 µm (Murakami et al., 2007), and the Wide field Infrared Survey Explorer (WISE) surveying in 3.4, 4.6, 12 and 22 µm (Wright et al., 2010). A southern hemisphere survey focused on IR variability was carried out by the Visible and Infrared Survey Telescope for Astronomy (VISTA) based at the Paranal Observatory, Chile (Emerson et al., 2006). However, other IR terrestrial surveys, such as the 2-micron All-Sky Survey (2MASS, Skrutskie et al., 2006) and the northern hemisphere UK Infrared Deep Sky Survey (UKIDSS) (Lawrence et al., 2007) had limited repeat observations.

- In the radio spectrum, one of the objectives of the Low-Frequency Array (LOFAR) (van Haarlem et al., 2013) is to detect transients such as Fast Radio Bursts (FRB) in addition to a survey known as the LOFAR Tied-Array All-Sky Survey (LOTAAS). In the future, The Square Kilometer Array (SKA) with sites based in Australia and South Africa, will improve on the resolution and sensitivity of LOFAR, while also increasing survey speeds (Dewdney et al., 2009).

The success of many of the above facilities and the discovery of new phenomena in niches of the temporal dimension, has encouraged funding for wider, faster and deeper survey instruments in many different areas of the electromagnetic spectrum. These include individual facilities such as the Nancy Grace Roman Space Telescope / Wide-Field IR Space Telescope (WFIRST, Akeson et al., 2019), the Large Area Survey Telescope (LAST, Ofek & Ben-Ami, 2020), and the Vera C. Rubin observatory / Legacy Survey of Space and Time (LSST, Ivezić et al., 2019). A comparison of the 'Grasp', or the volume surveyable per unit time as outlined by Ofek & Ben-Ami (2020), is shown in Fig. 2.5. Additionally, there are now initiatives, such as the Deeper, Wider, Faster (DWF) programme (Andreoni & Cooke, 2019; Strausbaugh et al., 2021), involving multi-wavelength instruments all over the globe, set up specifically for fast response to detected transients, affording observation in multiple passbands only seconds after a rising burst is detected.

In summary, technology in recent years, has improved the sensitivity, resolution and speed of observations through which a number of new phenomena have been discovered and continue to be studied. These include variability and transients in the sky from milliseconds, e.g. pulsars, FRB, through to many decades, e.g. orbital motions, expanding SN envelopes. Although still rare, this includes the transient TDEs, which we are now able to detect and study in more detail than ever before. Future surveys which increase the depth and hence volume of the sky observed on a regular basis, will only add to the ever increasing list of TDEs and other time domain phenomena which make the sky so dynamic.
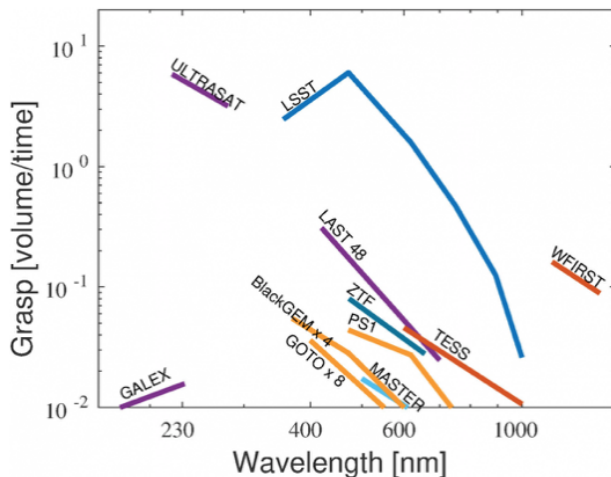
Figure 2.5: Observed volume per unit time for past, present and future time domain facilities (Credit: Ofek & Ben-Ami, 2020).

2.2.1 Longlist and Selection Criteria

As discussed above (§2.2), there are many observatories around the globe which have executed multi-epoch wide-area surveys, from which datasets could be analysed for evidence of tidal disruption events. An initial high-level search of potential optical transient and survey facilities is summarised in Table 2.3.

While the consolidation and analysis of multiple datasets may have provided many benefits (see Chapter 7), it was deemed by the author to be unnecessary during this initial project. Combination of data from multiple archives with differing properties, would also have made definition of a uniform selection function complex, if not impossible. Therefore, to allow more robust limits to be placed on the volume surveyed through an identified period, the single best archive was to be selected, for which a series of criterion pertaining to the detection of TDEs was drawn up. These criteria are discussed below and summarised in Table 2.4.

The expectation is that the profile of a TDE will rise over several weeks, and may last for many months. The observation cadence therefore needs to be sufficient to distinguish candidate transients from other astrophysical events, primarily supernova, but also other intermittent events such as those associated with cataclysmic variables.

For terrestrial based facilities, the notional cadence is also affected by lunation, the local weather and seeing, although this is less of a factor for prime observatory sites such as those located in Hawaii and Chile, and obviously satellite based missions, such as Gaia. However, facilities offering a cadence which is marginal for the time period expected (i.e $t_{rise} \gtrsim 4$ weeks), would have a higher probability of being affected by atmospheric conditions. At best, this could lead to a reduction in limiting magnitude, giving unacceptably high signal-noise ratios, or at worst a complete lack of observation for the epoch in question. In order to alleviate this, a facility with a cadence increment better than double the minimum requirement ($\lesssim 2$ weeks) would ideally be selected.

Table 2.3: Longlist comparison between optical survey/transient facilities showing telescope/camera combination field-of-view and sky area coverage, nominal limiting magnitude assuming seeing $\sim 1.5''$, sensor resolution on the sky, nominal cadence and period of operation. See text for a detailed assessment.

Facility Name	FOV / Coverage $(\deg^2)$	Depth 5σ (mag)	Plate Scale (arcsec)	Cadence (days)	Period (years)	Data Access	References
Pan STARRS	7 / 30,000	g$\sim$22.0 r$\sim$21.8 i$\sim$21.5 z$\sim$20.9 y$\sim$19.7	$\sim$0.25	90	2010 - 2014	MAST[4]	Chambers et al. (2016)
Asteroid Terrestrial impact Last Alert System (ATLAS)	29 / 35,000	g$\sim$19.5	$\sim$1.86	$\sim$2	2016 to date	ATLAS[5]	Tonry et al. (2018)
Catalina Real-time Survey	19.4 / 33,000	V$\sim$19 - $\sim$21.5	$\sim$1.5	>7	2005 to date	CSDR[6]	Drake et al. (2009) Djorgovski et al. (2011)
SDSS	6 / 14,555	u$\sim$22.1 g$\sim$22.6 r$\sim$22.3 i$\sim$21.9 z$\sim$20.3	$\sim$0.4	4	2000 - 2008	SDSS[7] (Phase 2)	York et al. (2000) Frieman et al. (2008)
Dark Energy Survey (DES)	3 / 5,000	g$\sim$23.0 r$\sim$22.8 i$\sim$22.0 z$\sim$21.4 Y$\sim$20.2	$\sim$0.27	$\sim$7 (SN)	2013 - 2019	DES[8] access	DES Collab. (2005) DES Collab. et al. (2016)
PTF/iPTF	7.8 / 8,000	g$\sim$21.3 R$\sim$20.6	$\sim$1	5	2009 - 2017	IRSA[9]	Law et al. (2009) Masci et al. (2017)
Gaia	2$\times$0.5 / 41,253	G$\sim$20.7	$\sim$0.1	$\sim$30	2014 - 2016	MAST[4]/ (DR2)	Gaia Collab. et al. (2016)
ASAS-SN	4.5 / 41,253	V$\sim$17	$\sim$8	2-3	2013 to date	OSU[10]	Kochanek et al. (2017)
ZTF	47 / 23,675	g$\sim$20.8 r$\sim$20.6 i$\sim$19.9	$\sim$1	1-3	2018 to date	IRSA[9]	Bellm et al. (2019a)

The passband(s) in which to carry out the analysis was also a prime consideration. As discussed in §1.4, a TDE based around an IMBH in a CSS or GC involving a sub-solar mass WD, would be observable in a number of passbands. For a face-on thin disc, the highest luminosity is likely to be in X-ray. However, where opacity is increased,

---

[4]MAST - Mikulski Archive for Space Telescopes
[5]ATLAS - Falling Star, forced photometry
[6]CSDR - Catalina Survey Data Release
[7]Sky Server - All SDSS survey data
[8]DESaccess - Public DES data
[9]IRSA - NASA/IPAC Infrared Science Archive
[10]Sky Patrol - ASAS-SN, hosted at Ohio State University

radiation reprocessing to longer wavelengths is more probable. For a thick disc then, UV and optical bands may dominate. If the TDE accretion rate is sufficient for a jet to form, then the event may also be visible at radio wavelengths, with the caveat this would require a largely face-on aspect to ensure detection. In summary, while thick-disc scenarios are more likely to be detectable at optical wavelengths, due to disruption encounter variability, it is unclear whether thin or thick disc formation has any sort of bias.

In any case, selection of an observation band or bands has to be offset against the cadence of available observations which, as discussed above, covers a wide range for different facilities based on their primary function. In addition to this, the positions of known objects in the CSS catalogue (see §2.1) had largely been determined, or verified, through optical photometry. For example, the archive of intermediate mass stellar systems (AIMSS) survey (Norris et al., 2014) used broad-band optical images from the HST archives taken by the WFPC2, ACS and WFC3, with spectroscopic follow-up carried out on a number of telescopes, predominantly at optical wavelengths. As a result, the majority of the catalogue CSS observations have supplementary optical band data, and for this reason, the author's preference was to continue to work with data from the optical domain. It should also be noted that there appears to be a bias towards optical based facilities in comparison to other bands, as they appear on the surface to be far more prolific. This is no doubt due in no small part to the dominance of sight as a human sense, and consequently due to the development of optical technology ahead of other wavelengths of EM radiation.

Table 2.4: Criteria for selection of time domain facility observation data.

Criterion	Value	Comments
Cadence	<2 weeks per single epoch visit	To improve probability of obtaining observations during transient rise.
Band	Optical. Multiple filters (min. 2)	Minimum of 2 filters per epoch to facilitate determination of object colour.
Data Accessibility	Online access. Mature API[11]. Max. 6 month latency	Ease of access programmatically is key, as is access to up to date data. Latency could be due to data release schedule or proprietary project data.
Limiting Magnitude	Better than ~ 21 g/r mag	See §1.4. This limit should allow detection of many optical TDEs.

As this project was to be based on existing archives, and no new observations were anticipated in the initial phase, the availability and accessibility of online data was also a prime consideration. Many of the facilities mentioned above are funded by specific agencies and project data may remain proprietary for a certain period of time before being released into the public domain. Common examples include archives based on the Sloan Digital Sky Survey (SDSS, York et al., 2000), the Hubble Legacy Archive (HLA). Typically, observatory data is specific to individual projects (which have funded the telescope time) and remains proprietary for a minimum of a year before being publicly released. On the other hand, survey data is sometimes available immediately, especially in the case of alert data which requires immediate follow-up by astronomers in multiple

---

[11]Application Programming Interface

passbands after a transient source has been detected, e.g. Swift, ATLAS, CRTS and ASAS-SN. As a side note, another consideration with survey data has less to do with its proprietary nature, but more to do with the pipeline processing (i.e. reduction) and management of an archive, which requires a huge investment in infrastructure and which, to a large extent, is as complex from an information technology perspective, as the initial observations are from an astronomical point of view. With this in mind, many facilities have opted to carry out periodic data releases (e.g. SDSS, Gaia). In these cases, reduced data, which may take many months to produce, is often still subject to an embargo for authorised agency scientists prior to an ultimate release into the public domain.

Having identified the criteria required from a time domain facility, a desktop exercise was carried out to review the longlist of facilities (Table 2.3) to determine a shortlist for detailed assessment.

PanSTARRS : Good depth and resolution with optical band coverage through five filters ($grizy_{P1}$). Sky coverage (3π steradian survey) consisted of 60 epochs in the five passbands of the entire sky north of declination $\delta = -30°$ (Chambers et al., 2016) giving an average cadence of 90 days. This survey data originates from 2009-2014. Data accessibility is good through MAST API with AstroQuery support for direct access to light curve data.
Conclusion: Shortlist (review available data)

ATLAS : Acceptable resolution, although depth is marginal for transients at $m \sim 19.5$. Cadence and coverage is excellent, with practically full sky coverage (from three sites in Hawaii, Chile and South Africa) every 2 days (Tonry et al., 2018). At the time of the initial review for this project, events only were reported to the Transient Name Server (TNS) and an API for full data access did not exist. However, this has since been implemented and would be useful for follow-up (Smith et al., 2020).
Conclusion: Reject, but use for additional validation

CRTS : Acceptable resolution with depth good from one of the three telescopes used. 33,000 sq.deg. of coverage over seven years of imaging (up to DR2) with some data back to 2005, with and average cadence of $\sim$7 days (Drake et al., 2009). No API at present, planned for DR3 along with image access. Position file upload possible to obtain multiple source LC.
Conclusion: Reject due to variable depth in coverage area and lack of API

SDSS : Good depth and resolution in five optical passbands ($ugriz_{SDSS}$). Projects have provided access to multiple survey data products involving varying coverage and cadence, e.g. SDSS-I (Legacy) covered 7,500 square degrees of the North Galactic Cap (Ivezić et al., 2007) but with minimal repeat visits, while SDSS-II(SN) performed multi-epoch observation from from Sept to Nov of 2005–7 but only covered 300 sq.deg. in the southern hemisphere (Frieman et al., 2008). To date, 14,555 sq.deg. of sky have been surveyed, but with variable cadence. Access to data is good through a bespoke website and API with AstroQuery support, but light curves for objects throughout the full sky are not accessible.
Conclusion: Reject - minimal multi-epoch observations

Dark Energy Survey : Excellent depth and resolution in the five optical passbands ($grizY_{DES}$). However, as with many non-transient specific surveys, coverage is lim-

ited, to $\sim \frac{1}{8}$ of the southern hemisphere. Multi-epoch imaging, applicable only to SN survey, consisting of a 27 sq.deg. field visited weekly throughout the six month DES season between 2013-2019 (DES Collab. et al., 2016). Access to limited data is available through online query tools.

Conclusion: Reject - limited sky-coverage, minimal multi-epoch, limited data access

PTF/iPTF : Acceptable resolution in two filters (SDSS-g' & Mould-R) with a good cadence over its period of operation (2009-2016). However, full sky (northern hemisphere) coverage was not continuous and data accessibility might be limited due to project embargo (Law et al., 2009; Masci et al., 2017). Available data accessible through IRSA API and AstroQuery.

Conclusion: Shortlist (review available data)

Gaia : Excellent resolution with good depth through effective G band magnitude and red/blue photometry for colour. Full sky coverage unaffected by vagaries of terrestrial seeing, although cadence of repeat visits is ∼30 days on average (Gaia Collab. et al., 2018). Access to full data is good through a number of mirror sites and MAST with AstroQuery API. Data release schedule is infrequent, i.e. >2years due to complex data reduction required.

Conclusion: Reject due to release schedule / cadence

ASAS-SN : The poorest depth and resolution of the considered facilities, but this is a compromise as the cadence for full-sky imaging is 2-3 days (aspirational daily) (Kochanek et al., 2017). Nevertheless, the depth of the imaging is designed to detect brighter SN, so would be unlikely to be useful for TDEs.

Conclusion: Reject due to minimal depth

ZTF : Acceptable depth and resolution, with good cadence for coverage of full northern hemisphere in three filters, although it was noted that coverage taken in g & r filters is significantly better than in i passband. Alert data is available immediately and DR schedule is for release of public data after 3 month proprietary period, which was reduced to 2 months during the course of the project (Bellm et al., 2019a). Data access through MAST and AstroQuery API is good, with light-curves directly available for download and analysis.

Conclusion: Shortlist

Clearly, all facilities listed above have advantages and disadvantages, based largely on the primary function for which they had originally been designed. e.g. the astrometric performance of Gaia is exquisite, but its temporal capabilities are used for determination of proper motion, and variability appears limited to a known catalogue of variable sources. At the other end of the scale, ATLAS, CRTS and ASAS-SN are more cost effective solutions designed for Near-Earth Object (NEO) and bright SN detection, with follow up expected on larger telescopes to determine the nature of the source/object.

Based on the above rudimentary assessment of an initial longlist of optical facilities which provide photometry data from multi-epoch imaging, the author selected the ZTF facility as the best compromise of the necessary requirements. The PanSTARRS and PTF facilities were accepted for review of available data, primarily for comparative purposes, as the former has imaging available in wider selection of filters, and it was considered that

the latter, being based on the same optics as the ZTF, may provide a simple temporal extension of the photometry for objects

2.2.2   Shortlist Assessment

The assessment of the three facilities shortlisted, was carried out to provide an initial introduction to the data products available and also to provide experience in the use of various Python based data query and manipulation packages, including AstroPy, AstroQuery (Ginsburg et al., 2019), NumPy and Pandas. At the same time, use of the Matplotlib package (Hunter, 2007) was investigated for standardisation of output and presentation of light curve information for sources. Additionally, experience in the use of MAST and IRSA based APIs was also gained.

Test Objects

Throughout this assessment, and while setting up code to interface to the facility data archives, test objects of various types were setup for repeated review and comparison. The objects were not necessarily related to CSS, but were selected for their variety of type, and where applicable, general variability in luminosity to demonstrate the capabilities of the facilities being assessed. These objects are shown in Table 2.5 and were selected in order to be able to prove the candidate selection algorithm on known positive and negative objects, to allow tuning of the process to reject false positives and accept false negatives.

The test objects fall into two groups. The first group were a selection of well documented objects from the CSS catalogue, i.e., NGC4546-UCD1 (Norris & Kannappan, 2011), M60-UCD1 (Norris et al., 2014), M85-HCC1 (Sandoval et al., 2015) and M59-UCD3 (Sandoval et al., 2015). These were selected as they are objects which are typical UCDs, albeit more luminous than for more distant objects to ensure a higher S/N ratio for photometry during initial setup. Due to their relative proximity, size and luminosity, these objects have been studied extensively in the past and so there was little expectation that these objects would present evidence of TDE flaring. Nevertheless, the purpose here was, from a process perspective, to provide an initial view on sample count and cadence, and from a code perspective to allow for setup of a standard output, presenting the light-curves samples of magnitude against time, with a median value and 3σ uncertainty. As the filter coverage for a random selection of objects is indeterminate, validation and presentation of available data was also required.

The second group of test objects were selected because of their diverse variability, specifically, intrinsic, extrinsic, periodic or stochastic, and were chosen to allow further analysis of the sample distribution. These objects included an eclipsing binary (V* IP Lyr), a pulsating variable (V* BG Gem), a quasar (WISE J005448.54+225123.5), a flare star (Kepler KIC #6691930), an X-ray source associated with a candidate IMBH (3XMM J215022.4-055108, Lin et al., 2018), a type 1a candidate supernova (TNS SN2021ldj Munoz-Arancibia et al., 2021) and two TDEs (AT2019qiz and AT2021jsg, Siebert et al., 2019; Yao et al., 2021, respectively). The potential for these objects to cause false-positives, insomuch as they might be confused as TDEs, was examined and subsequently used to tune the approach and parameters adopted in the analysis.

Table 2.5: Test objects used throughout the assessment phase of the facilities

Name	RA	DEC	mag (g')	Comments
NGC4546-UCD1	188.8696	-3.7892	18.06	Rh=25.54
M60-UCD1	190.8999	11.5346	17.4	Virgo cluster, Rh=24.2pc, d=16.5Mpc
M85-HCC1	186.3452	18.1816	18.95	Virgo cluster - Densest known UCD - Rh=1.85pc, d=18.5Mpc
M59-UCD3	190.5460	11.6448	16.94	Virgo cluster - 2nd densest known UCD - Rh=20pc, d=15.3Mpc
V* IP Lyr	275.8516	33.1855		Eclipsing binary
V* BG Gem	90.8783	27.6974		Pulsating variable (RV Tauri)
WISE J005448.54+225123	13.7022	22.8568	17.7584	Quasar
KIC #6691930	291.9606	42.1718		Kepler flare star
3XMM J215022.4-055108	327.59333	-5.8525		X-ray source IMBH candidate
SN1a Candidate	270.1704	37.2755		TNS SN2021ldj Redshift=0.073
TDE #1	167.1529	30.7613		TNS AT2021jsg Redshift=0.126
TDE #2	71.6579	-10.2265		TNS AT2019qiz d=66Mpc

Table 2.6: Observation data for WISE J005448.54+225123 quasar, showing a summary of samples available from PanSTARRS, PTF and ZTF optical time domain observatories.

	PanSTARRS					PTF		ZTF		
	g	r	i	z	y	g	R	g	r	i
Samples	12	20	22	16	13	-	53	287	346	40
Min. interval (min)	16	16	16	7	9	-	53	2	-	5
Mean interval (days)	107	77	73	105	120	-	30	4	4	12
Max. interval (days)	756	448	390	557	360	-	1434	138	130	237
Interval SD	226	142	133	142	118	-	197	13	10	37
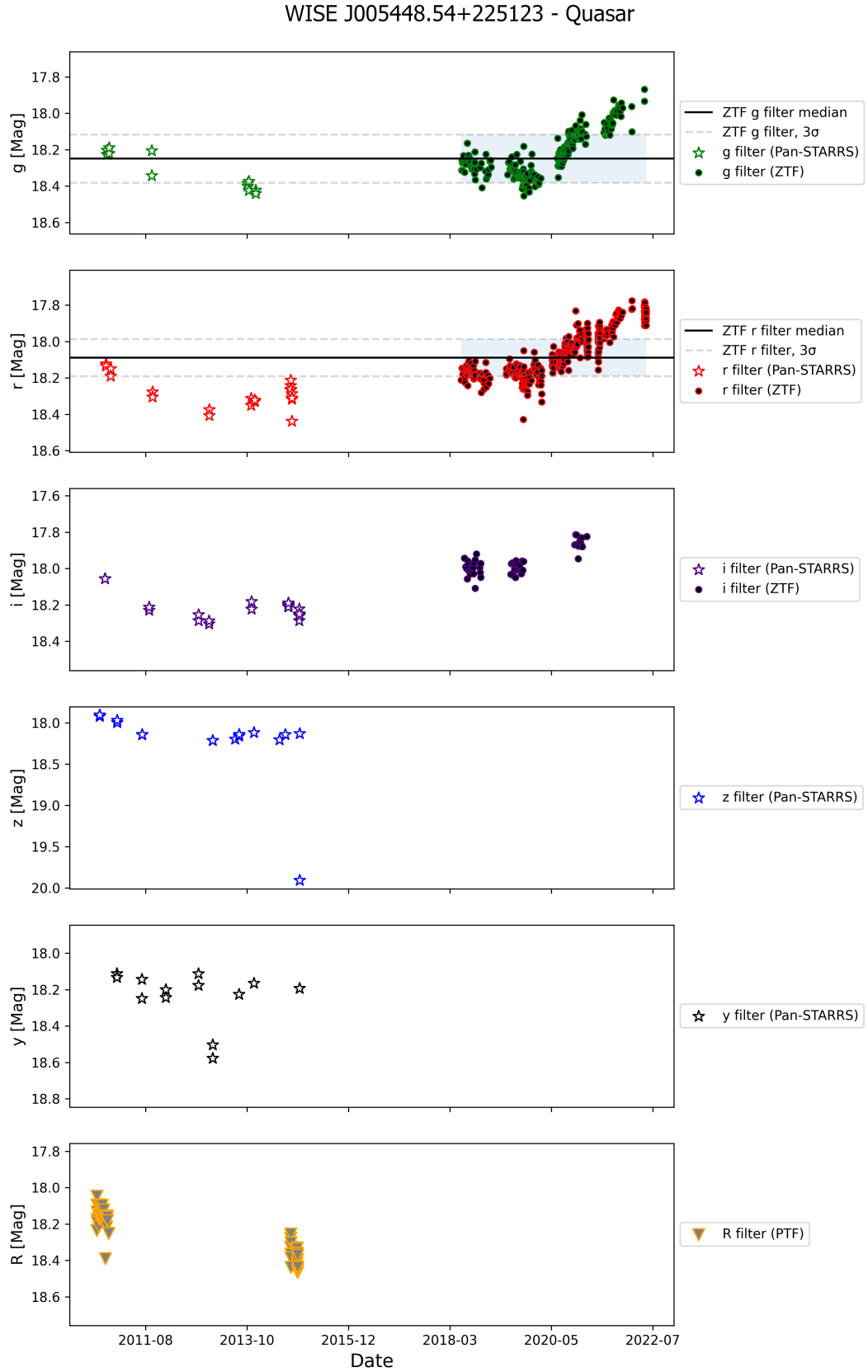
Figure 2.6: Example of light curves available from three optical time domain facilities including the Panoramic Survey Telescope and Rapid Response System (PanSTARRS-*grizy* to 2015), the Palomar Transient Factory (PTF-*R* to 2016) and the Zwicky Transient Facility (ZTF-*gri* from 2018 on). From top to bottom, light curves show magnitude in g, r, i, z, y & R filters respectively. g and r light curves show Median and 3σ for ZTF observations. Error bars excluded for clarity.

Data available for each of the test objects mentioned above (Table 2.5) was downloaded, allowing the relative performance and attributes of each of the facilities to be compared. This was carried out visually by plotting the light curves, and quantitatively, by summarising aspects such as the mean, maximum and standard deviation on the observation intervals.

The light curves in Fig. 2.6 and the summary data shown in Table 2.6, are based on observations of the WISE[12] J005448.54+225123 quasar, and show an example of the data retrieved from three optical time domain facilities including the Panoramic Survey Telescope and Rapid Response System (PanSTARRS), the Palomar Transient Factory (PTF) and the Zwicky Transient Facility (ZTF). For the WISE quasar object shown, the variation in the luminosity of the source is evident. However, more importantly at this stage, a comparison of the data available from the three facilities clearly show significant differences resulting from scheduling, coverage, observation performance and to a certain extent seeing considerations at the respective sites. These differences manifest not only in incomparable cadence for individual objects, but also what appears to be a variable duty-cycle to different sectors of the sky. This is particularly apparent for PTF in the R band, where despite 53 imaging epochs in total, the interval between high cadence sampling of this target is nearly $\sim$4 years (1434 days) and there is a complete void of records in the g band. In fairness to PTF however, this was atypical and other targets had higher observation totals / cadence.

The PanSTARRS data shows a more even distribution. For example in the i band, the maximum interval of repeat visits to the target is just over 1 year (390 days) but the mean interval is still 73 days, despite several same-night, repeat samples. Although the total samples recorded for this target by PanSTARRS is higher at 83 across the five $grizy$ filters, this amounts to an average of only 17 samples per band, with the maximum (22) being attributed to the i filter. The total ZTF samples for this object are significantly higher, with 287, 346 and 40 observations being carried out through the g, r & i filters respectively over a comparative 4 years of operation. The maximum sample gap in the r band is 130 days, but the sample interval mean is $\sim$4 days. The annual gaps evident in the ZTF coverage which correlate between the three ZTF filters, are presumed to be seasonal gaps, i.e. when the target is low on the horizon and the observation air mass is deemed too great. The priority given to observing in the g & r filters, in deference to the i band, is also evident.

In the comparative analysis of the three facilities, the author notes that the filters used are subtly different to the original Sloan (SDSS) filters on which they are modelled, but for the purposes of this analysis no distinction is required, or has been made.

In the end it was decided that the ZTF would provide the best all round performance for observation of the majority of the northern hemisphere i.e. $\delta > -30$ with a cadence of $\sim$3 days in at least 2 optical filters (g & r). It was also appealing that the ZTF facility was still active during the period of this project and hence data samples were increasing. While the resolution of the ZTF (pixel scale $\sim$1″, FWHM $\gtrsim$2″) was not as good as other facilities, for example PanSTARRS has 4× better resolution (pixel scale $\sim$0.25″, FWHM $\gtrsim$0.″6), this was deemed acceptable.

---

[12]Wide-field Infrared Survey Explorer (Wright et al., 2010)

2.3   Zwicky Transient Facility

As mentioned earlier (§2.2) the Zwicky Transient Facility (ZTF) is based around the Palomar 48" Schmidt telescope or P48, now known as the Samuel Oschin telescope, which was used in some of the earliest sky surveys. The facility is based on Mount Palomar in California, USA, where there are several other telescopes located, including the Palomar 60" or P60, used by the ZTF facility for spectroscopic follow up of targets (Blagorodnova et al., 2018), and the Hale 200" reflector, which was the largest telescope in the world from 1949 to 1976 (Maddison, 1997).

Table 2.7: Specification of the Zwicky Transient Facility showing key performance parameters for the Telescope optics, Camera and CCD sensor array. (Reproduced from Bellm et al. (2019a))

Telescope and Camera	
Telescope	Palomar 48 inch (1.2 m) Samuel Oschin Schmidt
Location	$33°21'26\rlap{.}''35$ N, $116°51'32\rlap{.}''04$ W, 1700 m
Camera field dimensions	$7\rlap{.}°50$ N-S $\times$ $7\rlap{.}°32$ E-W
Camera field of view	55.0 deg^2
Light-sensitive area	47.7 deg^2
Fill factor	86.7%
Filters	ZTF-g, ZTF-r, ZTF-i
Filter exchange time	~110 s, including slew to stow
Image quality	g = $2\rlap{.}''1$, r = $2\rlap{.}''0$, i = $2\rlap{.}''1$ FWHM
Median Sensitivity (30 s, 5σ)	$m_g = 20.8$, $m_r = 20.6$, $m_i = 19.9$
	$m_g = 21.1$, $m_r = 20.9$, $m_i = 20.2$ (new moon)
CCD Array	
Science CCDs	16 6144 $\times$ 6160 pixel e2v CCD231-C6
Guide and Focus CCDs	4 $2k \times 2k$ STA; delta doped by JPL
Pixels	15 µm pixel^{-1}
Plate scale	$1\rlap{.}''01$ pixel^{-1}
Chip gaps	$0\rlap{.}°205$ N-S, $0\rlap{.}°140$ E-W
CCD readout channels	4
Readout time	8.2 s
Read noise	10.3 e- (median)
Gain	5.8 e-/ADU
Linearity	1.02% $\pm$ 0.09% (correction factor variation)
Saturation	350,000 e-

Schmidt telescopes are designed to provide a wide field of view through the use of a corrector lens at the main aperture of the optics. Even with a corrector lens, the prime focus of the P48 is not planar and the original photographic survey's needed to form the plates in a jig prior to exposure. Although the P48 has a 48" aperture, the primary mirror is 72" and the 16, 6k×6k CCD array is fitted at the prime focus. As detailed in Dekany et al. (2020), major modifications of the optical train for use by ZTF were required and included fitment of a cryostat assembly on which the CCD array is mounted, and individual field flattener cryostat windows. Due to the use of a planar CCD array, an aspheric trim plate, in addition to the existing corrector plate, was also required to maintain image quality by meeting the Nyquist pixel sampling for $2''$ FWHM specification and maximizing the field of view.

The three g, r and i spectral filters of the ZTF are individual, full-frame filters exchangeable throughout an observing session Dekany et al. (2020). This process is nec-

essary up to 20 times a night, due to scheduling and allocation of project time on the telescope (Bellm et al., 2019b), so for performance reasons, filter exchange is carried out by a robotic arm mounted inside the optical tube, and takes about 2 minutes to exchange. This includes time for the telescope to slew to a safe position.

A summary of this, and other key data specifications for the ZTF, including the telescope, camera and CCD sensor array are shown in Table 2.7.

ZTF observing time is allocated on the basis of funding proportion (Bellm et al., 2019b). The data for this project was taken predominantly from the first phase of the ZTF programme (ZTF-1), lasting 30 months from commissioning in Mar 2018 to Sep 2020, funding was provided by the NSF (40%), a ZTF collaboration partnership (40%) and the remaining 20% by Caltech. As a consequence of this funding arrangement, 40% of the telescope time was allocated to 3-day, northern sky (85%) and 1-day, galactic plane (15%) public surveys in g & r filters. Another 40% using all three g, r, & i filters, was allotted to ZTF Collaboration specified surveys, consisting primarily of targets benefiting from higher cadence observations. The remaining 20% of time was allocated to individual Caltech projects. The public survey data is accessible through rolling data releases which commenced from 2019, and the ZTF Collaboration and Caltech data is made available after an 18 month proprietary period.

After download from the camera, the raw image data is sent in real-time from Palomar via a microwave link to the San Diego Supercomputer Centre (SDSC) before transfer over the internet to IPAC where further processing and generation of data products occurs.

2.3.1 Data Processing and Products

Once the image data has been ingested into IPAC, it is used in 3 separate pipelines as detailed in Masci et al. (2019) and summarised here.

Firstly, an image reduction pipeline carries out a standard calibration using instrumental flats and biases before a source extraction algorithm is carried out on the image, so photometry and magnitudes can be measured at the positions of identified sources. This provides what ZTF refer to as a single epoch catalogue, which is ultimately consolidated into the light curve archive data.

The second pipeline uses the same image data to feed the real-time alert data through difference imaging. Over time, ZTF have built up reference images for each pointing grid on the sky by stacking a minimum of 20 'good' (i.e. high S/N, good seeing) single epoch images, for which typically 60 images are required. Difference images are created by subtracting single epoch images from the reference and another source extraction is then performed to identify statistically significant variations, i.e. 5σ detections. These are considered to be transient candidates which are filtered, e.g. for instrumental artefacts, and vetted through a real/bogus machine learning (ML) algorithm (Duev et al., 2019; Mahabal et al., 2019). Nevertheless, with around ~500/~1000 pointings per night in the summer/winter seasons, this gives an alert rate of $\sim 10^3 - \sim 10^5$ transients per night.

The final pipeline is designed to alert for moving objects by looking for streaks in the image data. Further processing is carried out to determine if the movement comes from a natural or artificial object. Natural objects are reported to the Minor Planet Centre (MPC) to improve orbits of known objects or identify new objects. The alert rate of

---

[13]ZTF alert packets are distributed using Apache Avro™, a data serialisation framework from the Apache Software Foundation https://avro.apache.org

Table 2.8: ZTF Data Products - subset of data extracted from Masci et al. (2019)

Product ID	Description	Format	Generation Frequency	Public	Access
1	Raw images	fpack'd MEF	Real time	Yes	Archive: GUI or API
2	Epochal science images	FITS	Real time	Yes	Archive: GUI or API
3	Epochal source catalogs	FITS binary tables	Real time	Yes	Archive: GUI or API
4	Point-spread functions	FITS, ASCII	Real time	Yes	Archive: GUI or API
5	Epochal-difference image files	fpack'd FITS	Real time	Yes	Archive: GUI or API
6	Reference image (co-add) files	FITS	Real time (static)	Yes	Archive: GUI or API
7	Reference image source catalogs	FITS binary tables	Real time (static)	Yes	Archive: GUI or API
8	Calibration image files	FITS	Daily	Yes	Archive: GUI or API
9	Point-source alert packets	Avro[13]	Real time	Yes	
10	Light curves and metrics	Various	Updated monthly	Yes	Custom GUI or API
11	Source matchfiles	Pytable (HDF5)	Updated monthly	No	Datastore for #10
12	Streak data (fast-moving SSOs)	ASCII, JPEG, ADES	Real time	No	MPC
13	Moving-object tracks	ASCII, JPEG, ADES	Daily	No	MPC
14	QA metrics and sky-coverage maps	ASCII, PNG, MOV, FITS	Real time and daily	Subset	Archive Metadata

moving objects is around $\sim 10^2 - \sim 10^3$ per night after filtering and ML vetting (Duev et al., 2019).

The real-time transient alerting system takes about 30 minutes from the image being taken at Palomar to notification on the ZTF Alert Distribution System (ZADS, Patterson et al., 2019).

The full set of data products available from ZTF, some of which have been used in this project are shown in Table 2.8.

2.3.2 ZTF Assessment and Residual Modelling

To understand if the luminosity of a source is varying outside its quiescent state, requires an analysis of the object to identify statistical outliers. To understand if a measurement is an outlier, requires quantification of the uncertainties in the measurement to ensure that true variations in the source can be identified.
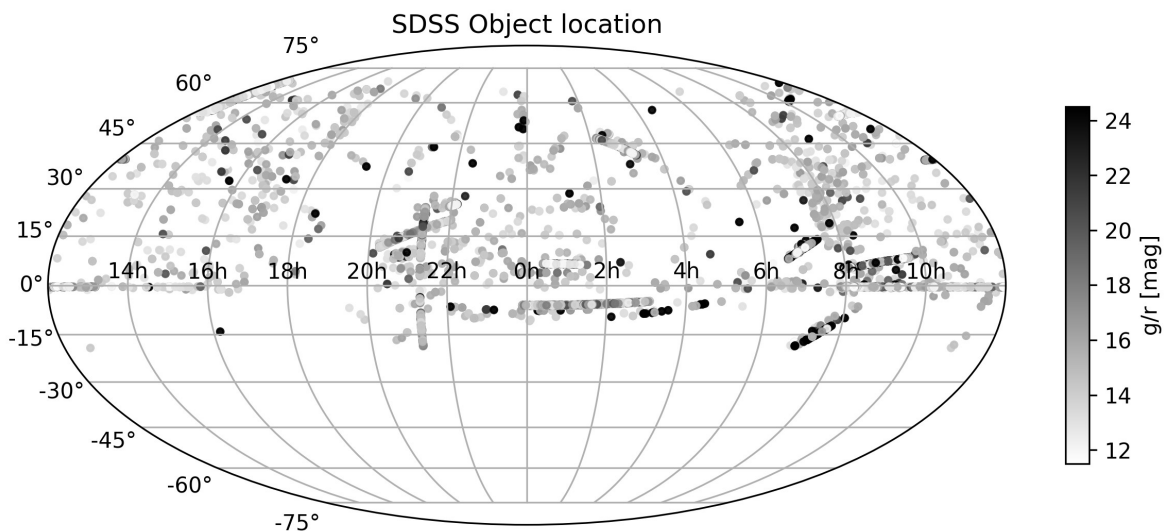
To assess the uncertainties in ZTF measurements, a random sample of stars, across the range of magnitudes appropriate to the observatory, were selected. The magnitude range of the facility, for the purposes of the assessment, was taken to be 12-23 mag

largely to ensure coverage from fully saturated measurements to in excess of the limiting magnitude of the facility. It was noted that the majority of public survey images are taken with exposure times of 30 seconds, which leads to the limiting magnitudes quoted above (Table 2.7). However, as discussed above (§2.3.1), data from ZTF partnership surveys is available after a proprietary period, and some of this imaging was performed to a greater depth, e.g. with exposures of 90 seconds or greater, for which the limiting magnitude would be improved.

The sample stars were randomly selected from the SDSS catalogue (DR13) in 0.25 mag bins, with 200 objects per bin. The random nature of the sample was determined to be a function of the process for returning the data from the SDSS database using the Astroquery package (from SDSS Sky Server), selecting the PhotoPrimary view, which is derived from the PhotoObjAll table. The first 200 objects were returned which met the criteria of having a g mag within the magnitude bin, declination $-20° \leqslant \delta \leqslant 70°$, type classification of 6 (i.e. a star) and a mode value of 1 (indicating the observation is a primary object). The random nature of the sample, in terms of sky location was confirmed by visualisation of the sample set as shown in Fig. 2.7 and deemed to be acceptable for this assessment.

If the luminosity of a source is truly constant, then we can argue that any variation in the measurement of its apparent magnitude is due to atmospheric variability and instrumental uncertainty. Although the ZTF facility has an observing strategy which tries to optimise the limiting magnitude, and schedule targets on the basis of factors such as seeing, air mass and sky brightness (Bellm et al., 2019b), this optimisation is not (to date) dynamically adaptive throughout an observing session. This means that cloud and changes in seeing, for instance, can have a marked effect on imaging. Nevertheless, if we assume the distribution of uncertainty associated with atmospheric effects is Gaussian they can be thought of as constant to a first order.

Additionally, we cannot assume that all the sources in our random sample exhibit a constant luminosity. Many stars show signs of variability, whether intrinsic such as Cepheids or RR Lyrae, or extrinsic such as eclipsing binaries, and so ultimately to deter-


Figure 2.7: On sky location of SSDS reference objects, used for assessment of uncertainty in ZTF measurements.

mine a baseline uncertainty for the ZTF and its observations, this source of variability must be rejected.

Therefore, an estimate of ZTF instrumental uncertainty was achieved by performing a sigma clip on the summary data of processed light curves for each SDSS object. From the SDSS star positions, cross-matched objects (within $\leqslant 2''$) were obtained from the ZTF and where available light curves for these objects were downloaded.

The standard deviation (σ) for the magnitudes measured in a light curve was calculated giving the photometric distribution for that object. From the distribution of all objects in a magnitude bin, the median and standard deviation for the bin could then be determined and used to iteratively reject any individual samples which were outside 3σ for the total bin. A maximum of 3 iterations were carried out to reject outliers of variability in each bin, and this was completed for the entire magnitude range.

The results of the above exercise are shown in Fig. 2.8 for both the *g* and *r* filter bands. Qualitatively, the shape of the curve is as expected. At brighter magnitudes there is increased scatter and an upturn due to saturation of the CCD sensor pixels. At dimmer magnitudes, the curve exhibits gradually increasing scatter, result-
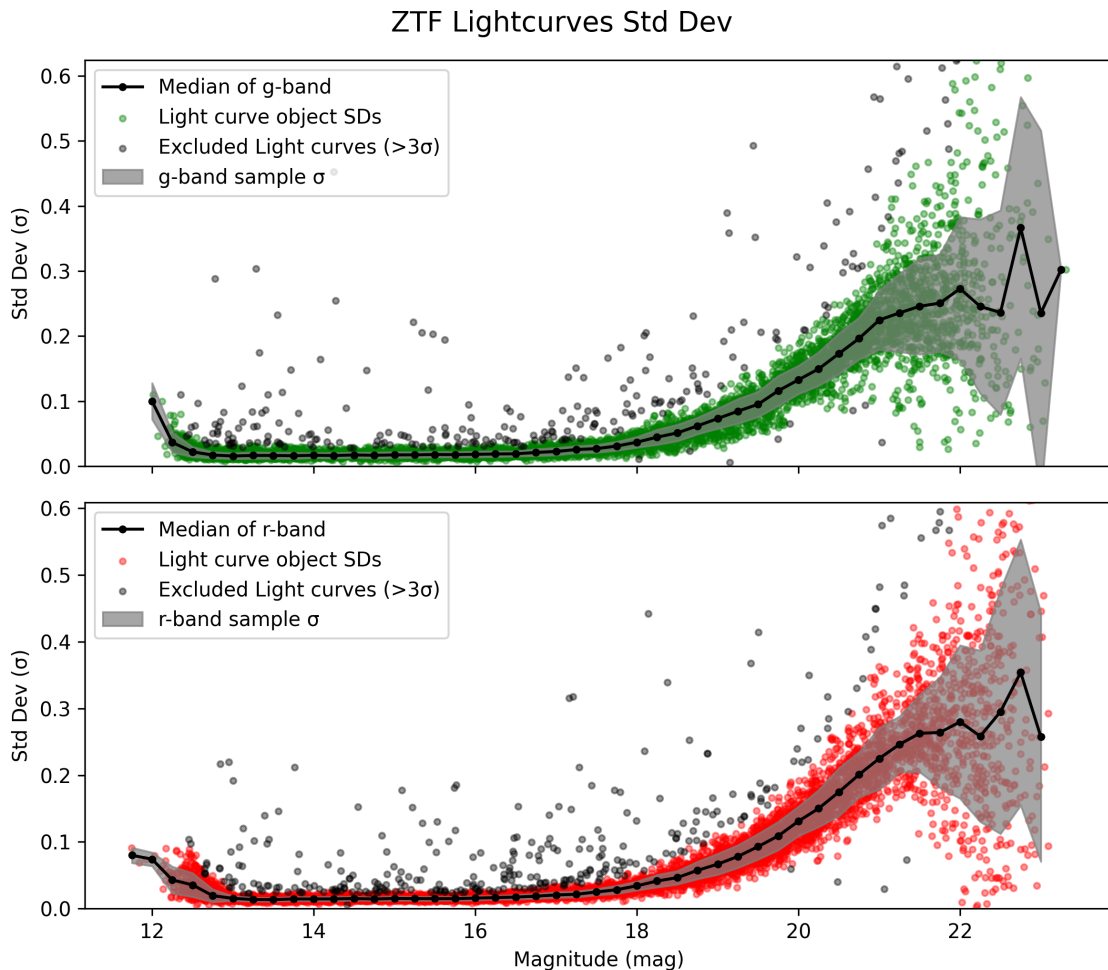
Figure 2.8: Standard deviation on 200/0.25 mag bin SDSS star sample from ZTF light curves. Solid lines show the median of the light curve SD for each magnitude bin. Gray shading show the 1σ on the sample and green and red coloured circles show 3σ, with grey circles indicating rejected samples.

ing from a decreasing signal to noise ratio as the limiting magnitude of the facility is approached. The downturn and indeterminate variation on the median, at magnitudes dimmer than ~21 mag in both filters, is thought to be due to both an increasing lack of ZTF objects at lower magnitudes, and also a reduction in the total number of samples per light curve. For instance, taking data throughout the initial ~3 years of operation, the mean samples per light curve is ⩾100 in the $g(r)$ filter up to 20.25 (21.0) mag, but drops off considerably at dimmer magnitudes. No analysis was carried out on the seeing conditions associated with these general statistics.
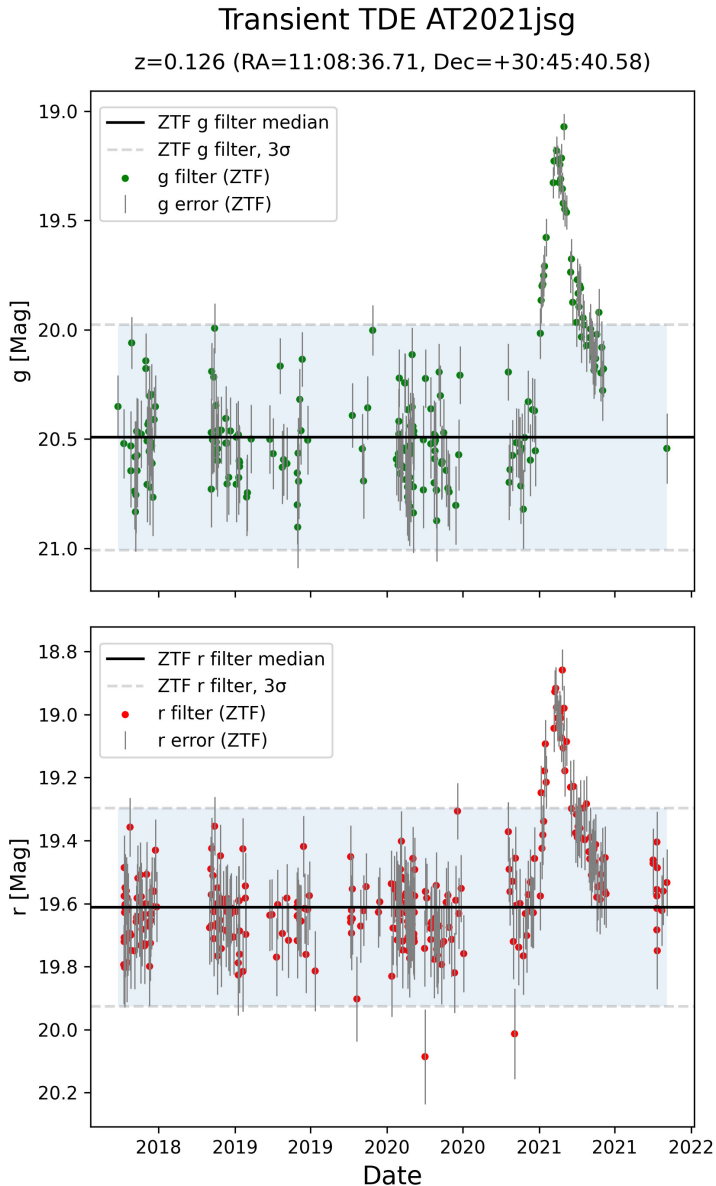
Figure 2.9: ZTF Light curve data for TDE AT2021jsg, used as a test target to illustrate requirements for an algorithm for detecting potential candidates. Consecutive detections (as discussed in the text) and correlation between filters are critical factors.

A best-fit curve was generated from the median of the standard deviation (using Numpy polyfit) to be used later as a measure of expected scatter for a constant luminosity source to facilitate transient identification. At this point, from the noise modelling carried out, we had a first-order scatter associated with the light curve photometry measured for ZTF objects. This had been estimated on an empirical basis throughout the facility's full magnitude range. This function was used in the following light curve analysis (Chapter 3) where multi-epoch photometry associated with CSS at ZTF object positions were analysed to provide an indication of statistical outliers. The presence and profile of the outliers was then be used to flag objects of interest for visual inspection.

Nevertheless, despite being able to identify outliers, a single epoch observation in a light curve was deemed necessary, but insufficient to reliably flag an object of interest and thus leave the algorithm susceptible to spurious noise associated with the source environment (e.g. proximity to a galaxy). Therefore, further development of the algorithm was considered necessary to provide a more robust indication of objects in

which a statistically significant transient existed.

As discussed in §1.4, the type of transient we are looking for is likely to increase the luminosity of the source over several weeks/months, therefore additional validation was put in place to count series of consecutive outliers, and the occurrence of this over the entire light curve was also provided. From comparison with test TDE light curves, it was noted that a high number of consecutive samples outside the 3σ uncertainty range discussed above, would be more indicative of a flare / TDE signal. This is in comparison to a low number of consecutive samples, occurring repeatedly throughout the period of the light curve which is more likely indicative of low signal to noise (S/N) imaging[14]. For example, Test TDE #1 (AT2021jsg) as shown in Fig. 2.9 showed 27 consecutive detections and Test TDE #2 (AT2019qiz - not shown) exhibited 61 consecutive detections, both across g and r filter bands. Note that the nature of the validation, would necessarily reject any detections in which the outliers were not correlated across both filter bands. Nevertheless, no attempt was made at this stage to determine the measure of cointegration between the two passbands.

In order to reject signals with a low signal to noise, further indications were provided by setting a maximum absolute count of outliers and a maximum proportion relative to the total number of samples in the light curve. However, these thresholds were left high initially (i.e. unset) as it was thought that additional test targets would be required to tune these and the other parameters to the point where they could be used.

---

[14]Noting that low S/N could either be seeing related, or intrinsic to the region in which the CSS is viewed, e.g. high surface brightness.

Chapter 3

CSS Catalogue - Light Curves

The previous sections have detailed research into the profile and longevity of a TDE (§1.4), CSS position data which has been consolidated from literature (§2.1), and a high-level detection algorithm which can be applied to light curves downloaded from the selected time-domain facility, ZTF (§2.3.2). During the research Python scripts were set up to download light curve data from ZTF and assess the possibility of a candidate TDE existing in the photometry.

In general terms, the analysis process followed for the CSS sources involved querying the ZTF archives at NASA/IPAC-IRSA with a search radius to 2″ at the RA and Dec of CSS catalogue positions for g & r filter data. ZTF generate light curves for sources from their epochal source PSF-fit photometry catalogue (product ID#3, see Table 2.8) where source positions are seeded from the reference image source PSF-fit catalogue (product ID#7, see Table 2.8). Given the ZTF resolution is $\sim 1''$/pixel, with a maximum quality of $\sim 2''$ FWHM, a cone search within that radius to correlate with reference object positions was deemed appropriate. Additionally, it was noted because there is some overlap between ZTF pointing fields, and since reference objects are allocated on a per field basis, there are some duplicate objects - i.e. the same physical object may be represented by multiple object identifiers (OIDs) in the ZTF archive. OIDs are also allocated on a per filter basis meaning many of the searches came back with multiple objects which were consolidated to reconstruct the light curve. The fact that multiple OIDs were combined was logged but subsequent statistical data was recorded against the OID which contained the greatest number of single epoch visits, and was defined as the primary OID in each filter.

Two sets of searches were considered from the CSS catalogue data, (1) those based on Milky Way and local objects and (2) those based on extragalactic objects. This cut was made at an arbitrary luminosity distance of $d_{\mathrm{L}} \leqslant 27$, or ~ 2.5 Mpc. Not surprisingly,

Table 3.1: CSS catalogue summary information

	Local			Extragalactic		
Total Objects		158			1484	
	Min	Median	Max	Min	Median	Max
Distance (Mpc)	0.002	0.009	0.81	3.77	16.52	891
Distance (d_{L})	11.71	14.87	24.53	27.88	31.09	39.75
Size Rh (pc)	0.78	2.98	113	0.9	15.81	671
Size Re (″)	12.6	58.2	300	0.01	0.14	6.9
Mass (10^6 M$_\odot$)	0.003	0.16	25700	0.12	3.72	23400

the extragalactic based objects amounted for the vast majority of the CSS inspected with 1484 objects in total compared to only 158 which were local objects.

Other summary statistics, as given in Table 3.1, show the median angular size of the extragalatic sample objects was 0.14″, while only 3 objects of the (non-zero) entries projected a size >2″ on the sky (most likely cEs). This further illustrates that these objects, at the distances considered, would effectively be point sources in ZTF imaging within the 2″ FWHM resolution.

Table 3.2: Example of the summary statistics retrieved / calculated on a per object basis for high-level analysis of light curve data extracted from ZTF archives.

Column Name	Description	Units	Example Data	
Name	CSS catalogue ID	-	VCC1871	
RA	CSS catalogue RA	deg	190.315417	
DEC	CSS catalogue DEC	deg	11.387222	
Description	Short description	-	Virgo_31.08_12 41 15_+11 23 14	
ZTFObject	Reference object found in ZTF archive	bool	True	
ZTFOutliers	Outliers exist (>3sigma)	bool	True	
MaxConsecOutliers	Max number of consecutive outliers	-	10	
ConsecRuns	Count of independent consecutive outlier runs	-	83	
			f*= g	f*= r
ZTF(f*)oid	Primary ZTF Object ID	-	525105100017169	525205100008446
ZTF(f*)filterID	Filter ID	-	g	r
ZTF(f*)Samples	Samples returned	-	435	538
ZTF(f*)MAD	Median absolute deviation		0.0543	0.0478
ZTF(f*)SD	Standard Deviation		0.1234	0.0869
ZTF(f*)Median	Median	mag	16.22	15.41
ZTF(f*)Mean	Mean	mag	16.19	15.40
Stat(f*)Included	True if statistics calculated	bool	True	True
ZTF(f*)RefMag	Primary OID reference mag	mag	16.22	15.42
ZTF(f*)med_16pc_diff	Difference between median and 16th percentile		0.1152	0.0819
ZTF(f*)deltaTMin	Single epoch minimum interval	days	0.000451	0.000451
ZTF(f*)deltaTMean	Single epoch mean interval	days	2.7533	2.4307
ZTF(f*)deltaTMedian	Single epoch median interval	days	1.0000	0.9604
ZTF(f*)deltaTMax	Single epoch max interval	days	133.32	130.28
ZTF(f*)deltaTSD	Single epoch interval standard deviation		10.66	10.23
ZTF(f*)OutlierCount	Count of 3sigma outliers	-	186	194

On the other hand, due to the proximity of the Milky Way sources, the angular size they project on the sky is larger than for the extragalactic objects, and thus the PSF-fit light curve was considered ill-suited to this size of object. While a rough inspection was carried out on these local sources, it was noted further development of other techniques would be required to robustly validate transients within these objects.

As noted by the ZTF[1], much effort had been put into early stage quality assurance

---

[1]The ZTF Science Data System (ZSDS) Explanatory Supplement, Chpt.13 - Cautionary Notes. https://web.ipac.caltech.edu/staff/fmasci/ztf/ztf_pipelines_deliverables.pdf

of the automated image processing pipeline, but it was still possible that bad data could affect product quality. Metadata was, however, included with the archives, with the *catflags* metric specifically providing an indication of potential issues for light curves. While ZTF advise interrogation of bit 15 (i.e. *catflags* < 32768) for a usability indication of each single epoch sample, for the highest data quality none of these bits should be set. Therefore to ensure the best quality data was extracted, a constraint on *catflags* = 0 was included in the query against the archive.

After download from the NASA/IPAC-IRSA archive, a plot of the light curve data was prepared with both *g* & *r* filter data, if available, on a common timescale. Additionally, summary information was determined for each dataset (see Table 3.2). This summary information was intended to provide a quantitative assessment of the data for comparative purposes. For each set of filter magnitude data, metrics included the number of samples returned, the median absolute deviation of the samples, the standard deviation, median and mean. Additionally, a similar set of quantities was determined for the cadence information, again independently for each filter, and based on the intervals between samples including interval minimum, mean, median, maximum and standard deviation. Finally, a total count of outliers was included. The only temporal metric which was determined through the combination of both *g* & *r* filters was the count of consecutive outliers mentioned above.

Table 3.3: Overview of the statistics from the final run of the CSS catalogue extragalactic sample against the ZTF reference object light curve catalogue.

Item	Count	Description
Total entries	1484	Total entries used from the CSS Catalogue
ZTF objects	1072	Catalogue entries for which a ZTF reference object exist
ZTF g objects	970	Catalogue entries for which a g filter object exists
ZTF r objects	1064	Catalogue entries for which an r filter object exists
ZTF g/r objects	962	Catalogue entries for which ZTF reference objects exist in both g & r filters
Outliers	823	Objects for which the light curve has at least one outlier
Outliers g	619	Objects for which the light curve *g* outliers ≥ 1
Outliers r	701	Objects for which the light curve *r* outliers ≥ 1
Outliers g/r	497	Objects for which the light curve *g* & *r* outliers ≥ 1
Outliers g/r 2	295	Objects for which the light curve *g* & *r* outliers ≥ 2
Consec Outliers 2	285	Light curves with ≥ 2 consecutive outliers (filter indefinite)
Consec Outliers 4	109	Light curves with ≥ 4 consecutive outliers (filter indefinite)
Consec Outliers 8	29	Light curves with ≥ 8 consecutive outliers (filter indefinite)

3.1 Results

After execution of the script to extract the light curves for the CSS objects, an initial inspection of the calculated summary data as described in Table 3.2, allowed a straightforward assessment of the data for the entire CSS Sample. This information is summarised in Table 3.3, with the counts in each row illustrating the benefit of a progressive filtering approach.

Having reduced the initial list of CSS catalogue entries to a more manageable list of items, the remaining objects could then be analysed in more detail. As plots of the light
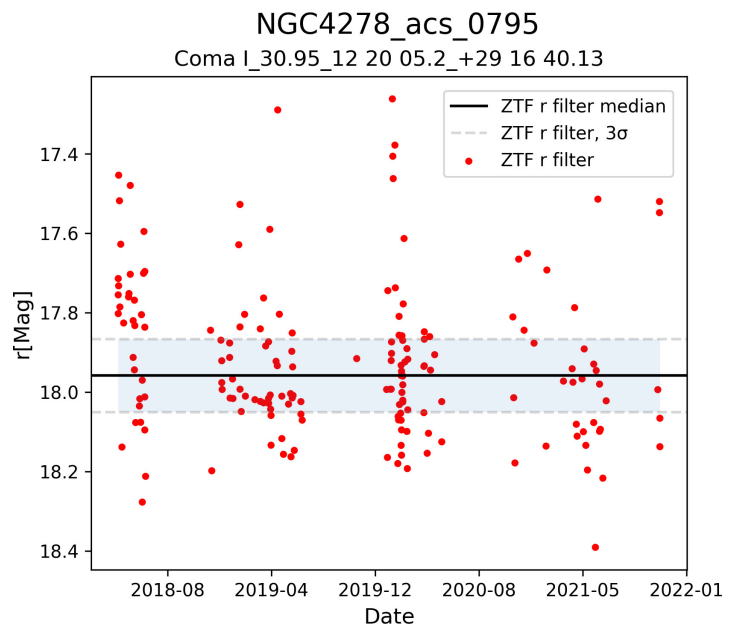
curves had been generated during the initial data extraction and download process, these images could now be inspected.

The light curves for the 29 objects with $\geqslant 8$ consecutive outliers were considered as objects of interest, and were sorted into a list of decreasing count of maximum consecutive (MC) outliers while minimising the count of consecutive runs (RC). A visual inspection for each of the plots was carried out, for which the details and a commentary are included in Appendix A. In summary, none of the light curves showed any discernible evidence of a transient signal despite in some cases many consecutive outliers, e.g. NGC4278_acs_0795 (Usher et al., 2013), as shown in Fig. 3.1 had maximum of 14 consecutive outliers with more outliers recorded over 19 separate runs, although this was only in one filter. All of the light curves showed evidence of seasonal pointing scheduling, but environmental effects such as high cloud or variable seeing throughout a session could not be corrected through the automated pipeline.

As the number of consecutive outliers is relatively low throughout the population of CSS objects, it is possible that the approach would respond well to techniques which improve the signal to noise, for example, sample binning or rolling average. These techniques would clearly have to be used with caution as too much smoothing would risk erasing signs of true source variability. However, consolidation of data, especially of same night visits or over short cadence timescales may prove beneficial. Nevertheless, this was not thought necessary at this stage and would have over-complicated the initial exercise. Furthermore, the author notes that ZTF reference object magnitudes have been generated from source extraction on multiple (i.e. $\geqslant 20$) co-added

Figure 3.1: Example plot of one of the 19 CSS objects of interest, NGC4278 ACS 0795, which emerged after filtering as described in the text. The image was chosen to illustrate a typical noise content on many of the light curves.

single-epoch images. Based on the rough analysis in §1.4, any TDE transients visible should experience a considerable increase in luminosity ($\gtrsim 1$ mag) over a minimum of 30 days before dimming over several months. There were no signals which fit this profile, or which might even be considered the 'tip' of this profile.

Despite confidence in the algorithm to provide a simplistic, but robust indication of potential transients in the light curves at the CSS object positions, the author nevertheless carried out a visual inspection of all of the light curves (1072) which had been produced from the original data extract. No evidence of any transient events, of any sort, was noted.

3.2 Image Analysis

While it appeared on the face of it there was little uncertainty from the above search, after scanning through many hundreds of light curves, the author wanted to investigate why some of the images were significantly noisier than others.

This investigation commenced by obtaining reference and median images from the ZTF archives, as shown in Fig. 3.2. As discussed previously, the reference images (top row) are co-added from a minimum of 20 single epoch images, and the median image (bottom row) was the single-epoch imaging found to be closest to the median reference magnitude value. For illustration purposes, the same object referenced in the previous section is included here. Cutouts of size $5'0''$ (left), $1'0''$ (centre), $0'12''$ (right) from the ZTF archive are centered on the object position, to show the context of the object proximity. The bright object in all three cutouts is the elliptical galaxy NGC4278 (in
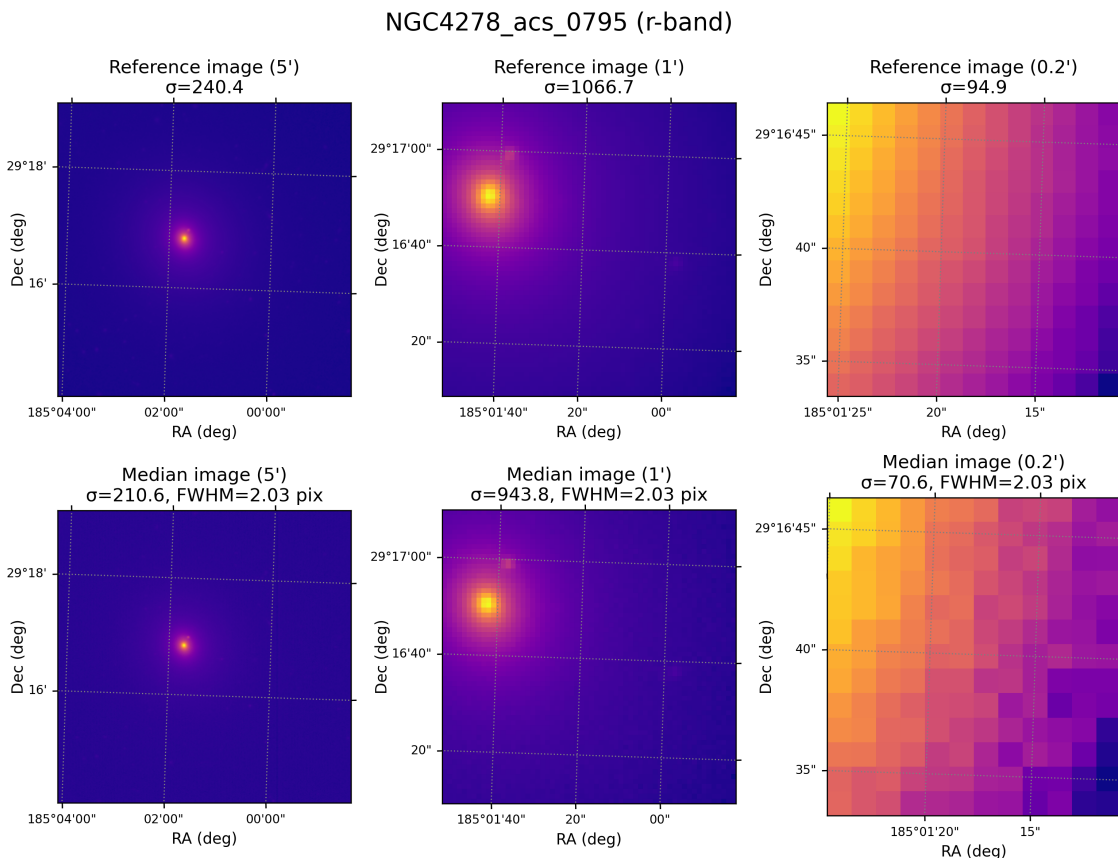

Figure 3.2: Example of the co-added reference (top) and single-epoch median (bottom) images centered on NGC4278 ACS 0795. Left to right, cutouts of size $5'0''$ (left), $1'0''$ (centre), $0'12''$ shown. Standard Deviation (σ) of pixel intensity included for all cutouts, with seeing metadata (FWHM) for single epoch imaging.

Coma Berenices). Each of the cutouts also shows the standard deviation of the pixel intensity across the image, and the single-epoch median images also include the associated value of seeing (pixels) from the image metadata.

Figure 3.2 illustrates the noise reduction in the co-added images in comparison to the single-epoch exposure, despite almost perfect seeing (2.03 pixels) for ZTF in the captured image. The object in question is difficult to discern at these contrast levels, but the extent

of the elliptical galaxy (NGC4278) is clear. From this it appears that the CSS, determined by Usher et al. (2013) to be a GC, is well within the half-light radius of the elliptical and this is confirmed as Cappellari et al. (2011) determine the effective radius (R_e) of NGC4278 to be $\sim 32''$, or 2.4 kpc at the assumed distance of 15.6 Mpc. From this we must assume that the photometry is contaminated by the surface brightness of the host galaxy and the PSF fitting is inaccurate. This is confirmed through comparison between the measured magnitude (reference median r filter 17.73 mag) and the g/z magnitudes from Usher et al. (2013) of 22.16 and 20.93 mag, respectively.
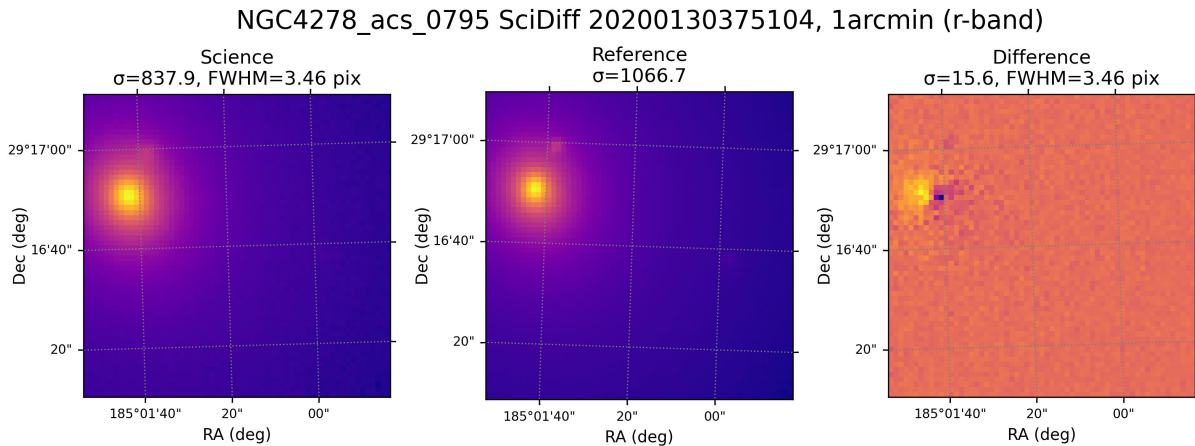

Figure 3.3: Comparison of ZTF single-epoch science (left), co-added reference (centre) and difference images (right) for NGC4278 ACS 0795. This is the imaging for the highest measured magnitude from the light curve for this object (see Fig. 3.1).

A comparison of a single-epoch science image with the co-added reference image, giving the difference image, was made. Fig. 3.3 shows the $1'$ cutouts for the outlier in Fig. 3.1 with the highest magnitude. The difference image shown is an example of that used in the ZTF alert pipeline which will be discussed in more detail in the next sections. Qualitatively, several points were noted from the difference image. There are clearly limitations in the subtraction of the host galaxy, although the image appears largely 'flat' outside of the bright core and the low standard deviation of the cutout appears to confirm this. The seeing associated with the exposure is also relatively high i.e. 3.46 pixels FWHM, compared to $\sim$2 pixels under perfect conditions.

To investigate the potential effects of seeing and airmass on scatter within the light curve samples, ZTF metadata for two CSS objects in the sample were extracted. This required downloading of the metadata for every single-epoch science exposure, so in some cases was time consuming, but the author thought a comparison of seeing and airmass against sample magnitude offset from the median reference, would confirm their effect on light curve sample distribution.

Fig. 3.4 shows a comparison between two objects, M59-UCD3 (Sandoval et al., 2015) in the left column and NGC4278-ACS-1369 (Usher et al., 2013) in the right column, which were selected as representative of tight and wide sample distributions, respectively. For context, M59-UCD3 had 197 samples included (85 g, 112 r) with only 1 outlier in the r filter, and NGC4278-ACS-1369 included 1495 samples (668 g, 827 r) with 79 outliers (25 g, 54 r).

The validity of using these objects is confirmed in the top row of Fig. 3.4 which shows the magnitude distribution of the samples for the light curves of the two objects in comparison to a normal distribution, based on the reference median and σ values calculated
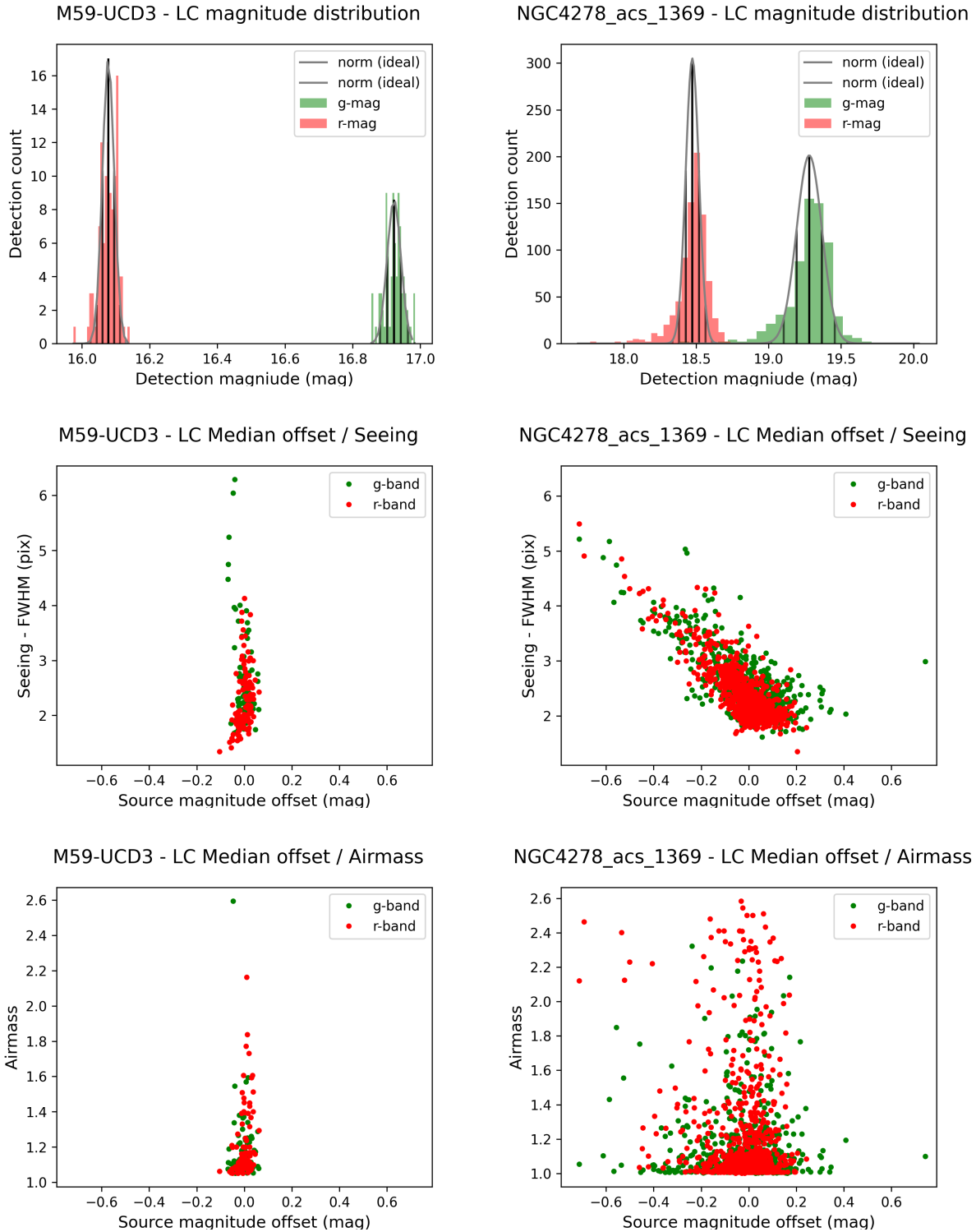
Figure 3.4: Analysis of effect of seeing and airmass on light curve sample distribution. (Left column) M59-UCD3 exhibits a tight distribution with only 1 outlier in 197 samples. (Right column) NGC4278 ACS 1369 shows a wider distribution with 79 outliers across 1495 samples in both filters. (Top row) Magnitude distribution in ZTF g and r filters. The narrow and wide distribution, in comparison to the expected instrumental normal based on earlier measurements is evident. (Centre row) ZTF sample seeing estimate vs median magnitude offset, showing a relationship between seeing and magnitude offset in the wider distribution case. (Bottom row) ZTF sample airmass estimate vs median magnitude offset, with a marginal relationship evident.

earlier (see §2.3.2). The fit of M59-UCD3 (Fig. 3.4-left) to a normal distribution is better than that of NGC4278-ACS-1369 (Fig. 3.4-right), which is clearly wider with a greater proportion of samples outside the 3σ range. The middle row of Fig. 3.4 shows the sample seeing against offset of magnitude to the median. In the tight sample object (left) the magnitude offset from the reference magnitude is minimal, but for the wider sample object (right) a decreasing magnitude offset to reference magnitude with worsening seeing is evident. In the bottom row of Fig. 3.4, a similar result is shown in respect of airmass against reference magnitude offset, although in this case the wider distribution (right) merely shows more scatter about the reference magnitude, without any discernible trend.

The above analysis would suggest that seeing is a more important factor than airmass alone, but even then, seeing is not the only factor in play here which reduces to the spread of the sample photometry to wider levels. As NGC4278-ACS-1369 is similar to that discussed, in that it is close to the elliptical galaxy NGC4278, and even this object at a higher $g = 19.94$ mag suffers increased noise due to proximity to its host.

In this chapter we have used multi-epoch ZTF observations, in the form of light curves to search for evidence of TDEs in CSS, which are dense stellar environments potentially containing nuclear IMBH. Inspection of the light curves of ZTF objects associated with these CSS positions showed no indications of any disruption events. The implication of this is discussed in Chapter 6.

Chapter 4

CSS Catalogue - Transient Alerts

As mentioned in Chapter 3, the ZTF facility uses a source extraction algorithm on co-added images to define a catalogue of reference object positions. A PSF fit at these reference object positions is carried out after every visit, on science images to produce the light curve photometry. The advantage of this technique is its efficiency for isolated point sources at positions which are previously known. For the purposes of this project, the fact that the photometry of point sources are well represented was not an issue in itself, with most of the CSS being considered effectively presenting as point sources as shown for extragalatic objects in Table 3.1. Nevertheless, this does become an issue for sources in close proximity to their host galaxy as explored in the image analysis of Chapter 3. A further disadvantage of this approach is that light curves are unavailable for objects which are not in the ZTF reference catalogue.

With that in mind, a different approach was taken to search directly for transients at the known positions from the CSS catalogue. This second technique involved querying alerts flagged from the ZTF alert pipeline (see §2.3.1). Although this pipeline still relies on the existence of a reference image, it does not require a priori object positions, as an alerting algorithm functions directly on the difference between the science images and reference images. After filtering for instrumental artefacts and physical anomalies (e.g. plane / satellite streaks), alerts are notified, in near real-time, to a network of alert brokers.

Table 4.1: Overview of the statistics from the final run of the CSS catalogue extragalactic sample against the ZTF alerts database.

Item	Count	Description
Total entries	1484	Total entries used from the CSS Catalogue
Alerts $r \leqslant 1'$	833	Object alerts within 1 arc min of CSS position
Alerts $r \leqslant 10''$	67	Object alerts within 10 arc sec of CSS position
Alerts $r \leqslant 2''$	34	Object alerts within 2 arc sec of CSS position

The same positional information as used in the previous section was reused here, and applied through a cone-search query against the Las Cumbres Observatory (LCO) 'Make Alerts Really Simple' (MARS)[1] host site using a JSON based API script. To provide context to the search a progressive reduction in radius was carried out for each position,

---

[1] https://mars.lco.global
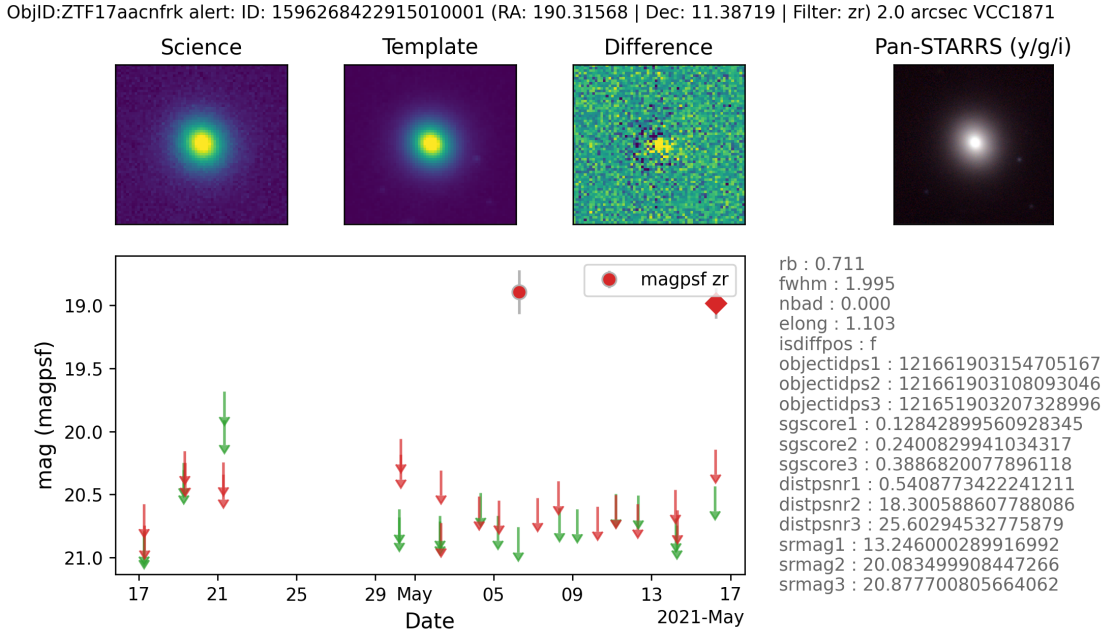
(a) Alert ZTF17aacnfrk within $2''$ of VCC1871, a Virgo cluster cE. The angular size is estimated at $6''9$ with $M_{\mathrm{star}} \approx 2.34 \times 10^{10}$ M$_\odot$ (Ferrarese et al., 2006). The metadata for the PanSTARRS #1 object, e.g. $distpsnr1 = 0.541''$ indicate this alert is close to VCC1871, so the alert is likely associated with image subtraction and PSF fitting limitations due to high surface background in proximity to the host galaxy.
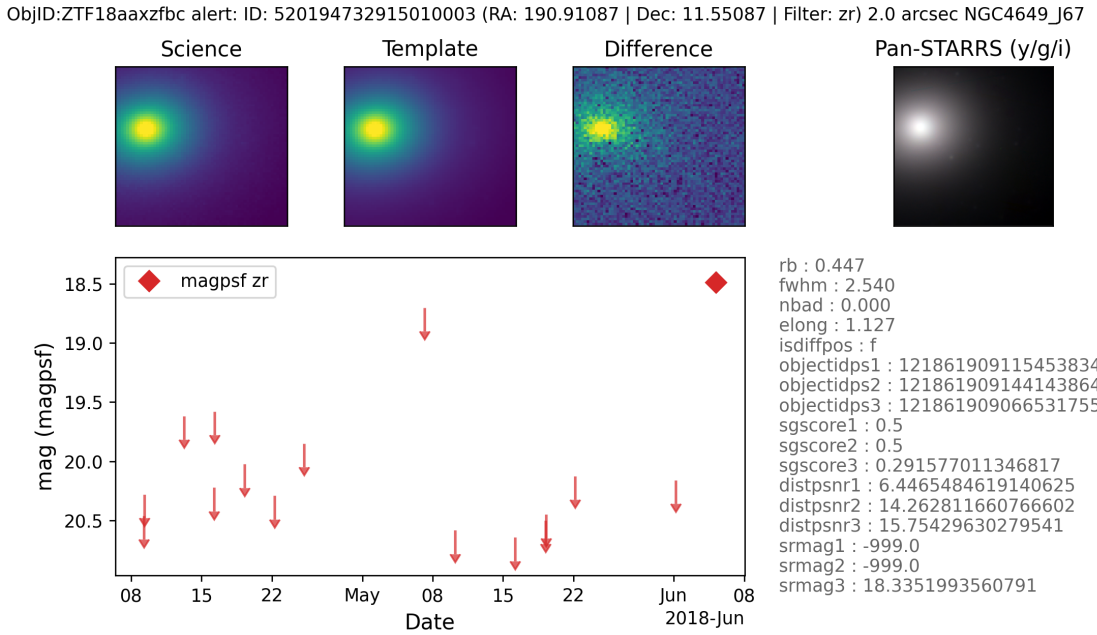
(b) Alert ZTF18aaxzfbc within $2''$ of NGC4649-J67 (Strader et al., 2012b), a UCD hosted by the massive Virgo elliptical NGC4649 (M60). The UCD is unresolved but with a 1.8 kpc galactocentric distance (Strader et al., 2012b), is well within the ($\sim$10 kpc) R_e of NGC4649. A single transient detection and low rb score suggest this is a false positive related to the transient source's proximity to the host galaxy.

Figure 4.1: Typical ZTF alert files centered within $2''$ of 2 CSS positions. Science image from the alert epoch, co-added template (reference) and difference image cutouts are shown. ZTF images are 63×63 pixels ($\sim 1'$ sq.) Also included is the corresponding PanSTARRS image of the same area. PSF Light curve photometry consists of 30 days prior to alert, with upper limit red and green arrows indicating non-detections in r&g filters respectively. Metadata is included, as explained in the text.

51

i.e. centered on the CSS catalogue position, a cone-search was performed at $1'$, $10''$, $2''$ radius.

4.1 Results

A summary count of the transient alerts, found from searching within the stated radii of the CSS catalogue extragalatic sample positions, is shown in Table 4.1. Image cutouts were obtained and inspected for the 101 objects (within $10.0''$) in the ZTF AVRO format, which includes a significant amount of metadata relating to the alert and its associated position (Bellm et al., 2019a). For example, as shown on the plots (e.g. Fig. 4.1) alert metadata includes a real/bogus (*rb*) assessment, the FWHM from the science image (*fwhm*), a count of (pre-tagged) bad pixels in a 5×5 square (*nbad*), and the source extraction elongation (*elong*). Position metadata consists of information such as the ID (e.g. *objectidps1*), star/galaxy score (e.g. *sgscore1*), distance (e.g. *distpsnr1*) and filter appropriate magnitude (e.g. *srmag1*) to the nearest three PanSTARRS objects (if within $30''$). Other metadata is also available in the AVRO file for interrogation which is not shown on the plots[2]. Each alert has a unique Alert ID, and is also allocated to an object ID, which is reused for subsequent alerts at the same position.

Fig. 4.1 includes 2 of the 34 alerts within $2''$ of CSS positions, to illustrate the format of the ZTF notifications in general, and interpret resulting alerts. Fig. 4.1a shows alert ZTF17aacnfrk, found to be within $2''$ of VCC1871, a cE in the Virgo cluster (Binggeli et al., 1985). The angular size is estimated at $6.9''$ and the cE mass as $M_{\text{star}} \approx 2.34 \times 10^{10}$ $M_{\odot}$ (Ferrarese et al., 2006). From the PanSTARRS #1 metadata included, the alert is coincident with VCC1871. As the light curve does not show any rise in profile over previous epochs, and there are no detections in the g filter, this alert is suspect and likely associated with image subtraction and PSF fitting limitations for an extended object.

Table 4.2: ZTF transient alerts raised within $2''$ of CSS catalogue positions (34 from 1484 extragalactic sample). Transient object ID is unique to position and used to correlate repeat transients determined at the same RA/Dec, whereas Alert IDs are unique.

| CSS Object	RA	Dec	Transient Object ID	Alert ID
NGC4467	187.375833	7.992778	ZTF18aahvedj	1764541880615010000
VCC1199	187.395833	8.058056	ZTF18aahveds	1551320760615010000 7893576206150100000
NGC4486B	187.633208	12.490167	ZTF18aaitueo	1768549783815010000 1763546443815010000
			ZTF18aamqzcp	1763539353815010000
VCC1627	188.905	12.381944	ZTF21aadkwba	1471481433415010000
VCC1871	190.315417	11.387222	ZTF17aacnfrk	1596268422915010000 1586291872915010000 8033955429150200000
NGC4649_J67	190.910417	11.55075	ZTF18aaxzfbc	5201947329150100000
NGVS-UCD394	187.6313771	12.4340543	ZTF20aasuaol	1160404943815010000

---

[2]https://github.com/ZwickyTransientFacility/ztf-avro-alert

Table 4.2: ZTF transient alerts at CSS catalogue positions (continued)

CSS Object	RA	Dec	Transient Object ID	Alert ID
NGC5846A	226.621667	1.595	ZTF19aarzgmr	1602290820615010000 1536420110615010000
NGC5846cE	226.642792	1.558778	ZTF18acvlxkf	7384956206150100000
CGCG036-042	152.043	2.463419	ZTF17aabmgdx	1098438770515010000
AHcE732	181.120708	1.894103	ZTF19acmyrwr	1771534500115010000
J094729.24+141245.3	146.871792	14.212583	ZTF18acpcmbf	1551270856215010000 6854006562150100000
587733399713087000	229.321667	46.708469	ZTF18aainewq	1669283501615010000
587732157926670000	119.771667	27.459531	ZTF18aagfkqb	1698506134115010000
J125942.30+275529.0	194.92625	27.924722	ZTF18aayyphm	1771530994115010000 7862900218150100000 5471765341150100000 5282585041150100000
			ZTF18aabduzw	5531752641150100000
588016892785524000	153.43375	38.714081	ZTF18aatvifr	7015103119150100000
588298663576928000	195.792917	47.381119	ZTF18aamtgdi	1449495332115010000 1201311942115010000 5222075221150100000
587729158440681000	220.144167	3.470461	ZTF20abhkcht	1270201122215010000
587730775488200000	333.663333	13.822239	ZTF21absrisy	1684338935915010000
587726102561489000	223.497917	4.795169	ZTF18acvinaf	1438556224615010000
587736915142574000	221.782083	11.608281	ZTF18abkfeor	1154526882415010000
587733081347653000	175.6975	55.185181	ZTF18aakpbao	5282050047150100000 5181778847150100000 5251757447150100000
588018090008576000	243.17	29.513169	ZTF18aawgbhk	1687173854915010000 988123294915015000 933165174915015000
588018056734572000	243.62625	35.082081	ZTF21abvekaq	1698206303715010000
J151641.28+070006.1	229.172	7.001694	ZTF20abgfczv	1265211825015010000
588017703463026000	169.884167	12.059789	ZTF20abcrpwm	1244246854715010000
587735696987455000	212.65625	54.814839	ZTF18aayywuz	5461879024150100000
587735696989028000	218.292917	53.242661	ZTF18abgkptb	558201901915015000
587734621637509000	144.6325	38.928639	ZTF18aceqnua	6755183119150100000
588013382207012000	184.075833	51.728681	ZTF18aaqkiei	6755479902150100000
587735241710567000	128.435833	29.886131	ZTF18accvaaj	6724303302150100000
588016890635157000	146.620417	34.626269	ZTF19aatbssl	848240064415015000
587738946684059000	185.689583	39.429839	ZTF20aaitxox	1120400772315010000
587731521740603000	128.61	38.458461	ZTF18acsurai	1118287241215010000 701536041215015000
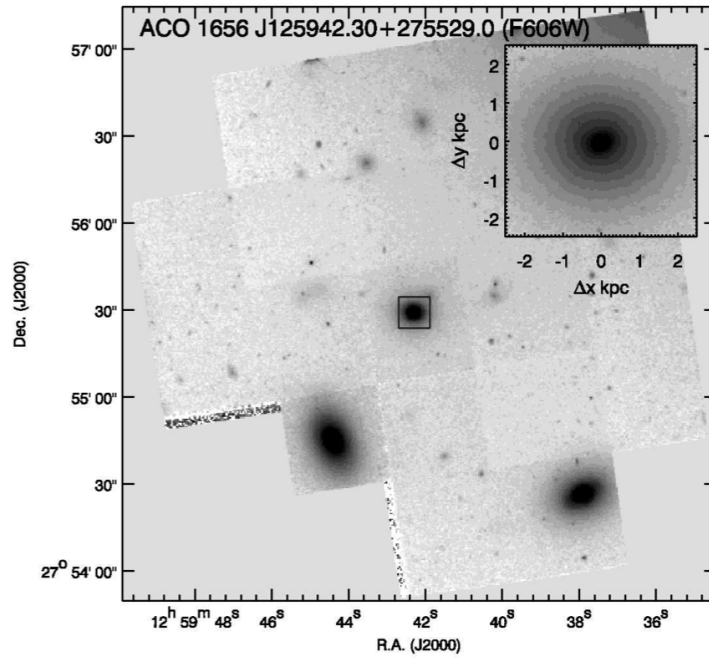
(a) Compact elliptical ACO 1656 J125942.30+275529.0 - Entire
HST WFPC2 image centered on the cE, with inset showing a 5
× 5 kpc region of the object (Credit: Chilingarian et al., 2009).
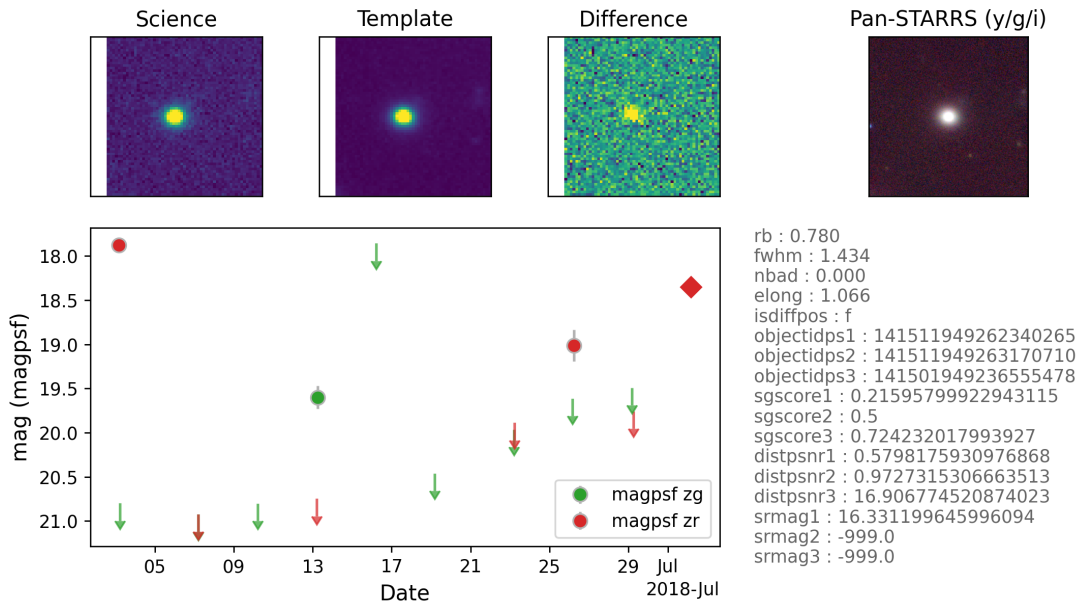
(b) Alert ZTF18aayyphm within 2″ of ACO 1656 J125942.30+275529.0 (Chilingarian et al., 2009).
Four transient alerts in ZTF *g* and *r* filters are shown for this alert object ID. It is noted that
the *rb* rating is relatively high, but a second PanSTARRS object within the search radius would
conceivably have contaminated the PSF photometry. A lack of consistent detections, or signal profile
throughout the sample period and marked ellipticity of the object (see **(a)** above) add evidence this
is a false positive alert.

Figure 4.2: Image and alert file used in analysis of cE ACO 1656 J125942.30+275529.0,
showing HST WFPC2 image and one of the four detected ZTF alert science images, with 30
day light curve.

Fig. 4.1b shows the ZTF data for alert ZTF18aaxzfbc which is within $2''$ of the UCD[3], NGC4649-J67 (Strader et al., 2012b; Forbes et al., 2013), in the halo of the massive Virgo elliptical NGC4649 (M60). Even at $R_h = 9.8$pc (Forbes et al., 2013), the UCD is resolved by neither ZTF nor PanSTARRS at the assumed 16.5 Mpc distance, but with a 1.8 kpc galactocentric distance (Strader et al., 2012b), is well within the ($\sim$10 kpc) R_e of NGC4649. A single transient detection and low rb score suggest this is a false positive associated with the proximity of the source to the surface brightness of the host galaxy.

A full list of the 34 transient alerts raised at CSS catalogue extragalactic sample positions is shown in Table 4.2. Of these, the only object with more than 3 transient alerts is J125942.30+275529.0, a cE Chilingarian et al. (2009) identified as formed through a tidal stripping episode in cluster ACO 1656. The HST WFPC2 image and ZTF alert (ZTF18aayyphm) detections, in both ZTF g and r filters, are shown for this object in Fig. 4.2. From the WFPC2 imaging (Fig. 4.2a) a marked ellipticity of the object was evident, although this was not clear from the ZTF source extraction metadata ($elong = 1.066$). Additionally, it was noted that the real/bogus rating is fair ($rb = 0.78$ for the final detection), but also, and significantly two PanSTARRS objects were within the $2''$ search radius at $0.58''$ and $0.97''$ respectively, and this could conceivably have contaminated the PSF photometry. A lack of consistent consecutive detections providing a recognisable signal profile throughout the sample period suggest this is also false positive alert.

All of the remaining alerts were similarly suspect insomuch as they were largely single transients (24 of 34 were singletons) associated with environmental or processing artefacts, and therefore without any statistical significance. As there have not been any transients visible in the light curves of ZTF reference objects at the positions of known CSS, and furthermore, there have been no statistically significant transient alerts raised at these positions either, we can say with a high level of confidence that there have been no transient events (of any sort) at these positions. As we have a time period over which the ZTF facility has been operating, we can use this to estimate an upper limit on the rate of TDEs within CSS based on our sample. This will be discussed in Chapter 6.

---

[3]NGC4649-J67 is on the definition cusp Strader et al. (2012b) describe it as a GC and Forbes et al. (2013) as a UCD.

Chapter 5

Local Galaxy - Transient Alerts

While the above sections concentrated on positions of known CSS hosted predominantly in galaxy clusters (e.g. Virgo, Fornax, Centaurus, Coma), it is probable many more of these objects are yet to be discovered. With that in mind, the approach used in Chapter 4, searching for transient alerts, was adapted for the periphery of host galaxies from ∼2 Mpc out to ∼120 Mpc, using the galaxy sample detailed in §2.1, which returned a total of 4,812 galaxies meeting the size, distance and region criteria.

Data returned also included a parameter named *logd25*, which was described as 'log of apparent diameter (d25 in 0.1′)'. This parameter was used to provide an indication of the extent of the galaxy to set the cone radius for searching for alerts, viz:

$$d_{\text{arcsec}} = 10^{\frac{60logd25}{10}} \tag{5.1}$$

and similarly, using the distance modulus and small angle formula allows a calculation of the apparent physical diameter of the galaxy

$$d_{\text{kpc}} = \frac{(m - M)d_{\text{arcsec}}}{206.265} \tag{5.2}$$

which was used to filter galaxies to a minimum apparent diameter >1 kpc.

Table 5.1: Additional data columns from galaxy proximity alert search, obtained from ZTF alert metadata, and used for data filtering and transient prioritisation.

Column name	Description	Example
Name	Galaxy principal designation	NGC2768
Hyperleda data	Downloaded data from Hyperleda - see Table 2.1	-
appDiam_arcsec	Apparent diameter (arcsec)- used as cone search radius	338
appDiam_kpc	Apparent diameter (kpc)	36.6
CountAlerts	Count of ZTF alert candidates within the search radius	32
UniqueObj	Number of unique objects associated with the alerts	18
MaxDet	Maximum number of alerts associated with one object	30
CountNSS	Count of alerts $> 2''$ from known solar system objects	32
CountNPS	Count of alerts $> 2''$ from known PanSTARRS objects	4
CountNGaia	Count of alerts $> 2''$ from known Gaia objects	12

A cone search, against the LCO MARS alert broker as used previously, was carried out surrounding each galaxy position, using d_{arcsec} as the cone radius, i.e. the search

was executed to twice the apparent diameter of the galaxy. Alerts with a real/bogus rating $rb < 0.5$ were rejected, and the remaining alert data was downloaded for further analysis. For all the alerts associated with a galaxy region, a number of additional fields were determined from the alert metadata to aid in prioritising a review of the transient candidates. This additional data, as shown in Table 5.1, included a count of the total number of alerts within the region ($CountAlerts$), the number of unique ZTF transient objects with which the alerts were associated ($UniqueObj$) and the maximum number of detections associated with a single object ($MaxDet$). The maximum detection parameter was used as a final filter to reject objects where $MaxDet \leqslant 3$. To assist in confirming the nature of the transient, the proximity of the alert candidates to objects in other catalogues was indicated through a count of alerts $> 2''$ from solar system ($CountNSS$), PanSTARRS ($CountNPS$) and Gaia ($CountNGaia$) objects.
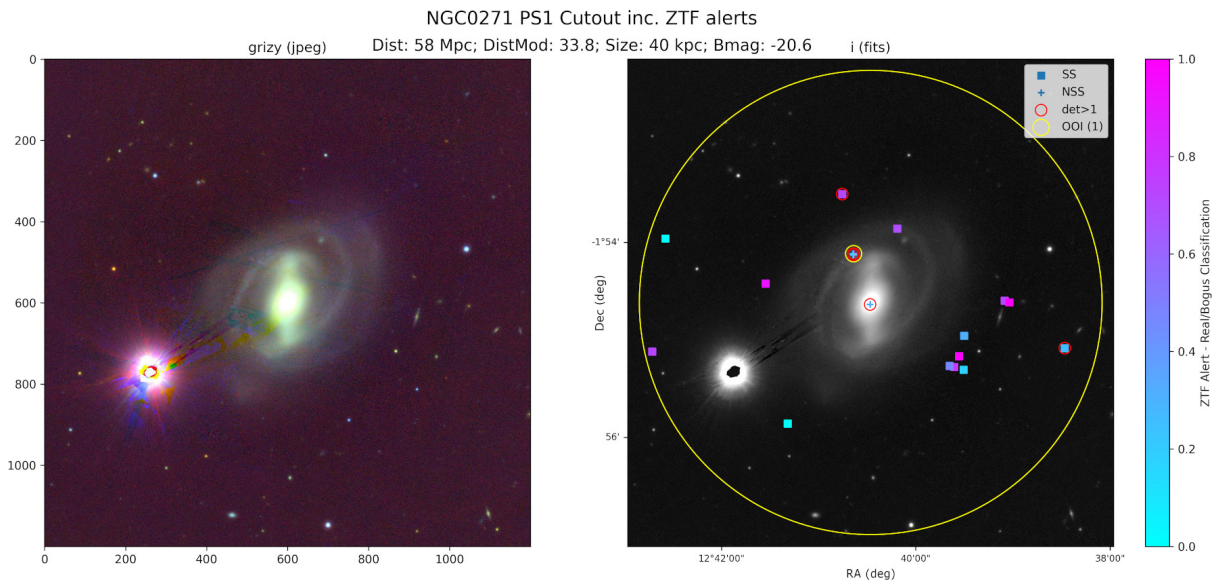
Figure 5.1: Example visualisation of ZTF alert data, overlaid on NGC0271 galaxy region. (Left) PanSTARRS $grizy_{PS1}$ image with no overlays. (Right) PanSTARRS i filter image overlaid with extent of cone search around region (large yellow circle), known solar system objects (squares), non-solar system objects (plus), objects where multiple detections have occurred (red circle), and objects of interest (OOI - small yellow circle) are ZTF alert objects after filtering, as discussed in the text. All alerts are coloured with a real/bogus (rb) scale

Applying the criteria discussed above to the data returned from the ZTF broker, reduced the data volume, and post-filtering, this data, now referred to as the 'filtered alert list', was used to visualize alerts in the context of the host galaxy. An example of this is shown in Fig. 5.1 for the galaxy NGC0271, a barred spiral galaxy in Cetus. The figure shows visualization of ZTF alert data overlaid on the NGC0271 galaxy region, and includes PanSTARRS combined $grizy_{PS1}$ filter image centered on the galaxy, but with no overlays. The second image uses the PanSTARRS i filter image, as this provided the best coverage, with overlaid symbols indicating the extent of the original cone search for alerts around the region. Additional overlays indicate known solar system objects, non-solar system objects, objects where multiple detections have occurred, and objects of interest (OOI). The OOI are the positions of ZTF alert objects after the filtering, as discussed above.

The benefit of the visualisation technique, initially as part of a prioritisation process, and latterly as an aid to specific alert analysis, was that the environment of the alert

could be quickly identified to a first order, i.e. in the example in Fig. 5.1 the OOI occurs in the spiral arm of a barred spiral galaxy. This allowed deprioritisation of alerts not likely to be of further interest, such as those in star forming regions likely associated with supernova, or nuclear alerts indicative of AGN activity.

5.1 Results

A visual analysis of the environment was useful, and quantitatively the filtered alert list gave rise to the totals as detailed in Table 5.2. Detailed analysis of alert light curves was carried out following similar processes to those for the CSS Catalogue alerts, by downloading ZTF AVRO data from the LCO MARS transient broker.

The wider volume covered around galaxy peripheries, furnished alerts with some interesting light curves, examples of which are shown in Fig. 5.2. However, at this point it became clear a large number of supernova had been returned in the search, and therefore cross-correlation of the alert position with a number of external databases was obtained to give further insight into the nature of the alert, especially where it had already been classified. External data extracted included the Transient Name Server information (TNS[1]), but also whether the alert had entries in the SIMBAD[2] (Wenger et al., 2000) or GAIA databases. If entries existed in any of these archives, the additional

Table 5.2: Summary of Hyperleda extract totals, filtered alert list (maxdet> 3, SS/PS/Gaia proximity $> 2''$) and other archive cross-correlation.

Count	Description
4812	Total galaxy count in Hyperleda extract
12116	Total count of filtered alerts
255	Total unique galaxy designations
274	Total unique ZTF objects
11598	Total unique candidate alerts
212	TNS entries from ZTF objects (4 dup)
167	TNS classified supernova entries
90	SIMBAD entries from ZTF objects (2 dup)
11	GAIA entries from ZTF objects
2	GAIA entries with a parallax

detail was added to the list of galaxy alert objects for final assessment, with the total counts again as indicated in Table 5.2.
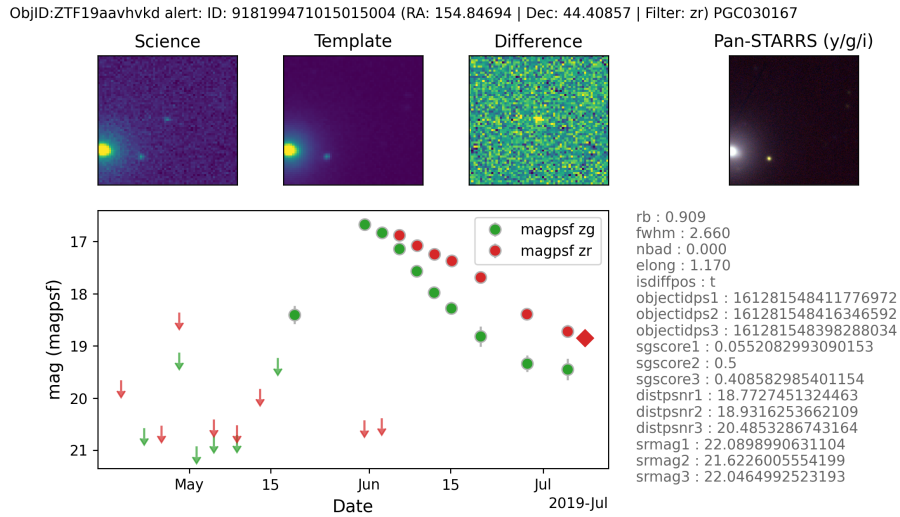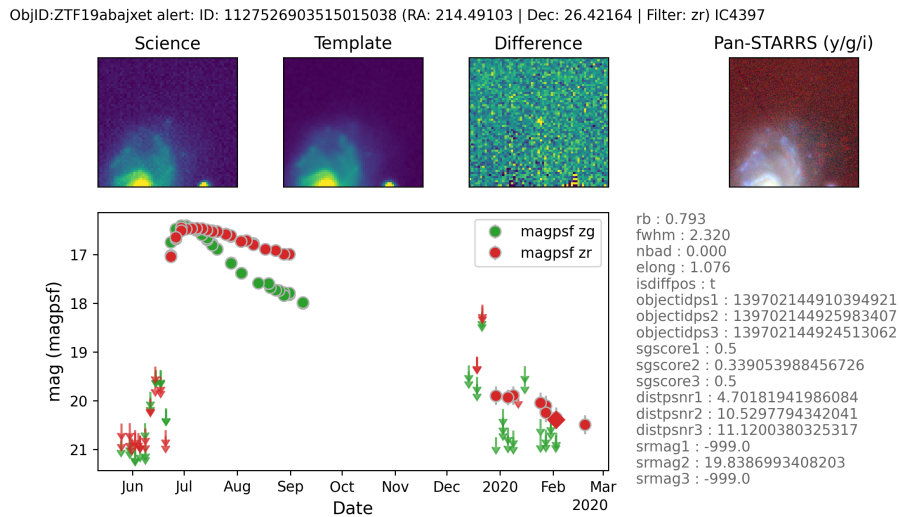
From light curves associated with alerts around galaxies searched, there was no clear evidence of TDEs. However, as summarised in Table 5.2, 212 of the 274 ZTF transient objects in the region searched had TNS entries, so it can be argued this approach is valid for the detection of optical transients. Furthermore, at the date of this report, a search of the TNS database showed 46 transients where the object type is classified as a TDE, with 28 of these credited as having been discovered through the ZTF. At ∼66 Mpc, the closest of these TDEs (Forster, 2019) was widely discussed in the popular press, and although associated with a nuclear SMBH ($\sim 1 \times 10^6$ M$_\odot$) in the face-on spiral 2MASX J04463790-1013349, the light curve from ZTF is shown in Fig. 5.3 as an example of a TDE from a BH 1 dex outside the IMBH mass range for which this project is searching. As discussed earlier §1.4, there are variables associated with both BH and disrupted star mass, along with orbital parameters of the encounter leading to a range of outcomes and profile evolution for the emissions from the event. However, to a first order we can argue that any TDEs present in the region searched would have been detected within this data.

---

[1]https://www.wis-tns.org
[2]http://simbad.cds.unistra.fr/simbad/
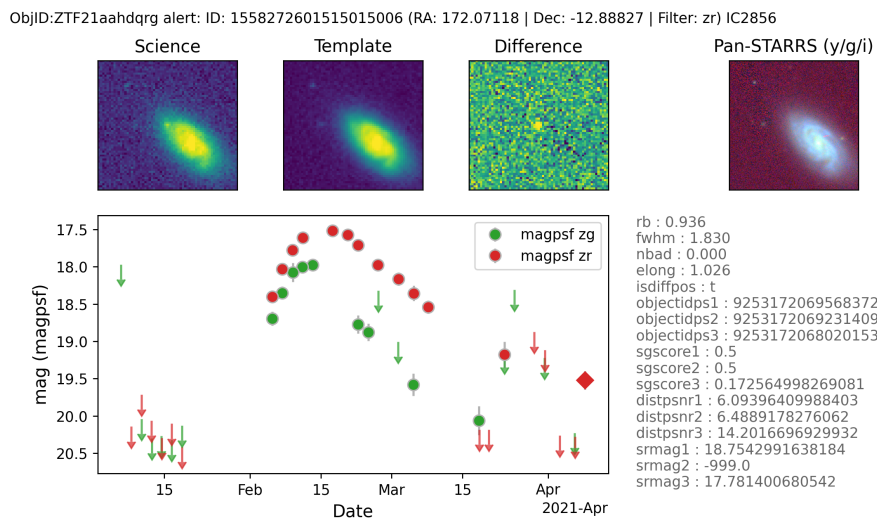
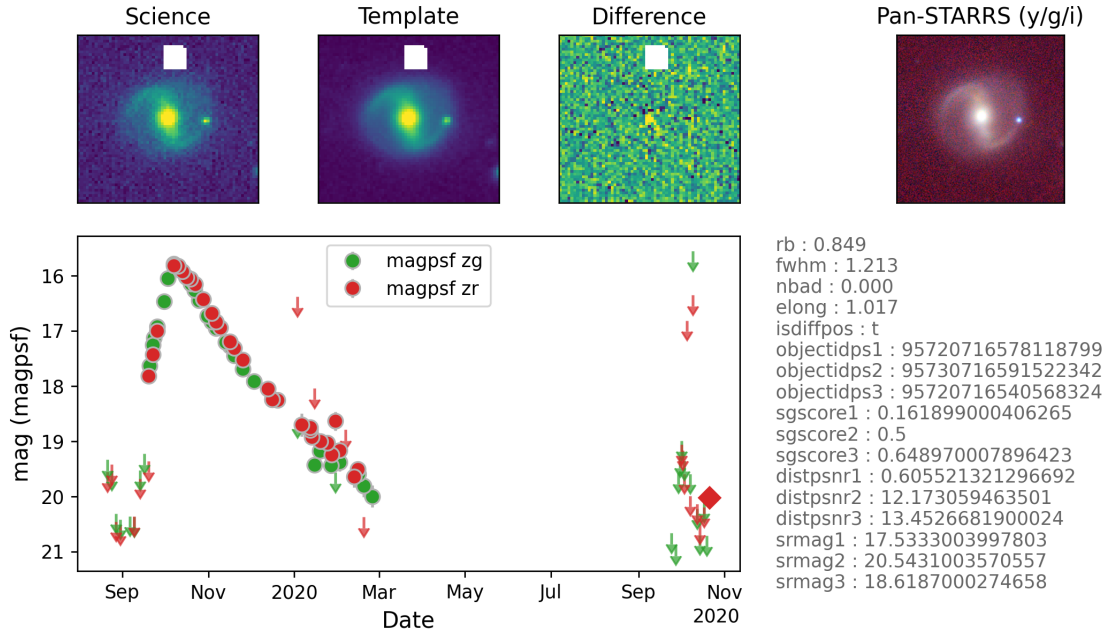**(a)** ZTF19aavhvkd - SN Type 1a in PGC 030167

(b) ZTF19abajxet - SN Type II in IC 4397

(c) ZTF21aahdqrg - SN Type Ic in IC 2856

Figure 5.2: Example SN alerts (classification from TNS) found in proximity to galaxies searched.

ObjID:ZTF19abzrhgq alert: ID: 1389351521615015004 (RA: 71.65786 | Dec: -10.22652 | Filter: zr)

Figure 5.3: Alert and light curve data from ZTF for transient object ZTF19abzrhgq. Details from the Transient Name Server classified TDE (Forster, 2019) associated with a nuclear SMBH in the face-on spiral galaxy 2MASX J04463790-1013349. The BH is estimated at $\sim 1 \times 10^6$ M$_\odot$, and the host galaxy is at a redshift of $z = 0.01513$ (Rines et al., 2003) or ~ 66 Mpc.

5.2 HST Image Analysis

Although there was no evidence of TDEs in the alert data from the galaxy proximity search, there were a number of other types of transients which, on the assumption they were associated with either GCs or CSS in the halo of the galaxies inspected, warranted further investigation. For instance, a SN transient associated with any of these objects would be of interest in its own right. Therefore, to examine the object in more detail at higher resolutions, a search was carried out to find available HST imaging at the transient positions from the HST Archive, via the MAST data source as used previously.

The resolution for much of the HST imaging is significantly better than the imaging used up to this point in the project. For example, the HST Wide-Field Camera 3 (WFC3) has a nominal quality of 0.07″ in UVIS and 0.09″ in IR. However, image pointing is inconsistent and there is no guarantee of imaging availability in the archive for any region on the sky.

In order to obtain a minimum level of quality from the HST archive image search, a level of filtering was again applied. This included preferential selection of imaging from WFC3, where the image is drizzled, has a calibration level of 3, in optical (UVIS) or IR wavelengths and is intended for use as a science image (i.e. rather than for instrument calibration). Despite these preferences, the nature of HST imaging is such that the source catalogue often only has Wide-field Planetary Camera 2 (WFPC2) or Advanced Camera for Surveys (ACS/WFC) imaging available, and this imaging was extracted for a source if necessary. Of the 274 ZTF alert objects, 64 returned HST imaging of some sort, with 38 of these images being associated with transients already classified in the TNS database and the remaining 26 had no previous classification.

The 64 HST images returned were inspected visually in conjunction with the
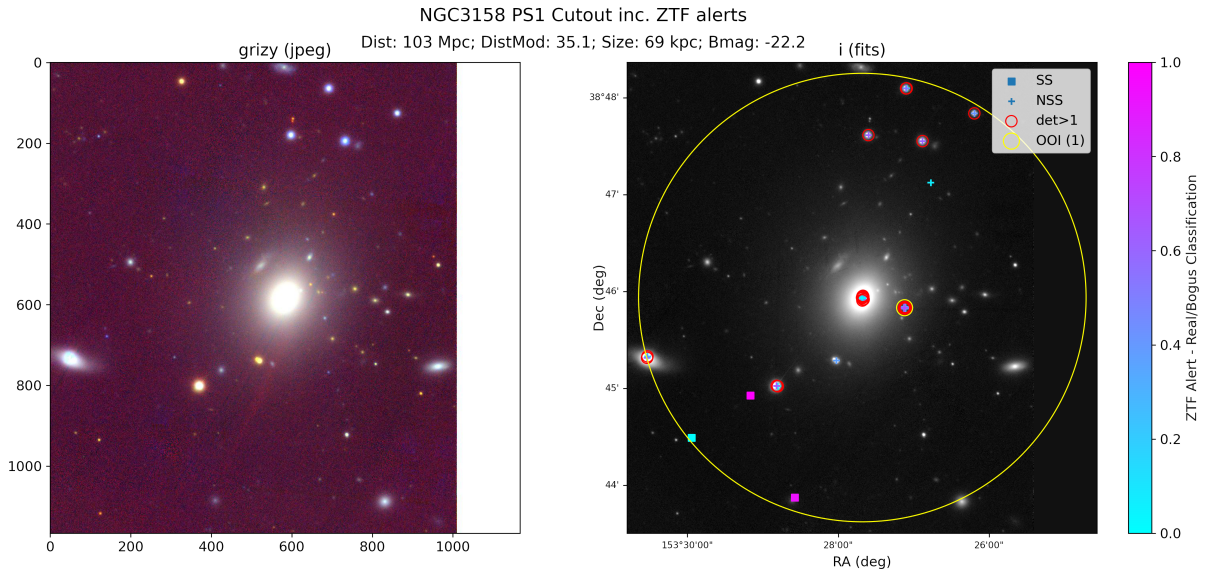
(a) PanSTARRS imaging of NGC3158 with alert positions overlaid. Alert detections shown with a red circle. Objects of interest (OOI) shown with a yellow circle, are alerts on which object filtering has been carried out (see text and Table 5.1).
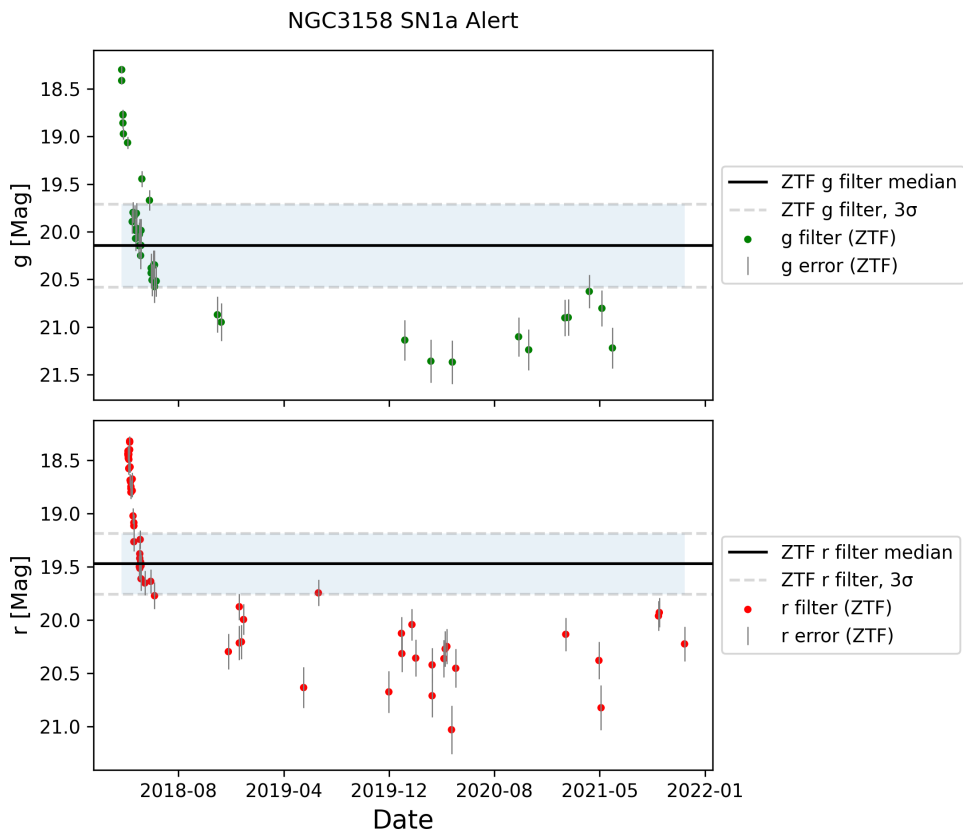

(b) Light curve for SN1a alert in proximity to NGC3158, showing profile with peak March 2018. Detection was made during a SN focused survey shortly after commissioning of the ZTF.

Figure 5.4: Image analysis of alert in proximity to NGC3158 - (a) PS1 image with alert overlay and (b) light curve of ZTF object at alert position.
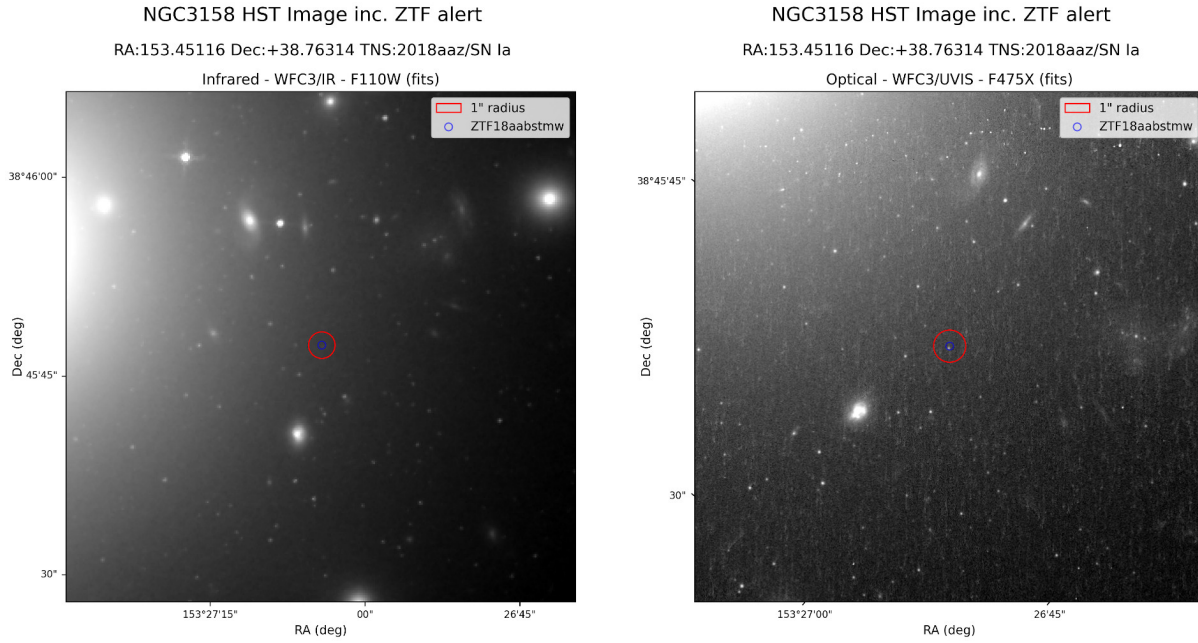
(a) Raw HST images extracted at position of alert ZTF18aabstmw. WFC3/IR and UVIS images shown in F110W (left) and F475X (right) filters respectively. This alert was classified as a type 1a SN (TNS 2018aaz).
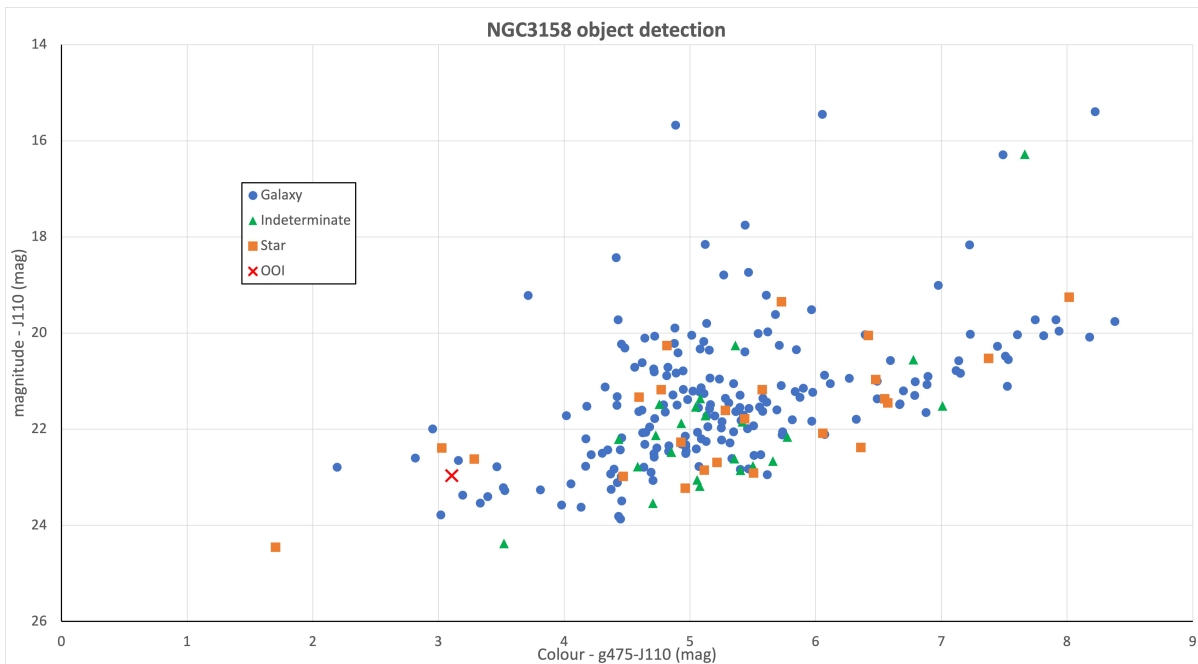
(b) Colour magnitude diagram of objects in proximity to NGC3158. Object magnitudes estimated from photometry for source objects extracted using the Skycat/GAIA tool. Galaxy and star are based on the extraction algorithm star classification (in f475x) where $Galaxy = class\_star < 0.3$ (blue circles), $Star = class\_star > 0.7$ (orange squares), intermediate values marked as $Indeterminate$ (green triangles). The locus of alert ZTF18aabstmw is shown with a red cross. The colour of this object is blue in comparison to the other objects extracted, indicating it is unlikely to be a CSS and more likely to be residual light from the SN.

Figure 5.5: Image analysis of alert in proximity to NGC3158. (a) Raw HST imaging. (b) Colour magnitude diagram for source extracted objects.

PanSTARRS imaging, light curve profiles and alerts data where available. The majority of HST images contained no significant additional detail on the alert, insomuch as the improved resolution of the imaging showed no objects at the alert position. Despite filtering for drizzled and high calibration images, there was more evidence of cosmic ray noise than expected. In certain cases, flipping between multi-epoch imaging, where available could be used to discount suspect objects within the radius of the alert.

One object of interest which arose, was a SN within proximity of NGC3158, an early-type galaxy located at a luminosity distance of ~103 Mpc. A type 1a SN (TNS SN2018aaz) occurred in proximity to this galaxy in March 2018, located as indicated in the PanSTARRS image in Fig. 5.4a, by the object of interest (OOI) tag. This alert was detected in an initial SN survey carried out by ZTF after its commissioning. The light curve for the ZTF alert object associated with this position (ZTF18aabstmw), is shown in Fig. 5.4b. The HST WFC3/IR and UVIS imaging of the same region centred on the alert position, is shown in the next figure Fig. 5.5a, where an object can be identified, especially in the UVIS/F475X image.

Using the HST images in Fig. 5.5a, source extraction and photometry was carried out using the Skycat/GAIA[3] tool. The zero points (ZP) for the instrument/filter configuration for HST were calculated in the ABmag photometric system using the STSynphot python package. At the date of the HST observation (MJD 58537 - 23 Feb 2019) the ABmag ZP for WFC3/UVIS2/F475X was 26.132 mag and WFC3/IR/F110W was 26.816 mag. These values were used in the configuration of the Skycat/GAIA tool, from which object detection and magnitude lists were determined. Each object in the list was then matched using the Starlink/Topcat[4] package, with a maximum separation of 0.5″. Having matched the source positions, a colour-magnitude diagram (CMD) of the dataset was produced, shown in Fig. 5.5b. The purpose of this was to determine the colour of the alert object, which was very much on the blue side of the source object detections. If this was a GC it would likely be as red, or redder than, the rest of the detected population hosted around NGC3158, and as this is not the case, an alternative hypothesis is that this is the residual light from the SN itself, which would conceivably be bluer.

To confirm visibility limits, additional analysis was performed to estimate a number of aspects of this SN in the environment around NGC3158. For example, although there is diversity in the luminosity of type 1a SN, Hillebrandt & Niemeyer (2000) quote an absolute visual magnitude of ~ -19.3 mag. At the distance for NGC3158, this would give an apparent magnitude $m_v = 20.76$ mag. Clearly there is some discrepancy here as the light-curve in Fig. 5.4b indicates a $m_g < 18.5$ mag. This is possibly due to the surface brightness of the background, or indicative that this is a foreground star. Nevertheless, we can take this further by assuming the light curve is generated through the radioactive decay sequence ^{56}Ni $\rightarrow^{56}$ Co $\rightarrow^{56}$ Fe (e.g., Kirshner, 1990; Hillebrandt & Niemeyer, 2000). Following this process, the light curve decay for the first 2-4 weeks is determined by the decay of ^{56}Ni with a half-life of 6.1 days, giving a reduction of ~ 0.087 mag/day for 4 weeks. After this the decay is shallower through the decay of ^{56}Co with a half-life ~77 days, giving a reduction of ~ 0.015 mag/day. As the data of the HST observation is ~11 months after the peak of the SN, we can estimate the reduction in magnitude after about 330 days as ≈ 7 mag. From the peak above, estimated from the light curve at $m_{g,peak} \sim 18.3$ mag, this equates to a magnitude after 330 days of $m_{g,330} \sim 25.3$ mag,

---

[3]GAIA - Graphical Astronomy and Image Analysis http://star-www.dur.ac.uk/~pdraper/gaia/gaia.htx/index.html

[4]TOPCAT - Tool for OPerations on Catalogues And Tables http://www.starlink.ac.uk/topcat/

which correlates roughly with the estimated GAIA tool photometry for the object of 26.1 mag.

The exposure time of the HST imaging in Fig. 5.5a was 2612s (Jensen et al., 2021), which for the WFC3/UVIS instrument, through the F475X filter gives a limiting magnitude (with a S/N ~10) of $m_{\text{F475X,AB}} \sim 27.5$mag (Dressel, 2021, Figure A.56). This implies that the residual light from the decaying SN would still have been visible at the point at which the observation was made, further suggesting that this is unlikely to be a GC, but rather the light from the SN itself.

In this chapter we have used ZTF alert data in conjunction with galaxy catalogue information to search for evidence of TDEs in environments which are thought to support IMBH in dense stellar cores. Despite many transient alerts being raised, analysis of the associated light curves showed no indications these were related to disruption events. The implication of this is discussed in Chapter 6.

Chapter 6

Discussion

As detailed in the analysis and result from Chapters 3 to 5, no TDEs were evident in either the light curves or alert searches at the known CSS positions, or the more general search in proximity to galaxies out to 120 Mpc.

Original theoretical predictions of TDE rates, albeit generally for SMBH and solar mass stars, were quoted at about $n_{\text{TDE}} \approx 10^{-4}\text{yr}^{-1}\text{gal}^{-1}$, e.g. Frank & Rees (1976); Ulmer (1999). However, as Stone & Metzger (2016) note, more recent observational results have suggested an order of magnitude lower rate than this at $n_{\text{TDE}} \approx 10^{-5}\text{yr}^{-1}\text{gal}^{-1}$. On the other hand, as this rate is a sensitive function of the central density profile of the galaxy, Wang & Merritt (2004) suggested that for systems such as nucleated dwarfs, where the nuclear density profile is steep, the rate may be an order of magnitude higher at $n_{\text{TDE}} \approx 10^{-3}\text{yr}^{-1}\text{gal}^{-1}$. This latter case is particularly relevant for the composite population of CSS, and it will therefore be informative to compare the above literature rates with an upper limit based on our non-detection of TDEs.

The period of data sampling, t_{ZTF}, for both the ZTF light curve reference objects, and the alert pipeline was taken to be March 2018 to September 2021 or 42 months (3.5 yrs) in total.

From the first and second approaches performed, searching at the position of known CSS, the number of CSS which had confirmed ZTF reference objects associated as $n_{\text{CSS}} = 1072$. This value is used as although 1484 objects were in the data, many were excluded due to their lower declination, and despite a professed limit of $\delta = -30°$ the lowest declination reference object related CSS was HUCD2 in Hydra I with a declination of $\delta = -27°26'6''$. In fact, only 3 objects were found with a declination lower than $\delta = -15°$. This is likely due to increased seeing and limiting magnitude at the low elevations required to image objects at these declination's reliably throughout a season, and the requirement for a minimum of 20 'good' images to co-add for a reference image.

Nevertheless, using this data gives an upper limit for the TDE rate in CSS of

$$n_{\text{TDE,Max}} < \frac{1}{n_{\text{CSS}} \times t_{\text{ZTF}}} \lessapprox 2.7 \times 10^{-4}\text{yr}^{-1}\text{gal}^{-1} \tag{6.1}$$

which is slightly below the highest literature rate for TDEs which assume a steep nuclear density profile, but higher than the standard theoretical TDE rate. In essence, it is marginal at best that no TDEs were found in this data sample. If the sample could be increased, either by the addition of further discovered CSS objects and/or by extending the sampling period, this would improve the reliability of the result. For example, if the period of inspection could be extended to 10 years, and still no TDEs were observed in

this CSS sample, this would start to bring into question the validity of the theoretical limit for CSS type objects.

The final approach, using a different dataset, gave 4812 galaxies within the sample, but of more relevance is the number of clusters associated with the halos of these galaxies. As shown in Eq. (2.2), this was calculated from the globular cluster luminosity function (GCLF) and specific frequency of GCs per unit galaxy luminosity as $n_{\text{GC,Total}} \approx 3.8 \times 10^6$. Clearly this is a larger sample, and if we assume firstly that this includes CSS at the top end of the GCLF, and secondly that GCs themselves may also harbour nuclear IMBH, this then gives rise to an upper limit on TDEs in galaxy halos

$$n_{\text{TDE,Max}} < \frac{1}{n_{\text{GC,Total}} \times t_{\text{ZTF}}} \lessapprox 7.5 \times 10^{-8} \text{yr}^{-1} \text{gal}^{-1} \qquad (6.2)$$

which is significantly at odds with even the lowest predicted TDE rates. However, for our purposes we have sanitised this sample by estimating the count of GCs which, based on the GCLF, should statistically be visible in our PanSTARRS *g*-filter follow-up imaging (limiting magnitude 22 mag). As detailed in Chapter 5, and Eq. (2.6) this reduces the overall count of potential objects to $n_{\text{GC,Vis}} \approx 1.9 \times 10^5$, or about 5% of the above total. From this we obtain a visible TDE upper limit of

$$n_{\text{TDE,Vis}} < \frac{1}{n_{\text{GC,Vis}} \times t_{\text{ZTF}}} \lessapprox 1.5 \times 10^{-6} \text{yr}^{-1} \text{gal}^{-1} \qquad (6.3)$$

which is still ~1 dex below the lowest literature detection limit. This implies either that ~10 TDEs in this sample have occurred but were undetected, or the number of TDEs predicted in our sample is erroneous.
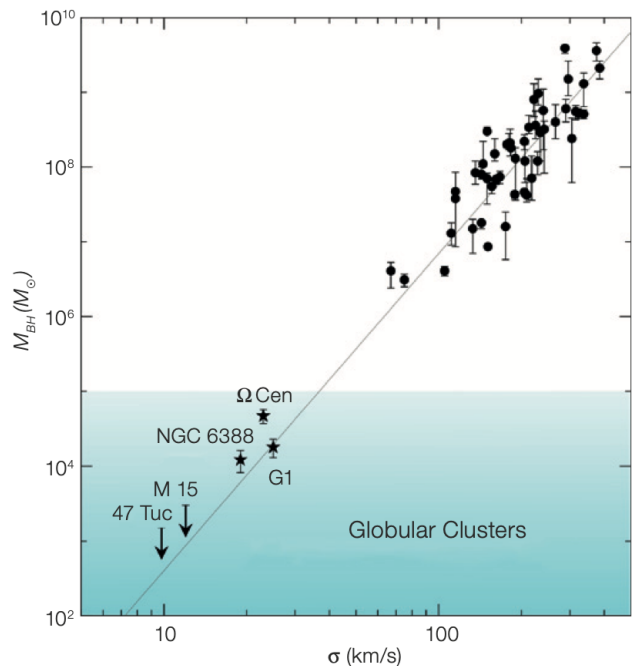
Despite attempting to ensure object visibility, in the former case it is possible that non-detections may occur if the immediate vicinity around the BH is optically thick. However, a surplus of gas and dust is at odds with the conventional view of GCs (e.g. Bastian & Strader, 2014; Cabrera-Ziri et al., 2015), as excess material is generally considered to have been used or ejected from these aged systems during their original star formation episodes. Conversely, for CSS formed through tidal stripping, more gas and dust may be present in the core due to inflows after interaction of the progenitor with a larger galaxy (e.g. Janz et al., 2016). It may also be possible that a thick disc, when presented edge-on, would be sufficient to absorb optical emissions, although in the case of this sample, an average 'funnel' angle on the central torus of $\geqslant 18°$ should, statistically, have given rise to one detection as this would have allowed visibility of the inner disc (see Fig. 1.5 and Dai et al. (2018)). While this may have provided a view of accretion emissions, reprocessing to optical may be marginal with this geometry, resulting in TDEs predominantly emitting in X-ray or UV, not covered by this project. A future cross-correlation in other wavelengths would be interesting to explore this avenue. Nevertheless, it should be remembered that quiescence is one of the (many) reasons detection of putative BHs in GCs is not trivial, and the mechanics behind the formation of an accretion disc as a result of a tidal encounter has many parameters. As discussed in §1.4, these include BH mass and rotation, star density, and orbital velocity, ellipticity and periapsis, all of which may affect the nature of the tidal stream, the matter fallback rate and ultimately the nature of the accretion disc which forms.

In the latter case for our sample, where the number of TDEs expected is in some way erroneous, we should consider a number of possibilities, including that IMBH do not exist in CSS, or IMBH do exist, but the rate of TDEs in this environment is lower than for

SMBH in galaxy cores, or more generally that the TDE rate is lower than the theoretical prediction.

When considering whether IMBH exist in CSS, it is useful to split the composite population into massive clusters and galaxies which have been through tidal stripping. It has long been thought that GCs (and thus by definition, massive clusters) may harbour nuclear BH (e.g. Miller & Hamilton, 2002) and at the lower end of the CSS mass scale this view has tantalising implications. If central BHs form in clusters following a similar process to larger galaxies, then we can justify taking a simplistic perspective and extrapolate the BH mass - scaling relationships. As illustrated by Lützgendorf et al. (2012) for the $M_{BH} - M_\sigma$ relationship (see Fig. 6.1), the BH mass would be of an intermediate scale.

The validity of this assumption is questionable due to a lack of firm evidence of nuclear BH in clusters. However, many authors suggest formation of IMBH in clusters is possible through core collapse and runaway mergers of massive stars (Portegies Zwart & McMillan, 2002), or repeated merging of mass segregated BHs (Miller & Hamilton, 2002). Some numerical simulations support this, such as González et al. (2021) who carried out N-body simulations in young star clusters with low metallicities and high binary fractions finding that at least one IMBH was often formed. Conversely, other authors (e.g. Heger & Woosley, 2002; Giesler et al., 2018) show dynamical interactions in cluster cores would eject many BH from the system before mergers could occur to 'grow' a nuclear BH. Despite this, X-ray emissions seem prevalent in GCs (e.g. Strader et al., 2012a), some associated with low-mass X-ray binaries

Figure 6.1: Scaling relationship between nuclear black hole mass (M_{BH}) and core velocity dispersion (σ) showing extrapolation of relationship from galaxies hosting SMBH (circles), down to cEs (Ω Cen, G1) and a few GCs. (Credit: Lützgendorf et al., 2012)

(LMXB), i.e. stellar mass BH[1] in binary systems where a partner, overflowing its Roche lobe, is slowly subsumed via an accretion disc into the BH. Pulsars also appear to be common in GCs (e.g. Devecchi et al., 2007) and thus an excess of dynamical mass, as indicated by the central velocity dispersion, compared to the luminous mass might simply be explained by a population of core segregated stellar mass BH and neutron stars rather than a single nuclear IMBH. Several examples exist of observational evidence fitting both scenarios (see Vitral & Mamon, 2021, for a recent example), but in this respect Occam's Razor would suggest there is no need to invoke the presence of IMBH, without evidence to the contrary.

---

[1]Most LMXBs in GCs are associated with neutron stars, but techniques such as radial velocity measurements through soft X-ray output (Charles, 2011), or X-ray / radio correlation (Bahramian et al., 2017) can be used to determine the system mass function, and thus the probability the compact object is a neutron star or BH.

At the upper end of the CSS mass scale, where we consider UCDs formed through tidal stripping encounters or cEs formed as low-mass galaxies (e.g. dwarf ellipticals) or tidally stripped bulges, the masses of the BHs are expected to be larger (an example is the Ω Cen shown in Fig. 6.1, the largest GC in the Milky Way and thought to be the core remnant of a dwarf galaxy). Certainly bulges and cores remaining, after tidal threshing has removed less gravitationally bound peripheral material, would have a nuclear BH mass related to the progenitor, and thus higher than would be expected for the remnant cluster mass. This is one of the significant 'observable' differentiators of CSS formation in the overlapping population, and is just one example of core phenomenological parameters which remain largely unaffected by a threshing event. As such there is no reason to expect there to be fewer TDEs in this type of environment than the galactic cores for which the theoretical rate has been calculated.

The implication here is that the ratio of large clusters to small / stripped galaxies would be another factor in respect of expected TDE rate and thus detection in our sample. Although the completeness of the CSS catalogue sample is unclear, of the 1484 in the non-local cut, 301 objects had estimated mass $M_\star > 7 \times 10^7$ M$_\odot$, i.e. over the cluster formation threshold mass (see §1.1) and thus would have a higher probability of having originally formed as dwarf galaxies or bulges, but been subsequently stripped through a threshing episode. If we apply the same ratio, conservatively taking 1/10th of our cluster sample (Eq. (6.3)) which was already reduced by 2 dex to encompass a high luminosity tail, this brings us to the equivalent of the lowest order of TDE rate, $n_{\text{TDE}} \approx 10^{-5} \text{yr}^{-1} \text{gal}^{-1}$. Although marginal, this suggests our extragalactic periphery sample should have detected ~1 TDE if the low rate is appropriate for GCs, but more importantly the higher rates (theoretical and for steep nuclear density objects) are not appropriate for these systems.

Chapter 7

Conclusions

In this project, we have taken two separate data sets, and applied them to a search for tidal disruption events (TDEs), to provide evidence for the existence of intermediate-mass black holes (IMBH). The search was performed primarily on the optical archives of the Zwicky Transient facility (ZTF), using light curves and alerts produced by the facility. Follow-up and contextual imaging were also carried out using PanSTARRS and HST archives. The data sets were based on compact stellar system (CSS) positions, covering the mass / radius space from globular clusters through to dwarf elliptical galaxies, with one data set consolidated from literature CSS positions, and the other from notional CSS populations hosted around massive galaxies at distance $2 \leqslant D \leqslant 120$ Mpc.

We discussed the nature of CSS, especially considering the low-mass cluster, or ultra-compact dwarf (UCD), end of what is considered a composite population, with the expectation any TDEs observed would involve IMBH and WD. The larger mass systems, nominally referred to as compact ellipticals (cEs), derived from tidally threshed larger galaxies, are more likely to host IMBH of higher mass, or even super-massive black holes (SMBH). No strong evidence was found to preclude TDEs in these systems.

Despite analysis of the archives covering a period of approximately 42 months, no evidence of optical TDE transient signatures was found through either inspection of light curves and transient alerts at known CSS positions, or alerts in the periphery of our host galaxies sample. From this result we conclude that the upper limit for the rate of TDEs in CSS is $n_{\mathrm{TDE,Vis}} \lessapprox 10^{-6} \mathrm{yr}^{-1} \mathrm{gal}^{-1}$ which is two orders of magnitude below the theoretical TDE rate involving SMBH interacting with solar mass main sequence stars in the nucleus of massive galaxies.

In conclusion, however, we recognise that further analysis and data would be required to determine a lower limit for TDEs in the dense stellar environments of CSS, in addition to their potential visibility using current detection methods. This would be essential to lead to an understanding of the nature of the discrepancy between the TDE rates discussed in literature and the upper limit found in this project. For example, N-body simulations with realistic GC stellar mass functions could improve predictions of the frequency of encounters between WD or remaining lower-mass MS stars and a nuclear IMBH. Simulations of this type could also allow clarification of the significance of other factors regarding the visibility of these events, or more accurately, the probability of detecting them using specific methods. For example, this would include the frequency with which a WD would be swallowed whole, i.e. without disruption or flaring, and the spectrum, luminosity and longevity of the flare, which would determine the limiting magnitude and observing cadence necessary under varying scenarios.

Further work

The selection of a single, albeit capable, facility for this project, was a conscious decision, as the author was keen to prove the viability of the approach taken and to concentrate on the scientific aspects of the study with a homogeneous sample. Therefore, increasing the size of the sample, to improve the probability of detecting a TDE, could be achieved in a number of ways. This would include increasing the coverage of the sample, both spatially and temporally. While the ZTF is active, repeating the detailed analysis over a longer period of time could be carried out most easily to increase the 4D coverage of the sample. Increasing the surveyed area, especially including southern hemisphere data ($\delta \leqslant -30°$), using additional facilities such as those discussed in §2.2, would also be possible, but by no means trivial as consolidating results may be problematic. For example removing duplicates where coverage for different facilities overlap and assessing the depth and time sensitivity of the individual surveys through the limiting magnitude and cadence respectively.

A similar project could be carried out to a greater depth and cadence, thereby increasing the volume searched and also largely following the ZTF processing model, after the Vera C. Rubin observatory (previously the Large Synoptic Survey Telescope or LSST), is commissioned. As shown in Fig. 2.5, this facility will provide 2 orders of magnitude better 'grasp' (volume/time) across a larger range of optical / IR wavelengths, and as this telescope is based in Chile, southern hemisphere coverage will also add to the volume surveyed. Consolidation of LSST data with the existing ZTF data should provide a relatively straightforward increase in both volume and time period sample.

Performing a similar analysis in other wavelengths, especially X-ray and UV, where TDEs are expected to be more luminous, may provide the benefit of increasing the probability of detection, although for example, even the eROSITA satellite, which started operation in Dec 2019, will only provide 6 month all-sky cadence over its 4 year mission period.

Further development of the analysis process may also be beneficial. For example, filtering of noise by co-addition of nightly imaging, sample binning or rolling average. Also the use of aperture photometry to reduce the impact of host galaxy proximity (i.e. background surface brightness) and allow inclusion of closer objects of larger angular size. Finally, it would be possible to develop algorithms to test the cointegration of signals between different filters.

As mentioned earlier, while follow up of ZTF detected TDEs are routinely carried out on the Palomar 60" to provide insight into the spectroscopic nature of the event, detailed, high-resolution follow up of all TDE events to categorise the nature of their location and surrounding stellar environment, for example by HST, has not been carried out consistently. A homogeneous follow up of the ∼100 known TDE positions, would provide this environmental background, allowing potential similarities in the stellar population demographics to be identified.

Bibliography

Abbott B. P., et al., 2016, Phys. Rev. Lett., 116, 241102

Abbott R., et al., 2020, Phys. Rev. Lett., 125, 101102

Abramowicz M. A., Fragile P. C., 2013, Living Reviews in Relativity, 16, 1

Abramowicz M. A., Czerny B., Lasota J. P., Szuszkiewicz E., 1988, ApJ, 332, 646

Akeson R., et al., 2019, arXiv e-prints, p. arXiv:1902.05569

Andreoni I., Cooke J., 2019, in Griffin R. E., ed., Proceedings of the International Astronomical Union Vol. 339, Southern Horizons in Time-Domain Astronomy. pp 135–138 (arXiv:1802.01100), doi:10.1017/S1743921318002399

Astropy Collaboration et al., 2013, A&A, 558, A33

Astropy Collaboration et al., 2018, AJ, 156, 123

Ata M., et al., 2018, MNRAS, 473, 4773

Atwood W. B., et al., 2009, ApJ, 697, 1071

Bañados E., et al., 2018, Nature, 553, 473

Bahramian A., et al., 2017, MNRAS, 467, 2199

Baker J., et al., 2019, arXiv e-prints, p. arXiv:1907.06482

Bakos G. Á., 2018, The HATNet and HATSouth Exoplanet Surveys. Springer International Publishing AG, p. 111, doi:10.1007/978-3-319-55333-7_111

Bastian N., Strader J., 2014, MNRAS, 443, 3594

Bekki K., Couch W. J., Drinkwater M. J., 2001, ApJL, 552, L105

Bellm E. C., 2019, in Griffin R. E., ed., Proceedings of the International Astronomical Union Vol. 339, Southern Horizons in Time-Domain Astronomy. pp 160–164 (arXiv:1802.10218), doi:10.1017/S174392131800248X

Bellm E. C., et al., 2019a, PASP, 131, 018002

Bellm E. C., et al., 2019b, PASP, 131, 068003

Binggeli B., Sandage A., Tammann G. A., 1985, AJ, 90, 1681

Blagorodnova N., et al., 2018, PASP, 130, 035003

Bonnerot C., Rossi E. M., Lodato G., 2016, MNRAS, 458, 3324

Bowyer S., Byram E. T., Chubb T. A., Friedman H., 1965, Science, 147, 394

Bromm V., Loeb A., 2003, ApJ, 596, 34

Brown T. M., et al., 2013, PASP, 125, 1031

Burbidge E. M., Burbidge G. R., Fish R. A., 1961, ApJ, 133, 393

Cabrera-Ziri I., et al., 2015, MNRAS, 448, 2224

Cappellari M., et al., 2011, MNRAS, 413, 813

Chambers K. C., et al., 2016, arXiv e-prints, p. arXiv:1612.05560

Charles P., 2011, in Schmidtobreick L., Schreiber M. R., Tappert C., eds, Astronomical Society of the Pacific Conference Series Vol. 447, Evolution of Compact Binaries. p. 19

Cheng H., Yuan W., Liu H.-Y., Breeveld A. A., Jin C., Liu B., 2019, MNRAS, 487, 3884

Chiboucas K., et al., 2011, ApJ, 737, 86

Chilingarian I., Zolotukhin I., 2015, Science, 348, 418

Chilingarian I., Cayatte V., Revaz Y., Dodonov S., Durand D., Durret F., Micol A., Slezak E., 2009, Science, 326, 1379

Clark D., Stephenson F., 2013, The Historical Supernovae. Pergamon international library of science, technology, engineering, and social studies, Elsevier Science, https://books.google.co.uk/books?id=qodGBQAAQBAJ

DES Collab. 2005, arXiv e-prints, pp astro–ph/0510346

DES Collab. et al., 2016, MNRAS, 460, 1270

Da Rocha C., Mieske S., Georgiev I. Y., Hilker M., Ziegler B. L., Mendes de Oliveira C., 2011, A&A, 525, A86

Dai L., McKinney J. C., Roth N., Ramirez-Ruiz E., Miller M. C., 2018, ApJL, 859, L20

Dekany R., et al., 2020, PASP, 132, 038001

Devecchi B., Colpi M., Mapelli M., Possenti A., 2007, MNRAS, 380, 691

Dewdney P. E., Hall P. J., Schilizzi R. T., Lazio T. J. L. W., 2009, IEEE Proceedings, 97, 1482

Djorgovski S. G., et al., 2011, arXiv e-prints, p. arXiv:1102.5004

Djorgovski S. G., Mahabal A., Drake A., Graham M., Donalek C., 2013, Sky Surveys. Springer Science & Business Media, Dordrecht, p. 223, doi:10.1007/978-94-007-5618-2_5

Drake A. J., et al., 2009, ApJ, 696, 870

Dressel L., 2021, in , Vol. 13, WFC3 Instrument Handbook for Cycle 29 v. 13. STScI, Baltimore, p. 13

Drinkwater M. J., Jones J. B., Gregg M. D., Phillipps S., 2000, , 17, 227

Duev D. A., et al., 2019, MNRAS, 489, 3582

Einstein A., 1916, Annalen der Physik, 354, 769

Emerson J., McPherson A., Sutherland W., 2006, The Messenger, 126, 41

Evans C. R., Kochanek C. S., 1989, ApJL, 346, L13

Faber S. M., 1973, ApJ, 179, 423

Ferrarese L., Merritt D., 2000, ApJL, 539, L9

Ferrarese L., et al., 2006, ApJS, 164, 334

Ferré-Mateu A., Forbes D. A., Romanowsky A. J., Janz J., Dixon C., 2018, MNRAS, 473, 1819

Forbes D. A., Pota V., Usher C., Strader J., Romanowsky A. J., Brodie J. P., Arnold J. A., Spitler L. R., 2013, MNRAS, 435, L6

Forbes D. A., Norris M. A., Strader J., Romanowsky A. J., Pota V., Kannappan S. J., Brodie J. P., Huxor A., 2014, MNRAS, 444, 2993

Forster F., 2019, Transient Name Server Discovery Report, 2019-1857, 1

Frank J., Rees M. J., 1976, MNRAS, 176, 633

Frieman J. A., et al., 2008, AJ, 135, 338

Gaia Collab. et al., 2016, A&A, 595, A1

Gaia Collab. et al., 2018, A&A, 616, A1

Gehrels N., Cannizzo J. K., 2015, Journal of High Energy Astrophysics, 7, 2

Gehrels N., et al., 2004, ApJ, 611, 1005

Gezari S., 2021, ARA&A, 59

Giesler M., Clausen D., Ott C. D., 2018, MNRAS, 477, 1853

Gingerich O., 2005, in Turatto M., Benetti S., Zampieri L., Shea W., eds, Astronomical Society of the Pacific Conference Series Vol. 342, 1604-2004: Supernovae as Cosmological Lighthouses. p. 3

Ginsburg A., et al., 2019, AJ, 157, 98

González E., Kremer K., Chatterjee S., Fragione G., Rodriguez C. L., Weatherford N. C., Ye C. S., Rasio F. A., 2021, ApJL, 908, L29

Graham A. W., 2002, ApJL, 568, L13

Graham A. W., Driver S. P., 2007, ApJ, 655, 77

Graham M. J., et al., 2019, PASP, 131, 078001

Greene J. E., Strader J., Ho L. C., 2020, ARA&A, 58, 257

Grindlay J., Tang S., Simcoe R., Laycock S., Los E., Mink D., Doane A., Champine G., 2009, in Osborn W., Robbins L., eds, Astronomical Society of the Pacific Conference Series Vol. 410, Preserving Astronomy's Photographic Legacy: Current State and the Future of North American Astronomical Plates. p. 101

Guérou A., et al., 2015, ApJ, 804, 70

Guillochon J., Ramirez-Ruiz E., 2013, ApJ, 767, 25

Guillochon J., Ramirez-Ruiz E., 2015, ApJ, 809, 166

Haas R., Shcherbakov R. V., Bode T., Laguna P., 2012, ApJ, 749, 117

Harris W. E., van den Bergh S., 1981, AJ, 86, 1627

Harris C. R., et al., 2020, Nature, 585, 357

Hau G. K. T., Spitler L. R., Forbes D. A., Proctor R. N., Strader J., Mendel J. T., Brodie J. P., Harris W. E., 2009, MNRAS, 394, L97

Heger A., Woosley S. E., 2002, ApJ, 567, 532

Hilker M., Infante L., Vieira G., Kissler-Patig M., Richtler T., 1999, A&AS, 134, 75

Hillebrandt W., Niemeyer J. C., 2000, ARA&A, 38, 191

Hills J. G., 1975, Nature, 254, 295

Hoskin M., 1999, The Cambridge Concise History of Astronomy. Cambridge University Press, Cambridge CB2 2RU. UK.

Hunter J. D., 2007, Computing in Science and Engineering, 9, 90

Ivezić Ž., et al., 2007, AJ, 134, 973

Ivezić Ž., et al., 2019, ApJ, 873, 111

Janz J., et al., 2016, MNRAS, 456, 617

Jensen J. B., et al., 2021, ApJS, 255, 21

Jones J. B., et al., 2006, AJ, 131, 312

Jordán A., et al., 2007, ApJS, 171, 101

Kaspi S., Smith P. S., Netzer H., Maoz D., Jannuzi B. T., Giveon U., 2000, ApJ, 533, 631

King I., 1961, ApJ, 134, 272

Kirshner R., 1990, Supernovae. Springer-Verlag Berlin Heidelberg New York

Kochanek C. S., et al., 2017, PASP, 129, 104502

Kormendy J., Ho L. C., 2013, ARA&A, 51, 511

Kormendy J., Richstone D., 1995, ARA&A, 33, 581

Kormendy J., Fisher D. B., Cornell M. E., Bender R., 2009, ApJS, 182, 216

Krolik J. H., Piran T., 2011, ApJ, 743, 134

Kulkarni S. R., 2012, arXiv e-prints, p. arXiv:1202.2381

Kulkarni S. R., 2013, The Astronomer's Telegram, 4807, 1

LIGO Scientific Collaboration et al., 2015, Classical and Quantum Gravity, 32, 074001

Larson R. B., 2003, Reports on Progress in Physics, 66, 1651

Law N. M., et al., 2009, PASP, 121, 1395

Lawrence A., et al., 2007, MNRAS, 379, 1599

Lee M. G., Jang I. S., 2016, ApJ, 831, 108

Lin D., et al., 2018, Nature Astronomy, 2, 656

Lodato G., Rossi E. M., 2011, MNRAS, 410, 359

Lodato G., King A. R., Pringle J. E., 2009, MNRAS, 392, 332

Lützgendorf N., et al., 2012, The Messenger, 147, 21

MacLeod M., Goldstein J., Ramirez-Ruiz E., Guillochon J., Samsing J., 2014, ApJ, 794, 9

Maddison R., 1997, Journal of the Antique Telescope Society, 13, 4

Magnier E. A., et al., 2020, ApJS, 251, 6

Mahabal A., et al., 2019, PASP, 131, 038002

Makarov D., Prugniel P., Terekhova N., Courtois H., Vauglin I., 2014, A&A, 570, A13

Malyali A., Rau A., Nandra K., 2019, MNRAS, 489, 5413

Mamajek E. E., et al., 2015, arXiv e-prints, p. arXiv:1510.06262

Martin D. C., et al., 2005, ApJL, 619, L1

Masci F. J., et al., 2017, PASP, 129, 014002

Masci F. J., et al., 2019, PASP, 131, 018003

Merloni A., Heinz S., di Matteo T., 2003, MNRAS, 345, 1057

Mezcua M., 2017, International Journal of Modern Physics D, 26, 1730021

Mieske S., Hilker M., Jordán A., Infante L., Kissler-Patig M., 2007, A&A, 472, 111

Miller M. C., Hamilton D. P., 2002, MNRAS, 330, 232

Minkowski R. L., Abell G. O., 1963, The National Geographic Society-Palomar Observatory
    Sky Survey. University of Chicago Press, Chicago, IL. USA., p. 481

Misgeld I., Hilker M., Mieske S., 2009, A&A, 496, 683

Misgeld I., Mieske S., Hilker M., Richtler T., Georgiev I. Y., Schuberth Y., 2011, A&A, 531, A4

Mortlock D. J., et al., 2011, Nature, 474, 616

Munoz-Arancibia A., et al., 2021, Transient Name Server Discovery Report, 2021-1444, 1

Murakami H., et al., 2007, PASJ, 59, S369

Narayan R., McClintock J. E., 2008, , 51, 733

Narayan R., Yi I., 1994, ApJL, 428, L13

Nieto J. L., Prugniel P., 1987, A&A, 186, 30

Norris M. A., Kannappan S. J., 2011, MNRAS, 414, 739

Norris M. A., et al., 2014, MNRAS, 443, 1151

Norris M. A., Escudero C. G., Faifer F. R., Kannappan S. J., Forte J. C., van den Bosch R. C. E., 2015, MNRAS, 451, 3615

Nousek J. A., Gehrels N., Burrows D. N., Kennea J., Hartmann D., 2011, in AAS/High Energy Astrophysics Division #12. p. 36.18

Ofek E. O., Ben-Ami S., 2020, PASP, 132, 125004

Paczyńsky B., Wiita P. J., 1980, A&A, 500, 203

Patterson M. T., et al., 2019, PASP, 131, 018001

Paudel S., Lisker T., Hansson K. S. A., Huxor A. P., 2014, MNRAS, 443, 446

Peng E. W., et al., 2008, ApJ, 681, 197

Pennington R. L., Humphreys R. M., Odewahn S. C., Zumach W., Thurmes P. M., 1993, PASP, 105, 521

Penny S. J., Forbes D. A., Strader J., Usher C., Brodie J. P., Romanowsky A. J., 2014, MNRAS, 439, 3808

Peterson B. M., Horne K., 2004, Astronomische Nachrichten, 325, 248

Pfeffer J., Baumgardt H., 2013, MNRAS, 433, 1997

Pfeffer J., Hilker M., Baumgardt H., Griffen B. F., 2016, MNRAS, 458, 2492

Phillipps S., Drinkwater M. J., Gregg M. D., Jones J. B., 2001, ApJ, 560, 201

Piran T., Svirski G., Krolik J., Cheng R. M., Shiokawa H., 2015, ApJ, 806, 164

Portegies Zwart S. F., McMillan S. L. W., 2002, ApJ, 576, 899

Predehl P., 2017, Astronomische Nachrichten, 338, 159

Rees M. J., 1988, Nature, 333, 523

Reid I. N., et al., 1991, PASP, 103, 661

Rey S., Kim S., Jeong H., Lee Y., Lee J., Joo S., Kim H., 2020, in American Astronomical Society Meeting Abstracts #236. p. 138.03

Rines K., Geller M. J., Kurtz M. J., Diaferio A., 2003, AJ, 126, 2152

Ruszkowski M., et al., 2019, BAAS, 51, 326

Sandoval M. A., et al., 2015, ApJL, 808, L32

Saxton R., et al., 2019, Astronomische Nachrichten, 340, 351

Schmidt M., 1963, Nature, 197, 1040

Shakura N. I., Sunyaev R. A., 1973, A&A, 500, 33

Shappee B. J., et al., 2014, ApJ, 788, 48

Siebert M. R., Strasburger E., Rojas-Bravo C., Foley R. J., 2019, Transient Name Server Classification Report, 2019-1921, 1

Skrutskie M. F., et al., 2006, AJ, 131, 1163

Smartt S. J., 2009, ARA&A, 47, 63

Smith A. M. S., WASP Consortium 2014, Contributions of the Astronomical Observatory Skalnate Pleso, 43, 500

Smith Castelli A. V., Faifer F. R., Richtler T., Bassino L. P., 2008, MNRAS, 391, 685

Smith K. W., et al., 2020, PASP, 132, 085002

Stone N. C., Metzger B. D., 2016, MNRAS, 455, 859

Strader J., Chomiuk L., Maccarone T. J., Miller-Jones J. C. A., Seth A. C., 2012a, Nature, 490, 71

Strader J., et al., 2012b, ApJ, 760, 87

Strausbaugh R., Cucchiara A., Dow Michael J., Webb S., Zhang J., Goode S., Cooke J., 2021, arXiv e-prints, p. arXiv:2109.13203

Strubbe L. E., Murray N., 2015, MNRAS, 454, 2321

Taylor M. B., 2005, in Shopbell P., Britton M., Ebert R., eds, Astronomical Society of the Pacific Conference Series Vol. 347, Astronomical Data Analysis Software and Systems XIV. p. 29

Taylor M., et al., 2021a, Do Massive Black Holes Come in Small Packages? A census of black holes in compact stellar systems in the Virgo cluster., JWST Proposal. Cycle 1, ID. #2567

Taylor M., et al., 2021b, High-resolution ACS/WFC Imaging of Compact Stellar Systems in the Virgo Cluster in Support of JWST Cycle 1 Science, HST Proposal. Cycle 29, ID. #16882

Thomas P. A., Drinkwater M. J., Evstigneeva E., 2008, MNRAS, 389, 102

Tonry J. L., et al., 2018, PASP, 130, 064505

Udalski A., Szymanski M., Kaluzny J., Kubiak M., Mateo M., 1992, Acta Astron., 42, 253

Udalski A., Szymański M. K., Szymański G., 2015, Acta Astron., 65, 1

Ulmer A., 1999, ApJ, 514, 180

Urrutia Zapata F., Fellhauer M., Alarcón Jara A. G., Matus Carrillo D. R., Aravena C. A., 2019, MNRAS, 489, 2746

Usher C., Forbes D. A., Spitler L. R., Brodie J. P., Romanowsky A. J., Strader J., Woodley K. A., 2013, MNRAS, 436, 1172

Vitral E., Mamon G. A., 2021, A&A, 646, A63

Voges W., et al., 1999, in Aschenbach B., Freyberg M. J., eds, Max-Planck-Institut für extraterrestrische Physik Vol. 272, Highlights in X-ray Astronomy. p. 282

Wang J., Merritt D., 2004, ApJ, 600, 149

Wang F., et al., 2021, ApJL, 907, L1

Wenger M., et al., 2000, A&AS, 143, 9

Wirth A., Gallagher J. S. I., 1984, ApJ, 282, 85

Wright E. L., et al., 2010, AJ, 140, 1868

Yang J., et al., 2020, ApJL, 897, L14

Yao Y., Sharma Y., Gezari S., Hammerstein E., Velzen S. V., Somalwar J., Kulkarni S., 2021, Transient Name Server Classification Report, 2021-1221, 1

York D. G., et al., 2000, AJ, 120, 1579

Zhang Y., Bell E. F., 2017, ApJL, 835, L2

van Haarlem M. P., et al., 2013, A&A, 556, A2

van Velzen S., et al., 2021, ApJ, 908, 4

Appendix A

CSS Light curve assessment

As detailed in the result of Chapter 3, of the 1484 CSS positions queried in the ZTF archive, only 29 had $\geqslant 8$ consecutive outliers across the two g and r filters used. An assessment of the light curves returned for those objects is included below. Information specified for objects includes distance modulus (DM, if included in light curve plot), maximum consecutive outliers (MC) and count of consecutive runs (RC) where more than 1 outlier occurs consecutively.

587726015089869000 (227.8638°, 1.7879°, MC=8, RC=7) - Max consecutive outliers related to reading across a two week period and thus likely associated with full moon phase.
587733398652649000 (256.0279°, 25.0551°, MC=8, RC=10) - Object is 7 pixels across and thus PSF unlikely to be providing and accurate estimate of magnitude. Some moon phasing evident in the early samples.
587733399713087000 (229.3217°, 46.7085°, MC=10, RC=72) - A bright object with an estimated diameter of 14 pixels. PSF suspect
587736915690258000 (246.3117°, 7.1457°, MC=8, RC=3) - A bright object with an estimated diameter of 10 pixels. PSF suspect
587729158982861000 (232.4121°, 3.3456°, MC=37, RC=13) - Very repetitive readings (same night?) on 4 occasions throughout 4 year period. Possibly cloud. Only one filter (r)
588016892785524000 (153.4338°, 38.7141°, MC=8, RC=35) - A bright object with an estimated diameter of 9 pixels. PSF suspect
588016892785524000 (153.46°, 38.7155°, MC=8, RC=24) - Duplicate
NGC4467 (Virgo group, 187.3758°, 7.9928°, MC=12, RC=80) - Wide dispersion in both filters. No signal apparent.
588017703489241000 (230.7846°, 8.6393°, MC=9, RC=13) - A bright object with an estimated diameter of 7 pixels. PSF suspect. Inconsistent peaks over 1-2 weeks 3 times in ztf-r filter
588295841247657000 (173.7042°, 49.0814°, MC=8, RC=24) - A bright object with an estimated diameter of 7 pixels. PSF suspect. Object close proximity to surface brightness of another object (host?)
588298663576928000 (195.7929°, 47.3811°, MC=8, RC=17) - A bright object with an estimated diameter of 13 pixels. PSF suspect. Object close proximity to surface brightness of another object (host?)
VCC1871 (Virgo group, 190.3154°, 11.3872°, MC=10, RC=83) - Object with brightest

r mag (15.4 mag). High samples but still noisy.

VCC1627 (Virgo group, 188.905°, 12.3819°, MC=12, RC=34) - Much brighter (16 mag) cluster than others. Need to check proximity to host galaxy.

AHcE6365 (DM=31.13, 186.6998°, 7.6715°, MC=11, RC=36) - A bright object with an estimated diameter of 20 pixels. PSF suspect.

NGC0821-UCD1 (DM=31.75 group, 32.0863°, 10.9907°, MC=8, RC=25) - Object within surface brightness of host galaxy. Peak seen in light curve shows multi-epoch variation over a single night.

J025629.35+155533.0 (DM=35.73 group, 44.1223°, 15.9258°, MC=15, RC=5) - One set of repetitive readings in r filter only -little correlation between filters.

587734622698406000 (116.5579°, 21.9933°, MC=11, RC=13) - 3-4 single night repetitive samples in r-filter, not corresponding in g-filter.

NGC2892-cE1 (DM=34.95 group, 143.2246°, 67.6151°, MC=9, RC=37) - Object within surface brightness of host galaxy. Peak seen in light curve shows multi-epoch variation over 2-3 nights.

NGC3115-UCD1 (DM=29.77 group, 151.3158°, −7.7143°, MC=8, RC=27) - Dim object barely visible in surface brightness of host galaxy spiral arms

587732157926670000 (119.7717°, 27.4595°, MC=14, RC=33) - Higher magnitude in both filters, suspect increased surface brightness from host galaxy.

NGC4278_acs_0795 (Coma I group, 185.0217°, 29.2778°, MC=14, RC=19) - Data only available in r filter and appears to be noise about the median throughout the entire year, and for every year of survey.

NGC4278_acs_1102 (Coma I group, 185.0329°, 29.2886°, MC=11, RC=46) - Good number of consecutive outliers, but light curve exceptionally noisy (g19.2/r18.4 mag)

NGC4494-UCD1 (DM=30.99 group, 187.8563°, 25.7722°, MC=10, RC=48) - Object within surface brightness of host. Consecutive outliers appear at moon peak.

NGC5846A (DM=32.13 group, 226.6217°, 1.595°, MC=9, RC=39) - A bright object with an estimated diameter of 17 pixels. PSF suspect. Peak over 12 days at start of season (calibration?)

NGC7727-cE (DM=31.84 group, 354.9737°, −12.2919°, MC=10, RC=38) - Object very close to nucleus of host (in projection)

NGVS-UCD420 (Virgo group, 187.7085°, 12.4025°, MC=8, RC=26) - Object within surface brightness of host galaxy. Consecutive points in first run of facility (05/2018)

VCC1199 (Virgo group, 187.3958°, 8.0581°, MC=11, RC=61) - A bright object with an estimated diameter of 14 pixels. PSF suspect.

587731870172315000 (185.4267°, 55.8091°, MC=8, RC=26) - No appreciable signal can be made out from the noise.

VCC1499 (Virgo group, 188.3325°, 12.8533°, MC=9, RC=62) - A bright object with an estimated diameter of 30 pixels. PSF suspect.